

# INAUGURAL - DISSERTATION

zur  
Erlangung der Doktorwürde  
der  
Naturwissenschaftlich-Mathematischen  
Gesamtfakultät  
der  
Ruprecht-Karls-Universität  
Heidelberg

Vorgelegt von  
Marcin Szymon Filipiak, MSc. Eng.  
aus Bydgoszcz (PL)

Tag der mündlichen Prüfung: 21.06.2019

---



Thema

# Carbon based nanomaterials for biosensing applications

1. **Gutachter:** Prof. Dr. Jana Zaumseil
2. **Gutachter:** Prof. Dr. Motomu Tanaka



Dissertation

Submitted to the  
Combined Faculty of Natural Sciences and  
Mathematics  
Heidelberg University, Germany  
for the degree of  
Doctor of Natural Sciences (Dr. rer. nat.)

Presented by  
Marcin Szymon Filipiak

Oral examination: June 21<sup>st</sup>, 2019

---



## Zusammenfassung

Es besteht ein hoher Bedarf an einer schnellen, zuverlässigen und hochempfindlichen Bestimmung verschiedener Biomarker in unbehandelten physiologischen Proben im Point-of-Care-Umfeld. Unter vielen Arten von Biosensoren scheinen elektrochemische und elektronische Wandler viele Anforderungen an zukünftige Diagnosegeräte zu erfüllen, wie etwa die marker-freie Bestimmung von Analyten in Echtzeit sowie die Möglichkeit der Massenfertigung. Neuere Entwicklung der Nanomaterialien, insbesondere der Kohlenstoff-basierten Nanomaterialien, löste auch ein Interesse an Biosensor-Anwendungen aus. In dieser Arbeit wurden zwei Kohlenstoff-Nanomaterialien - Graphen und Kohlenstoff-Nanoröhren - verwendet, um sowohl elektronische als auch elektrochemische Biosensoren zu konstruieren, die in physiologischen Proben funktionieren können und die für den Bereich Point-of-Care weiterentwickelt werden können. Die beiden Transduktionsarten wurden bewertet: 1) elektronisch (d. h. Feldeffekttransistor (FET)-basiert), basierend auf der Analytenbestimmung durch Ladung, und 2) elektrochemisch (d.h. amperometrisch), basierend auf der Analytbestimmung durch die auftretenden Redoxreaktionen an der Elektrode. Erstens wurden für den Aufbau eines Feld-Effekt-Transistor-Biosensors auf Basis eines Kohlenstoffnanoröhrchens neue und stabile Rezeptormoleküle - Nanokörper - eingesetzt und in einem markerfreien System mit grün fluoreszierendem Protein als Modellanalyt untersucht. Der Biosensor wies einen großen dynamischen Bereich mit niedriger Nachweisgrenze auf und war Ausgangspunkt für eine weitere anwendungsorientierte Studie. Zweitens wurde ein auf Graphen basierender Feldeffekttransistor (GFET) als Transducer für den Aufbau eines TSH-spezifischen Biosensors verwendet. Diese Lösung führte zu einer Abdeckung (und weit darüber hinaus) der TSH-Referenzwerte in physiologischen Proben. Schließlich wurde Graphen für den elektrochemischen Nachweis unter Verwendung des Setups aus der GFET-Studie als Arbeitselektrode verwendet. In Kombination mit dem Enzym Flavin-Adenin-Dinukleotid-abhängiger Glucosedehydrogenase (FAD-GDH) wurde ein elektrochemischer Glucosebiosensor hergestellt. Zusätzlich wurde ein direkter Elektronentransfer vom Enzym zur Graphenelektrode beobachtet. Die Ergebnisse dieser Arbeit tragen zur Entwicklung eines multimodalen Nachweises von Analyten in physiologischen Proben für die weitere Anwendung im Point-of-Care-Umfeld bei.

## Abstract

There is an unmet need of fast, reliable and highly sensitive determination of different biomarkers in untreated physiological samples in the Point-of-Care setting. Among many types of biosensors, electrochemical and electronic transducers seem to fulfill many requirements for future diagnostic devices such as label-free and real-time analyte determination, as well as a potential for mass-manufacturability. A recent advancement of nanomaterials, with particular focus on carbon nanomaterials, triggered a foundation of a new branch of biosensors to explore. In this work, two carbon nanomaterials - graphene and carbon nanotubes, were used to construct both electronic and electrochemical biosensors – able to work in physiological environment and with a potential for further development into the Point-of-Care environment. The two types of transduction were assessed - 1) electronic (*i.e.* field-effect transistor (FET) based), based on analyte determination by its charge, and 2) electrochemical (*i.e.* amperometric), based on analyte determination by the redox reactions that occur at the electrode. Firstly, for the construction of carbon nanotube network based field-effect transistor biosensor, novel and stable receptor molecules were employed - nanobodies, and studied in a label-free system with green fluorescent protein as a model analyte. The biosensor exhibited a wide dynamic range with low detection limit and triggered the next, more applicable study. Secondly, a graphene-based field-effect transistor (GFET) was employed as a transducer for construction of thyroid-stimulating hormone (TSH) specific biosensor. This solution resulted in coverage (and also going far beyond) of TSH reference values in physiological samples. Finally, for the electrochemical based detection, using the setup from GFET study, graphene was used as a working electrode and in combination with the enzyme - flavin adenine dinucleotide dependent glucose dehydrogenase (FAD-GDH), resulted in an electrochemical glucose biosensor. Direct electron transfer from the enzyme to the graphene electrode was additionally observed. The results of this work shed light and contribute to the development of multimodal detection of analytes in physiological samples for further application in Point-of-Care setting.

# Preface

Normally, to diagnose a patient, apart from the obvious visible symptoms, the physician takes a sample of the patient's blood. Then, the sample is transported into centralized laboratory, where a trained professional would analyze it to find out which biomarker concentration (or presence) is outside the reference values of a healthy individual. A biomarker is a naturally occurring indicator (gene, protein etc.) that can help assess the presence and progression of disease. Among biomarkers, proteins are especially useful due to their abundance in body fluids. As for selectively targeting the proteins even in complex samples, antibodies can be used. Another class of biomarkers are metabolites such as glucose or lactate that can be more or less specific to the disease. Once the illness is diagnosed (e.g. sepsis diagnosis by means of lactate determination), they can help monitor its progression and trigger immediate measures to overcome the disease symptoms (glucose monitoring and insulin dosing in diabetes). Analyzing the sample in a centralized analytical laboratory can take from several hours even up to a few days and in case of some very fast progressing diseases, it can be already too late for the patient's health and well-being. Therefore, near-patient testing, e.g. at the doctor's office (at *Point-of-Care*) and a result within the time of medical checkup, is needed. Unfortunately, so far the need for fast and reliable, on-the-spot diagnosis in the Point-of-Care setting is not completely realized. Huge diagnostics companies (e.g. Roche) are trying to make the dream of a simple, reliable and fast diagnostics device that can be used at the Point-of-Care, come true. Biosensors, devices comprising of a biomolecule sensitive layer - receptor, and a transducer that translates the biological signal generated at the receptor into measurable quantity, pose a very promising solution. A first biosensor appeared as early as 1962<sup>1</sup> and a completely new era of diagnostics began.

Among many types of biosensors, the main research focused on only three types - optical, electronic and electrochemical (see Section 1.1). Although optical methods have been used in biology/biochemistry for a long time (e.g. one of the first radioimmunoassays - 1960<sup>2</sup>), due to laborous sample preparation and complex instrumentation needed, they are not the first choice for Point-of-Care diagnostics. The greatest potential for development is attributed to electrochemical and electronic biosensors. A huge advancement of nanomaterial research in the last 30 years (<sup>3,4</sup>) accelerated the biosensors industry. Nanomaterials possess very high surface-to-volume ratio, not only do they enhance the surface area of the devices, but can also increase the sensitivity, time of response and be a building block for miniaturization of devices.

In this work two different carbon nanomaterials: graphene and carbon nanotubes are used in order to construct sensitive, reliable and fast biosensing devices that work in physiological buffer conditions accurately and specifically determining the concentration of given analyte. The goal of this thesis is to show the applicability and versatility of

novel carbon nanomaterials in different aspects of biosensing, due to high sensitivity and stability.

First, semiconducting single-walled carbon nanotube network based field-effect transistors were used as transducers for a green-fluorescent protein (GFP) specific nanobody-based biosensor (see Chapter 2). In the field of FET-based biosensors in complex matrices (serum, blood, plasma *etc.*), one encounters two large challenges: a) Debye screening, which is caused by the high concentration of ions that form a double layer on the liquid/solid interface and b) the non-specific adsorption of different species (proteins, cells, etc.). The idea pursued in this Chapter is based on co-immobilization of: 1) very short and stable receptors - nanobodies (VHH), that bring the specific analyte binding event closer to the biosensor's surface and provide high density of receptors and 2) poly(ethylene glycol) (PEG), that is shown to reduce the Debye screening limitation<sup>5-7</sup> and at the same time, prevents the non-specific adsorption.<sup>7-9</sup> The resulting biosensors show high selectivity, sub-picomolar detection limit and a dynamic range exceeding 5 orders of magnitude in physiological solutions.

In the later part of the work, graphene was shown to be effective both as a FET channel in electronic-based biosensing and as a working electrode in electrochemical-based biosensing. The construction and application of thyroid-stimulating hormone (TSH) specific graphene FET-based biosensor is presented in the Chapter 3. Here, the receptors (TSH specific F(ab')<sub>2</sub> antibody fragments) were co-immobilized with PEG to enable biosensing in high ionic strength buffer and reduce non-specific adsorption. The biosensor exhibited selective detection of TSH with concentrations as low as 10 fM, with a dynamic range spanning several orders of magnitude (i.e. fM – nM). By careful analysis of the changes in electronic properties upon analyte binding, the work presented in this chapter helps elucidating the mechanism of biosensing using a graphene field-effect transistor.

The third major part of the work describes the development of amperometric glucose biosensor with single-sheet graphene as a working electrode (Chapter 4). Interestingly, the glucose specific enzyme used (here, flavin adenine dinucleotide (FAD) dependent glucose dehydrogenase, FAD-GDH) exhibits direct electron transfer to the graphene electrode making it a 3rd generation amperometric glucose biosensor. To verify the activity of the enzyme, a "classical" redox mediator was used - ferrocenemethanol. Additionally, in order to reduce electrochemical interferences, a novel and unexplored redox mediator (nitrosoaniline derivative, NA) was employed.

*"You cannot hope to build a better world without improving the individuals. To that end, each of us must work for our own improvement and, at the same time, share a general responsibility for all humanity, our particular duty being to aid those to whom we think we can be most useful."*

*„Nie można bowiem mieć nadziei na skierowanie świata ku lepszym drogom, o ile się jednostek nie skieruje ku lepszemu. W tym celu każdy z nas powinien pracować nad udoskonaleniem się własnym, jednocześnie zdając sobie sprawę ze swej, osobistej odpowiedzialności za całokształt tego, co się dzieje w świecie, i z tego, że obowiązkiem bezpośrednim każdego z nas jest dopomagać tym, którym możemy się stać najbardziej użyteczni."*

— Maria Skłodowska-Curie



# Contents

<b>Abstract</b>	<b>2</b>
<b>Preface</b>	<b>2</b>
<b>1 Introduction</b>	<b>3</b>
1.1 Biosensors - receptors . . . . .	3
1.1.1 Immunosensors (immunochemical biosensors) . . . . .	4
1.1.2 Enzymatic biosensors . . . . .	6
1.1.3 Receptor immobilization . . . . .	8
1.2 Biosensors - transducers and analytical methods . . . . .	11
1.2.1 Electrochemical methods . . . . .	11
1.2.2 Field-effect transistor based biosensors . . . . .	16
1.2.3 Surface characterization methods . . . . .	26
1.3 Carbon based nanomaterials . . . . .	29
1.3.1 Graphene . . . . .	30
1.3.2 Carbon nanotubes . . . . .	33
1.3.3 Graphene and CNT comparison . . . . .	36
<b>2 Carbon nanotube field-effect transistors with nanobody receptors for immunodetection in physiological solutions</b>	<b>37</b>
2.1 Introduction . . . . .	37
2.2 Results . . . . .	39
2.2.1 Characterization of the electrolyte-gated CNT FET . . . . .	39
2.2.2 Surface functionalization of CNT FET . . . . .	40
2.2.3 Electrical characterization of VHH immobilization on CNT FET . . . . .	41
2.2.4 QCM reference measurements: GFP specific VHH immobilization and GFP binding . . . . .	43
2.2.5 Effect of PEGylation on GFP binding to the VHH modified CNT FET surface . . . . .	44
2.2.6 Control experiments with "off-receptor" and "off-target" . . . . .	45
2.2.7 Optimized SWCNT FET-based assay for GFP detection . . . . .	47
2.2.8 CNT FET long-term stability . . . . .	48
2.3 Discussion . . . . .	49
2.4 Conclusions . . . . .	52

<b>3</b>	<b>TSH immunosensing with single-sheet graphene field-effect transistor</b>	<b>53</b>
3.1	Introduction . . . . .	53
3.2	Results and discussion . . . . .	54
3.2.1	Device fabrication . . . . .	54
3.2.2	Surface functionalization of graphene . . . . .	55
3.2.3	TSH detection in high ionic strength buffer . . . . .	57
3.2.4	Detection mechanism . . . . .	61
3.3	Conclusions . . . . .	65
<b>4</b>	<b>Observation of direct electron transfer from glucose dehydrogenase to single-sheet graphene</b>	<b>67</b>
4.1	Introduction . . . . .	67
4.2	Results and discussion . . . . .	69
4.2.1	Direct electron transfer . . . . .	72
4.2.2	Mediated electron transfer using ferrocenemethanol as a redox mediator . . . . .	75
4.2.3	Mediated electron transfer using nitrosoaniline as a redox mediator . . . . .	77
4.2.4	Discussion . . . . .	79
4.3	Conclusions . . . . .	82
<b>5</b>	<b>Conclusions and outlook</b>	<b>83</b>
<b>6</b>	<b>Materials and methods</b>	<b>85</b>
6.1	Single-walled carbon nanotube network field-effect transistor for immunodetection in physiological conditions . . . . .	85
6.1.1	Preparation of SWCNT dispersions. . . . .	85
6.1.2	FET fabrication . . . . .	85
6.1.3	Liquid handling . . . . .	86
6.1.4	Expression of receptor and analyte molecules . . . . .	86
6.1.5	Surface functionalization . . . . .	86
6.1.6	Measurement setup . . . . .	87
6.1.7	QCM study . . . . .	87
6.2	TSH immunosensing with GFET . . . . .	87
6.2.1	Materials . . . . .	87
6.2.2	Fabrication of substrate and gold contacts . . . . .	88
6.2.3	Graphene transfer and flow chamber assembly . . . . .	88
6.2.4	Surface functionalization and TSH detection . . . . .	88
6.2.5	Measurement setup . . . . .	89
6.3	DET from GDH to graphene . . . . .	89
6.3.1	Single-sheet graphene electrodes . . . . .	89
6.3.2	Liquid handling . . . . .	89
6.3.3	Surface functionalization . . . . .	89
6.3.4	Measurement setup . . . . .	90
	<b>Personal information</b>	<b>113</b>
	<b>Acknowledgements</b>	<b>117</b>

# 1 | Introduction

## 1.1 Biosensors - receptors

A **biosensor** is an analytical device comprising a **bioreceptor** (biological recognizing element) from different classes (enzymes, antibodies and its fragments, whole cells, DNA, RNA etc.) and a **transducer** (physicochemical signal detection element), which can be divided into several subgroups: 1) electrochemical (including amperometric and potentiometric), 2) electrical (field-effect transistor based and conductometric), 3) optical, 4) calorimetric and 5) piezoelectric (quartz crystal microbalance, cantilever)<sup>10</sup> (see Fig. 1.1). Biosensors offer a lot of advantages over conventional analytical techniques, including portability, miniaturization and on-site monitoring as well as good selectivity and sensitivity depending on the transducer.

In this work, carbon nanomaterial based electrochemical (in particular graphene based, Chapter 4) and electrical (carbon nanotube based - Chapter 2 and graphene based - Chapter 3) biosensors were explored. In this section, the fundamentals of biosensing methods will be described.

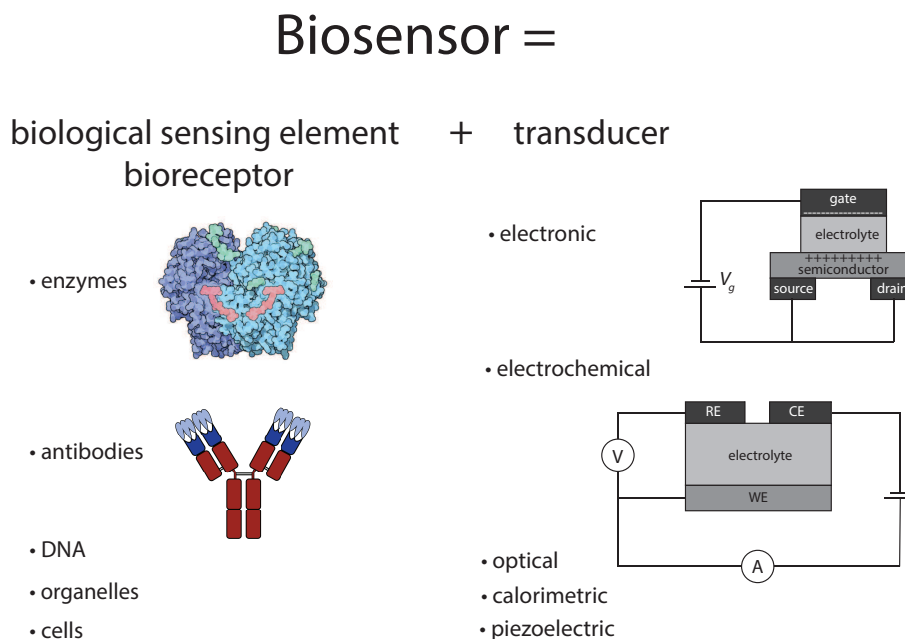


**Figure 1.1** – Scheme of a biosensor. Biological sensing elements are coupled to transducers. These transduce the signal to deliver a readable output.

### 1.1.1 Immunosensors (immunochemical biosensors)

Immunosensing, as the name suggests, is the field of biosensing focusing on sensing the analytes *via* the immunochemical reactions. An antibody (or one of its many fragments, see Fig. 1.3) is immobilized on the surface of the transducer and the analyte binding signal is recorded as a function of the analyte concentration (see Fig. 1.2). This strategy is called "label-free" or "direct assay" and is the least complex when it comes to the mechanism, yet most difficult to utilize, because of rather small signals generated and high abundance of non-specific signal. Often, a control biosensor is additionally used, which generates the signal from binding of the non-target species (interferences) and after the subtraction of "active" and "control" biosensor signals, target binding specific signal can be assessed. In order to enhance the signal and increase the specificity of the assay, researchers use "labels" - a species, most commonly a secondary antibody, that binds to the already bound analyte. "Labels" can include a bioconjugated (attached to the secondary antibody) element like an enzyme (e.g. horseradish peroxidase), that catalyses a redox reaction, the product of which can be sensed e.g. electrochemically.<sup>11</sup>

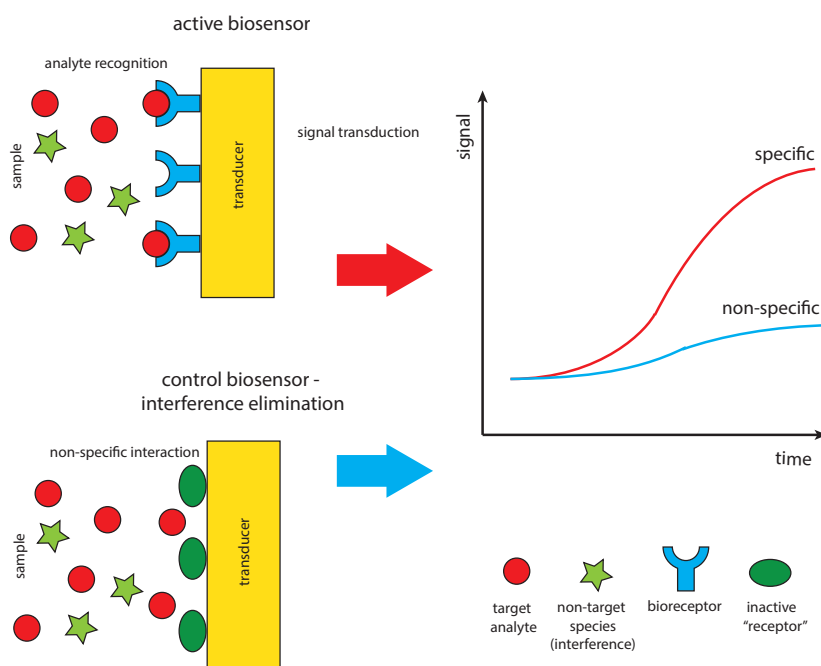


**Figure 1.2** – Schematic representation of the main components and mode of action of a immunosensor. In this case, a typical label-free immunoassay-based biosensor is depicted as an example of a biosensor setup. A device capable of immobilizing the molecule of interest for detection will allow the conversion of an input signal to a quantifiable output signal for transduction and generation of a final measurement.

Antibodies (immunoglobulins - IgG) are a large family of Y-shaped glycoproteins, which are used by the immune system as recognition elements for different targets (*antigens*) in order to neutralize *pathogens* (bacteria, viruses, etc.). Each tip of the "Y" of an antibody contains a *paratope* ("lock") that is specific for one particular *epitope* ("key") on an antigen, allowing these two structures to bind. Their structures are divided into two regions - the variable (V) region (top of the Y) defining antigen binding properties and

the constant (C) region (stem of the Y), interacting with effector cells and molecules.<sup>12</sup> IgGs contain two identical heavy (H, 50 kDa, Fig. 1.3, blue) and two identical light (L, 25 kDa, Fig. 1.3, green) chains (resulting in a molecular weight  $M_w \approx 150$  kDa). Several disulfide bonds link the two heavy chains (black lines between blue chains in IgG, Fig. 1.3), the heavy and light chains, and reside inside the chains. The variable (V) regions of both chains cover approximately the first 110 amino acids, forming two antigen-binding (Fab) regions (55 kDa each), whereas the remaining sequences are constant (C) regions, forming Fc (fragment crystallizable) regions for effector recognition and binding. Two Fab fragments linked with a disulfide bridge form a  $F(ab')_2$  fragment used in the work described in Chapter 3. The sequences of both the heavy and light chains vary greatly between different antibodies. Approximately 95% are constant and the remaining 5% are variable and create their antigen-binding specificity.<sup>12</sup> A special type of immune system entity - nanobodies - a variable region of a heavy chain of a camelid antibody exist in camelids (*e.g.* alpacas) and has a very small size of around 15 kDa. Those were used and are further described in Chapter 2.

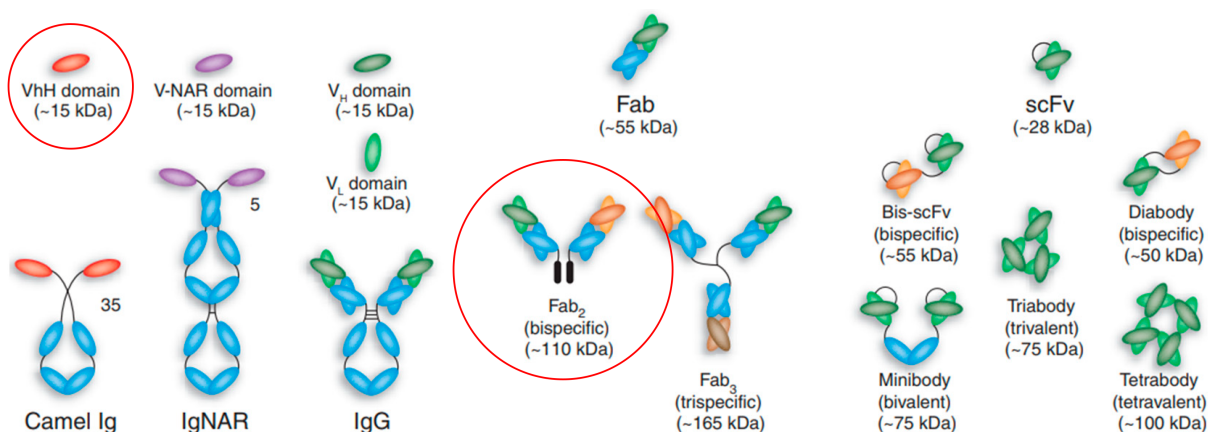


**Figure 1.3** – Schematic representation of different antibody formats, showing intact "classic" IgG molecules alongside camelid VhH-Ig and shark Ig-NAR immunoglobulins. Camelid VhH-Ig and shark Ig-NARs are unusual immunoglobulin-like structures comprising a homodimeric pair of two chains of V-like and C-like domains (neither has a light chain), in which the displayed V domains bind target independently. Shark Ig NARs comprise a homodimer of one variable domain (V-NAR) and five C-like constant domains (C-NAR). A variety of antibody fragments are depicted, including Fab, scFv, single-domain VH, VhH and V-NAR and multimeric formats, such as minibodies, bis-scFv, diabodies, triabodies, tetrabodies and chemically conjugated Fab' multimers (sizes given in kilodaltons are approximate). Circled receptors were used in this work - VHH in Chapter 2 and  $F(ab')_2$  in Chapter 3. Reprinted and readapted with permission from.<sup>13</sup> Copyright 2005 Nature Publishing Group.

Historically, antibodies were first used as receptors in immunosensors, but due to their size and (in)stability, researchers began to look for alternatives. With advances in protein engineering and biochemistry, new classes of receptors emerged: from different antibody fragments (Fig. 1.3), through aptamers (RNA or DNA based receptors) to molecularly imprinted polymers (polymers with a molecular imprint of the target analyte).

Among such short receptors are single-domain antibodies (so-called nanobodies). With a molecular weight of only  $\sim 13$  kDa and size of  $\sim 2-3$  nm, nanobodies are much smaller

than the common whole antibodies ( $\sim 150$  kDa,  $\sim 15$  nm) or Fab fragments ( $\sim 50$  kDa, 7- 8 nm).<sup>14,15</sup> In addition, the nanobodies are easily produced, highly soluble and stable in a range of different conditions.<sup>16</sup> So far, their usefulness as recognition elements of a biosensor has been proven in photoelectrochemical<sup>17,18</sup> and electrochemical<sup>19,20</sup> formats, but not in combination with transistor-based sensors.

All immunochemical reactions are governed by a receptor specific constant - the dissociation constant ( $K_d$ ),<sup>21</sup> which measures the tendency of a receptor-antigen complex to separate (dissociate) reversibly into free receptor and free antigen.

Binding of the antigen (A) to the receptor (R):



is described by the law of mass action, applying the association constant  $K_a$ :

$$K_a = \frac{k_{on}}{k_{off}} = \frac{[A - R]}{[A] \times [R]} \quad (1.2)$$

or its reciprocal value, the dissociation constant (more commonly used)  $K_d$ :

$$K_d = \frac{1}{K_a} = \frac{k_{off}}{k_{on}} = \frac{[A] \times [R]}{[A - R]} \quad (1.3)$$

Association constants possess the dimension of reciprocal concentration ( $M^{-1}$ ) and higher values indicate stronger binding, while dissociation constants possess the dimension of a concentration (M) and lower values indicate stronger binding.

### 1.1.2 Enzymatic biosensors

The first (enzymatic) biosensor ever was developed by Clark<sup>1</sup> in as early as 1962. The idea was quite simple: a cell containing a platinum and silver electrode was used. Platinum acts as a oxygen reduction electrocatalyst, while the silver electrode is a pseudo-reference electrode. Upon applied potential between the two electrodes, the oxygen from the solution is electroreduced at the Pt electrode. This setup, after implementing an additional layer of glucose oxidase, which catalyses the oxidation of glucose while locally using up oxygen, was used as a first ever biosensor. The rate of reaction current is limited by the diffusion of both glucose and oxygen.

Given the above, an enzymatic biosensor is a device that uses the enzyme to provide selectivity of the method (e.g. amperometry like in the example above<sup>1</sup>) by catalyzing a specific biochemical reaction. The selectivity of the enzymatic biosensor towards the analyte is given by the selectivity of the enzyme itself. The analyte in the context of catalysed reaction can play different roles - substrate (e.g. glucose biosensors<sup>22</sup>), inhibitor (organopesticide biosensor based on inhibition of acetylcholinesterase e.g.<sup>23</sup>) or even the enzyme itself (lactate dehydrogenase activity biosensor e.g.<sup>24</sup>)

**Enzyme basics** Enzymes are the biological systems catalysts - proteins that are able change the pathway and thus lower the activation energy of a reaction. The specificity of an enzyme is due to the precise interaction of the substrate with the enzyme. This

precision is a result of the intricate three-dimensional structure of the enzyme protein. Catalysis takes place at a particular site on the enzyme called the *active site*. The catalytic activity of many enzymes depends on the presence of small molecules termed *cofactors*, which can be covalently bound to the enzyme (e.g. FAD in glucose dehydrogenase<sup>25</sup>) or free-diffusing in the solution (as in the case of NAD<sup>+</sup>-dependent lactate dehydrogenase<sup>26</sup>). Such an enzyme without its cofactor is referred to as an *apoenzyme*, whereas the complete, catalytically active enzyme is called a *holoenzyme*.<sup>27</sup> There are many classes of enzymes, but the ones that are mostly used in biosensors, belong to the class of oxido-reductases (Enzyme Commission number - EC 1<sup>28</sup>), which as the name suggests catalyse oxidation-reduction reactions.

The catalytic activity of an enzyme is the property measured by the increase in the rate of reaction of a specified chemical reaction that the enzyme produces in a specific assay system. *Enzyme activity* is defined as moles of substrate converted per unit time. The SI unit for enzyme activity is katal, although more commonly used one is an enzyme unit (U), which is 1  $\mu\text{mol}/\text{min}$  (1 U = 16.67 nkat).<sup>29</sup> Another commonly used measure to describe enzyme activity is *specific enzyme activity*. It gives information about the enzyme sample purity and is expressed as activity of an enzyme per milligram of total protein (unit:  $\frac{\mu\text{mol}}{\text{min} \times \text{mg}}$  or simply U/mg).

The primary function of enzymes is to enhance rates of reactions, so that they are compatible with the needs of the organism. The most commonly used kinetic model was developed by Michaelis and Menten<sup>30</sup> (see 1.4). At a fixed concentration of enzyme, reaction rate ( $V_0$ ) is almost linearly proportional to substrate concentration [S] when [S] is small, but is nearly independent of [S], when [S] is large. The critical feature in the Michaelis-Menten model is that a specific E-S complex is a necessary intermediate in catalysis. Considering an enzyme (E) that catalyses the reaction of substrate (S) to product (P) conversion:



where  $k_{-1}$  is the forward rate constant,  $k_{-1}$  is the reverse rate constant and  $k_2$  is the catalytic rate constant.

Assuming that the enzyme concentration [E] is much smaller than the substrate concentration [S], the rate of product formation  $V_0$  is given by equation:

$$V_0 = \frac{d[P]}{dt} = V_{max} \frac{[S]}{K_M + [S]} = k_{cat}[E]_0 \frac{[S]}{K_M + [S]} \quad (1.5)$$

where  $K_M$  is the *Michaelis-Menten constant*,  $k_{cat}$  is the *turnover number* - maximum number of substrate molecules converted to product per enzyme molecule per second,  $E_0$  is the initial enzyme concentration.

The reaction order depends on the relative size of the two terms in the denominator. At low substrate concentration  $[S] \ll K_M$  the equation 1.5 simplifies to:

$$V_0 = k_{cat}[E]_0 \frac{[S]}{K_M} \quad (1.6)$$

Under these conditions the reaction rate increases linearly with substrate concentration [S] (*first order kinetics*).

With higher substrate concentration -  $[S] \gg K_M$ , the reaction rate becomes substrate concentration independent (*zero order kinetics*) and asymptotically approaches the maximum reaction rate (saturates) -  $V_{max} = k_{cat}[E]_0$ .

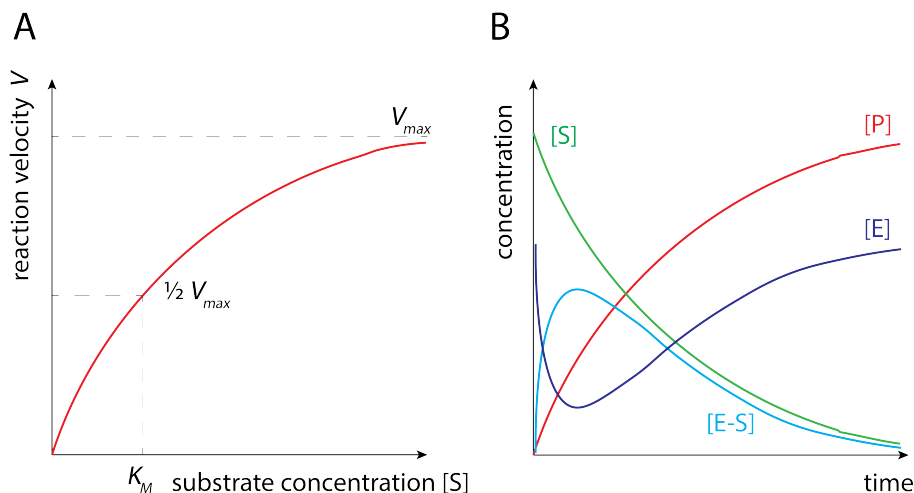


**Figure 1.4** – *Michael-Menten kinetics* **A** A plot of the reaction velocity ( $V_0$ ) as a function of the substrate concentration  $[S]$  for an enzyme that obeys Michaelis-Menten kinetics shows that the maximal velocity ( $V_{max}$ ) is approached asymptotically. The Michaelis constant ( $K_M$ ) is the substrate concentration yielding a velocity of  $V_{max}/2$ . **B** Concentration profiles of substrate  $[S]$ , product  $[P]$ , free enzyme  $[E]$  and enzyme-substrate complex  $[E-S]$  according to Michaelis-Menten kinetics.

Practically, Michaelis-Menten constant is the concentration at which the reaction rate is half of the maximum. Furthermore, the Michaelis-Menten constant is often used as measure of substrate's affinity of the enzyme - the smaller the  $K_M$ , the higher the substrate's affinity towards the enzyme.  $K_M$  has a direct influence on the analytical parameters of different enzymatic biosensors - the reaction rate can be easily substituted by biosensor's signal (be it electrochemical, optical etc.). For example, for glucose dehydrogenase,<sup>31</sup> the  $K_M$  is 68 mM, which makes a biosensor's steady-state response linear in the relevant reference range in blood (1 - 20 mM), but for lactate oxidase, the  $K_M$  is about 1 mM<sup>32</sup> and with the reference range 0.2 - 25 mM (extreme case - sportsmen),<sup>33</sup> the measurement needs to be finely timed to resolve the higher lactate concentrations.  $K_M$  depends on substrate and enzyme pair, as well as on pH and temperature.<sup>34</sup>

### 1.1.3 Receptor immobilization

In order to construct a biosensor, the receptor needs to be immobilized on the sensing surface (transducer). There are several strategies for receptor immobilization 1) adsorption, 2) covalent bonding, 3) entrapment in a matrix, 4) cross-linking (with e.g. glutaraldehyde) and 5) affinity based binding.<sup>35</sup> Each immobilization method presents advantages and drawbacks. The choice of the most appropriate technique depends on the receptor nature, the transducer and the associated detection mode. A perfect immobilization strategy aims at preserving the activity of the receptor, stability, maximizing the biosensor's response (sensitivity) and reproducibility.

**Pyrene chemistry** Covalent bonding of receptor to a linker molecule (pyrene derivatives) is used to fabricate a specific target carbon nanomaterial based biosensor. Generally, the bare CNT or bare graphene are first exposed to the linker molecules (pyrene derivatives) to introduce the anchoring sites (carboxyl groups -COOH, *N*-hydroxysuccinimide (NHS) ester of carboxyl groups or maleimide groups (MAL)) for the later receptor and spacer immobilization. Pyrene (C<sub>16</sub>H<sub>10</sub>) is a polycyclic aromatic hydrocarbon consisting of four fused benzene rings, resulting in a flat aromatic system. The pyrenes form a monolayer on the surface of both graphene and carbon nanotubes by means of  $\pi$ - $\pi$  stacking.<sup>36,37</sup> Three types of pyrene (Fig. 1.5 A) derivatives were used in this work: 1-pyrenebutyric acid (PBA, Fig. 1.5 B), 1-pyrenebutyric acid *N*-hydroxysuccinimide ester (PBA-NHS, Fig. 1.5 C) and *N*-(1-pyrenyl)maleimide (py-MAL, Fig. 1.5 D).

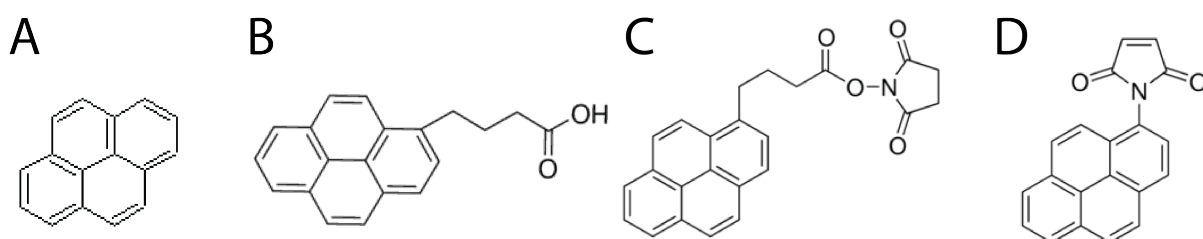


**Figure 1.5** – Chemical formulas of pyrene and its derivatives used in this work. **A** Pyrene, **B** 1-pyrenebutyric acid, **C** 1-pyrenebutyric acid *N*-hydroxysuccinimide ester and **D** *N*-(1-pyrenyl)maleimide

**EDC/NHS chemistry** One of the most standard, specific and widely used bioconjugation methods is based on carbodiimides.<sup>38,39</sup> Carbodiimide conjugation works by activating carboxyl groups (-COOH) for direct reaction with primary amines (-NH<sub>2</sub>) *via* amide bond formation. Because no portion of their chemical structure becomes part of the final bond between conjugated molecules, carbodiimides are considered zero-length carboxyl-to-amine crosslinkers.<sup>40</sup> The most widely used carbodiimide is water soluble (but also easily hydrolyzed!) 1-ethyl-3-(3-dimethylaminopropyl) carbodiimide hydrochloride (EDC). It reacts with carboxylic acid groups to form an active *O*-acylisourea intermediate that is easily displaced by nucleophilic attack from primary amino groups in the reaction mixture (e.g. -NH<sub>2</sub> residues of surface lysines present in the antibody or an enzyme). The primary amine forms an amide bond with the original carboxyl group, and an EDC by-product is released as a soluble urea derivative. *N*-hydroxysuccinimide (NHS) is often included in EDC coupling protocols to improve efficiency or create stable in dry conditions (amine-reactive) intermediates. EDC couples NHS to carboxyls, forming an NHS ester that is considerably more stable than the *O*-acylisourea intermediate while allowing for efficient conjugation to primary amines at physiologic pH. For a simplified mechanism of EDC/NHS conjugation see Fig. 1.6 A. NHS activated linkers are also available to simply introduce the protein of interest to the desired surface.

**Maleimide chemistry** The often occurring -SH surface groups (cysteine residues) can be conjugated to *via* the sulfhydryl-reactive crosslinker reactive groups like maleimide. There are many advantages of using this conjugation (immobilization) strategy:

1. Thiols are present in most proteins but are not as numerous as primary amines, thus crosslinking *via* thiol groups is more precise and selective.
2. Thiol groups in proteins are often involved in disulfide bonds, so cross-linking at these sites typically does not significantly modify the underlying protein structure or block binding sites.
3. The number of available thiol groups can be easily controlled or modified (reduction of disulfide bonds or introduction of thiol groups into molecules).

The maleimide group reacts specifically with sulfhydryl groups resulting in formation of a stable, irreversible thioether linkage. For a simplified mechanism of maleimide/thiol conjugation see Fig. 1.6 B.

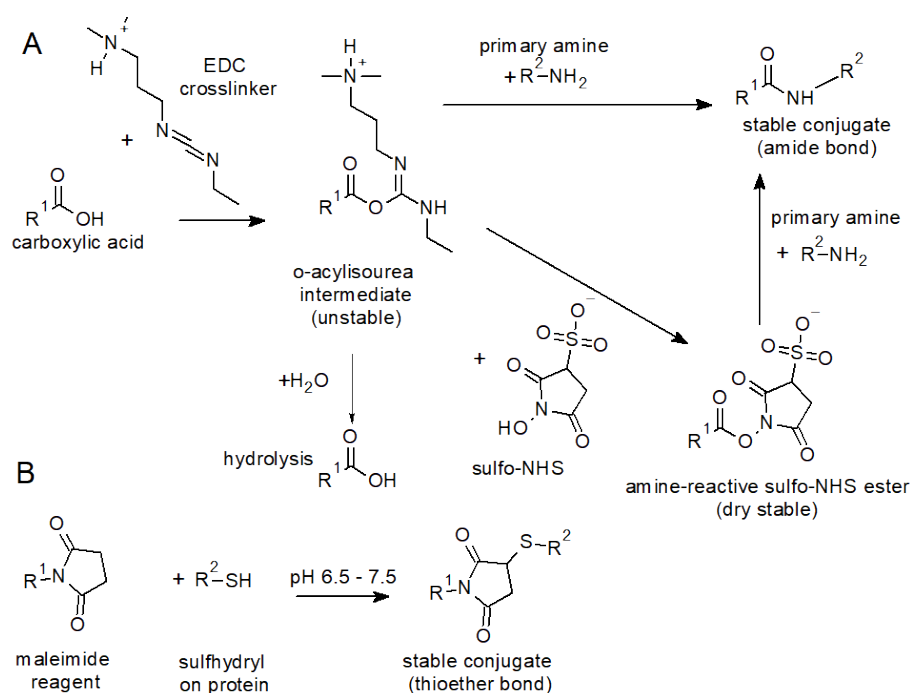


**Figure 1.6** – *A* Carboxyl-to-amine crosslinking using the carbodiimide EDC and NHS. *B* Maleimide reaction scheme for chemical conjugation to a thiol.

## 1.2 Biosensors - transducers and analytical methods

### 1.2.1 Electrochemical methods

Electrochemistry studies reactions with electron transfer at the electrolyte|electrode interface. The electron transfer is caused by oxidation-reduction reactions. Figure 1.7 compares: **A** *homogeneous* (one phase - liquid) electron transfer (reduction reaction) from cobalt cyclopentadienyl ( $\text{Co}(\text{Cp}\cdot)_2$ ) to ferrocenium ion ( $\text{Fc}^+$ )  $\text{Fc}^+ + [\text{Co}(\text{Cp}\cdot)_2] \rightleftharpoons \text{Fc} + [\text{Co}(\text{Cp}\cdot)_2]^+$  ( $\text{Fc}^+$  reduction coupled with  $\text{Co}(\text{Cp}\cdot)_2$  oxidation) with **B** *heterogeneous* (on the liquid|solid interface) electron transfer from the electrode to  $\text{Fc}^+$  (ferrocenium ion *electroreduction*). In the beginning of the process shown in the Fig. 1.7 B, the electron potential is not sufficient to be transferred from the electrode, but when the electron potential is increased to a certain level higher than the lowest unoccupied molecular orbital (LUMO) energy level of the  $\text{Fc}^+$ , the electron can be transferred from the electrode to  $\text{Fc}^+$  thus reducing the  $\text{Fc}^+$  ion to  $\text{Fc}$ .

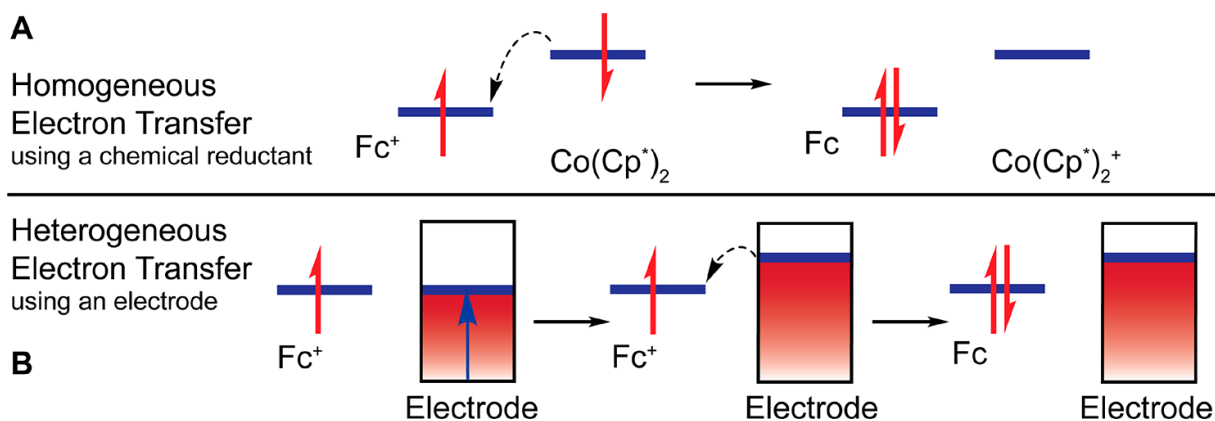


**Figure 1.7** – (A) Homogeneous and (B) heterogeneous reduction of  $\text{Fc}^+$  to  $\text{Fc}$ . The potential of the electrons in the electrode is controlled by the potentiostat; their potential can be increased until electron transfer becomes favorable. Reprinted with permission from.<sup>41</sup> Copyright 2018 American Chemical Society.

A typical electrochemical cell consists of 3 different electrodes: 1) a stationary *working electrode* (WE), 2) a *reference electrode* (RE) which the potential is applied against, and 3) a *counter (auxiliary) electrode* that completes an electrical circuit with WE over which the current flows. All three are immersed in a stagnant solution containing the electroactive species as well as an excess of supporting electrolyte (an inert salt, e.g. KCl) to provide sufficient ionic conductivity and migration. The electrochemical reaction under study takes place at the surface of the working electrode. The electrochemical signal recorded reflects the process taking place at the working electrode such that our interest is focused on the interface of this electrode with the electrolytic solution.

**Mass transport** When the sufficient potential is applied, the electroactive species in the solution, undergo redox reaction at the electrode changing the local concentration of the respective species in the vicinity of the electrode. This potential is generally governed

by the Nernst equation, which predicts the relationship between concentration and voltage (potential difference).

$$E = E^0 + \frac{RT}{nF} \ln \frac{Fc^+}{Fc} \quad (1.7)$$

In a typical electrochemical experiment, a large amount of electroactive molecules are involved and thus the diffusion process obey the Fick's laws accounting for changes in concentration with time and distance from the working electrode.<sup>42</sup> For the simplest case of planar electrode exhibiting linear diffusion, all the points at a given distance from the electrode surface in the perpendicular coordinate  $x$  are equivalent such that net flux of molecules only occurs in this direction. According to Fick's first law, the flux,  $j$  (unit:  $\frac{mol}{m^2 \times s}$ ), at a given point  $x_1$ , is proportional to the concentration gradient:

$$j_{j,x_1} = -D_j \left( \frac{\partial c_j}{\partial x} \right)_{x_1} \quad (1.8)$$

where  $D_j$  is the diffusion coefficient of species  $j$ . The solutions of the Equation 1.8 (i.e. the concentration profiles of the participating species) are functions of only two independent variables: time  $t$  and the distance to the electrode surface in the  $x$  coordinate.<sup>42</sup>

As mentioned, during the time of the measurement, the concentration gradient can change and this is described by the Fick's second law of diffusion:

$$\frac{\partial c_j}{\partial t} = -D_j \left( \frac{\partial^2 c_j}{\partial x^2} \right) \quad (1.9)$$

Fick's second law predicts the variation of concentration of different species as a function of time within the electrochemical cell. In order to solve these equations analytical or computational models are usually used. Concentration profiles are the graphical representations of the Fick's second law solutions (equations) and they indicate the gradual expansion of the *diffusion layer* towards the bulk of the solution as shown in the Fig. 1.8 A-G.

## Cyclic voltammetry

Cyclic voltammetry is the basic and the most informative electroanalytical technique provides information about i.e. the potentials of redox processes, the oxidation state of the redox species, the number of electrons involved, the rate of electron transfer, possible chemical processes associated with the electron transfer, adsorption effects, standard redox potential ( $E_0 = \frac{E_{p,c} + E_{p,a}}{2}$ ) or transfer electron number ( $\Delta E = E_{p,a} - E_{p,c} = 58/n$ ), where  $E_0$  is the standard redox potential,  $E_{p,a}$  is the anodic (oxidation) peak potential,  $E_{p,c}$  is cathodic (reduction) peak potential and  $n$  - number of electrons.

Considering a simple solution containing 1 mM ferrocene (Fc), the concentration of its oxidized form at the beginning of the experiment is 0 (Fig. 1.8 A). When a potential between WE and RE is linearly increased from  $E_1$  to  $E_1$ , the electrooxidation reaction of Fc starts to occur, which is seen as the increase of the current (Fig. 1.8 H) and consequently, the concentration of Fc in the vicinity of the electrode drops (Fig. 1.8 B). Here, the electron transfer rate is fast in comparison to the voltage sweep rate and thus at the electrode surface an equilibrium is established identical to that predicted by

thermodynamics (Nernst equation). The rate of the reaction reaches its maximum (Fig. 1.8 C) exhibiting a characteristic current peak ( $I_{p,a}$  - anodic (oxidation) peak) at the potential  $E = E_{p,a}$ . The peak occurs, since the diffusion layer has grown sufficiently above the electrode that the flux of the electroactive species to the electrode is not fast enough to satisfy the requirements of the Nernst equation. In this situation the current begins to drop. At this point, the concentration of Fc near the electrode is approaching 0 and finally reaches 0 with further potential increase (Fig. 1.8 D). The the diffusion layer continues to grow throughout the scan (see Section 1.2.1). This slows down mass transport of Fc to the electrode. Typically then, the potential scan direction is reversed and the  $\text{Fc}^+$  reduction reaction is starting to appear in the current response (Fig. 1.8 E). The maximum for cathodic (reduction) current is then achieved ( $I_{p,c}$  at the potential  $E = E_{p,c}$ ) with the maximum reaction rate in the F point (Fig. 1.8 F). After that with further scanning, the reduction current decreases to reach the G point, similarly extending the diffusion layer as with the "forward" scan (Fig. 1.8 G).

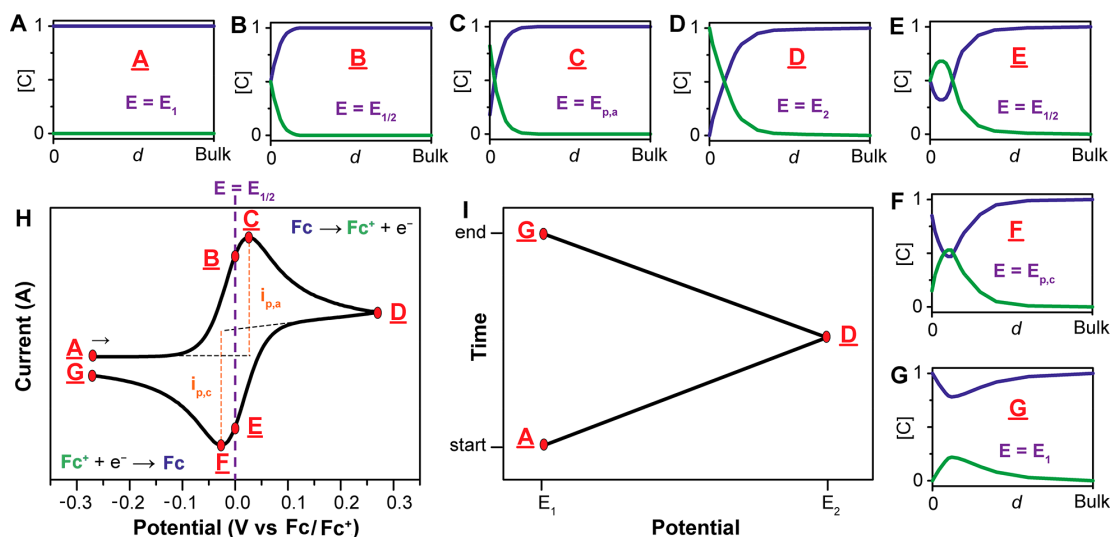


**Figure 1.8** – **A-G** Concentration profiles (mM) for Fc (blue) and  $\text{Fc}^+$  (green) as a function of the distance from the electrode ( $d$ , from the electrode surface to the bulk solution, e.g. 0.5 mm) at various points during the voltammogram. **H** Voltammogram of the reversible reduction of a 1 mM Fc solution to  $\text{Fc}^+$ , at a scan rate of 100 mV/s. **I** Applied potential as a function of time for a generic cyclic voltammetry experiment, with the initial, switching, and end potentials represented (**A**, **D**, and **G**, respectively). Reprinted and adapted to comply with IUPAC convention with permission from.<sup>41</sup> Copyright 2018 American Chemical Society.

In equilibrium between the  $\text{Fc}/\text{Fc}^+$ , the potential in an electrochemical cell is described by the Nernst equation:

$$E = E^0 + \frac{RT}{nF} \ln \frac{(Ox)}{(Red)} = E^0 + 2.3026 \frac{RT}{nF} \log_{10} \frac{(Ox)}{(Red)} \quad (1.10)$$

where  $E^0$  is the standard potential,  $F$  is Faraday's constant,  $R$  is the universal gas constant,  $n$  is the number of electrons,  $T$  is the temperature and  $(Ox)$  and  $(Red)$  are the activities of oxidized and reduced form of a species, respectively.

The magnitude of the peak current for a reversible electron transfer is given by the Randles-Ševčík equation 1.11:<sup>43</sup>

$$I_p = 0.446nFAC\sqrt{\frac{nFvD}{RT}} \quad (1.11)$$

where  $I$  - peak current,  $n$  - number of electrons transferred per molecule diffusing to the electrode surface,  $F$  - Faraday constant,  $A$  - electroactive surface area,  $C$  - concentration of the analyte in solution,  $v$  - scan rate,  $D$  - diffusion coefficient of the analyte,  $R$  - gas constant and  $T$  - absolute temperature.

The Randles-Ševčík equation describes the effect of scan rate on the peak current - with an increase of the scan rate, the peak current also increases.<sup>44</sup> The equation is used variously e.g. to estimate the diffusion coefficient  $D$  of redox species.<sup>44</sup> Additionally, for a known diffusion coefficient and concentration of electroactive species, the electroactive surface area of the working electrode under study using this equation (applied in Section 4.2.2) and used for comparisons with the literature. Moreover, plotting of  $I_p$  vs.  $v^{1/2}$  provides information about stoichiometry of the redox process e.g. for a chemically reversible redox process, the function  $I_p$  in terms of  $v^{1/2}$  is linear.

### Chronoamperometry

Another commonly used electrochemical technique for analysis is chronoamperometry, where a step of potential is applied and kept constant while the current response is measured in undisturbed conditions ( $I = f(t)$ ), i.e. the mass transport is diffusion limited. The potential is stepped from  $E_1$ , where no current flows, i.e. the oxidation or reduction of the electrochemically active species does not take place, to  $E_2$  where the current belongs to the electrode reaction is limited by diffusion (see Fig. 1.9).

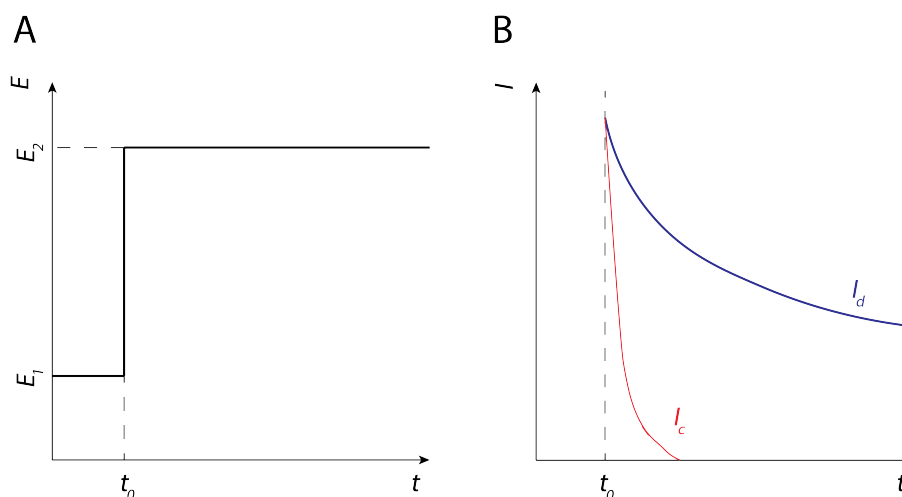


**Figure 1.9** – Typical waveform of the potential step (A) and the respective chronoamperometric response (B). ( $I_c$  - capacitive current,  $I_d$  - diffusion current).

The Faradaic current response decays as described in the Cottrell equation:<sup>45</sup>

$$I = nFAC \frac{D}{\pi t} \quad (1.12)$$

where  $I$  - current,  $n$  - number of electrons transferred per molecule diffusing to the electrode surface.

The equation shows that the current decays (as shown in Fig. 1.9 B), from an initial infinite value, proportionally as  $1/\sqrt{t}$  and, furthermore, that no steady state current is ever achieved. The capacitive current,  $I_c$ , coming from the electrical double layer formation, is also present in the beginning of the experiment, but decays exponentially (as shown in Fig. 1.9 B). Plotting  $I(t)$  vs.  $t^{-1/2}$  and reading out the slope can give information about diffusion coefficient. Finally, the Cottrell equation can be applied only when considering planar working electrodes of "infinite" size (the edge effect is negligible).<sup>43</sup>

## 1.2.2 Field-effect transistor based biosensors

Field-effect transistor-based transducers are considered charge-sensitive devices and exhibit a range of advantages such as excellent sensitivity and selectivity, label-free detection, real-time response, cost-effective fabrication, and ease of miniaturization and integration in electronic chips. This makes FET-based biosensors applicable in Point-of-Care setting.<sup>46</sup>

The operating mechanism of a field-effect transistor is shown using the example of the metal oxide semiconductor FET (MOSFET) (see Fig. 1.10).

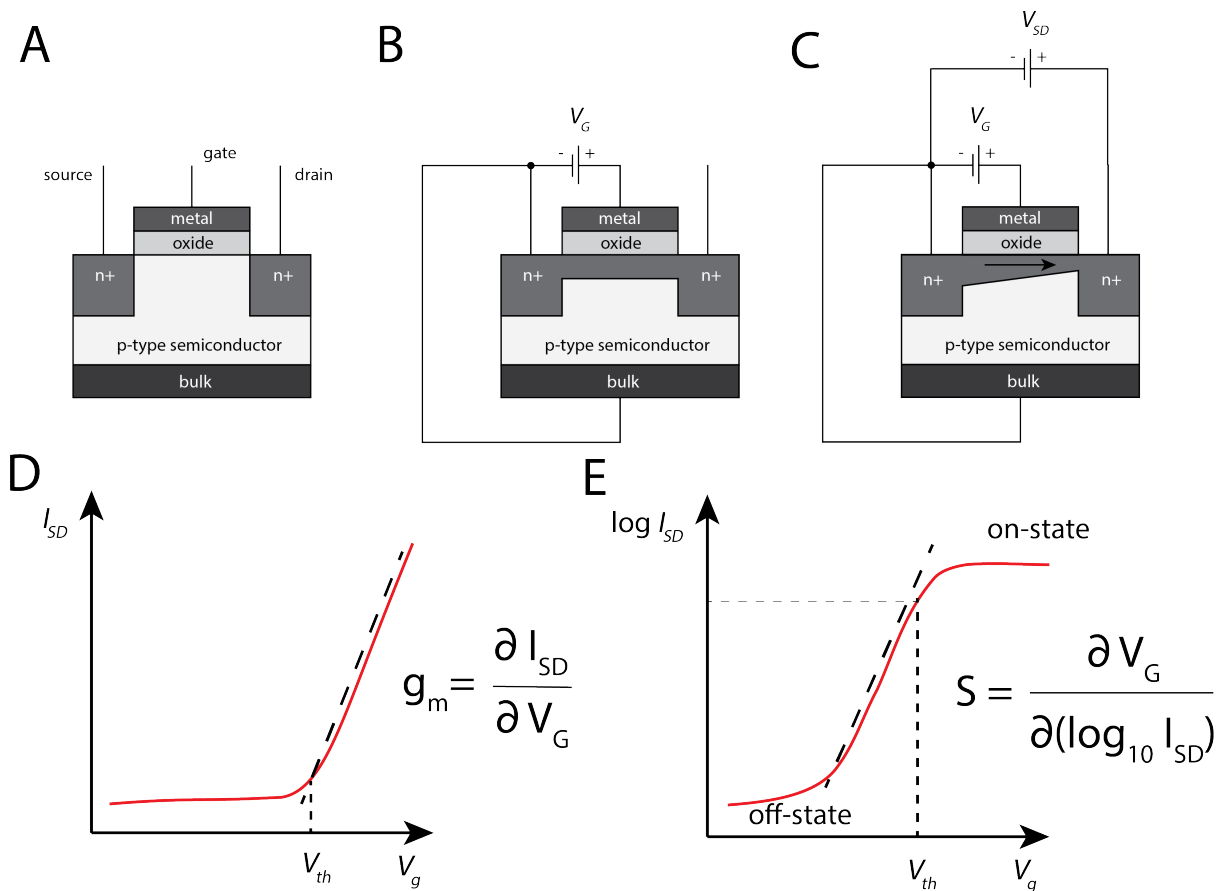


**Figure 1.10** – **A** Scheme of a typical *n*-channel MOSFET. The *p*-type semiconductor substrate (bulk) contains two *n*-doped regions (source and drain). A metal gate is placed on top of the semiconductor, isolated by a metal oxide. **B** When a positive voltage  $V_G$  between gate and source is applied, electrons are pulled from the bulk to the semiconductor/oxide interface thus creating an inversion channel. **C** If a positive voltage  $V_{SD}$  is applied between source and drain, electrons in the channel will migrate to the drain. The channel is narrowed by  $V_{SD}$  close to the drain. **D** Transfer curve of the *n*-type MOSFET ( $I_{SD}$  vs.  $V_G$ ) plotted in  $I_{SD}$  linear scale. The current is linearly depends on  $V_G$  above the threshold voltage  $V_{th}$ . There, the slope is called the transconductance  $g_m$ . Below the threshold voltage  $V_{th}$ , the current depends exponentially on the gate voltage  $V_G$ . **E** Transfer curve of the *n*-type MOSFET ( $I_{SD}$  vs.  $V_G$ ) plotted in  $I_{SD}$  semi-logarithmic scale. The exponential function is a straight line on a semi-log plot up to the threshold voltage  $V_{th}$ . The reciprocal slope of that function is called the subthreshold swing  $S$ .

The substrate is a p-type semiconductor, containing two n-doped regions acting as *source* and *drain* terminals. A metal *gate* is placed on top of the semiconductor isolated by a metal oxide. The doped regions are isolated from the substrate by p-n junctions. When a positive voltage is applied to the gate terminal, negative charge carriers (electrons) are attracted to the semiconductor/oxide interface thus creating an inversion layer (Fig. 1.10 B). If no current flows at  $V_{SD} = 0$ , the transistor is called "enhancement type" or "normally-off". When additionally a positive source-drain voltage  $V_{SD}$  is applied, the current  $I_{SD}$  starts to flow between the two terminals (Fig. 1.10 C).

The source-drain current  $I_{SD}$  through the channel is described by equation:

$$I_{SD} = \mu C_{ox} \frac{W}{L} Q V_{SD} = \mu C_{ox} \frac{W}{L} (V_G - V_{th}) V_{SD} \quad (1.13)$$

where  $\mu$  - charge mobility,  $C_{ox}$  - capacitance of the gate oxide per area,  $W$  - channel width,  $L$  - channel length,  $Q$  - charge density in the channel,  $V_{SD}$  - source-drain voltage,  $V_G$  - gate voltage and  $V_{th}$  - threshold voltage.

The consequence of the above equation is that if the gate voltage is much lesser than the threshold voltage  $V_G \ll V_{th}$ , there is no current flowing between the source and drain  $I_{SD}$ .

**Surface charge and surface potential** The immersion of some materials in electrolyte solution causes the surface charge to appear by dissociation of surface sites, adsorption of ions from solution, crystal lattice defects or an imbalance in number of lattice ions on the surface of an ionic crystal. Surface charges are the cause of an electric field attracting counter ions. According to the simplest model, the layer of surface charges and counter ions, which neutralize the surface charges, is called "*electric double layer*" or "Helmholtz layer" (see Fig. 1.11 A).<sup>47</sup> Here, the surface potential linearly dissipates from the surface to counter-ions. In a more advanced model by Gouy and Chapman, thermal fluctuations tend to drive the counterions away from the surface, which in consequence leads to the formation of a "*diffuse double layer*" (see Fig. 1.11 B).

The Stern's model (see Fig. 1.11 C) combines the Helmholtz model with the Gouy–Chapman model to explicitly account for the two different regions of charge – namely the Stern layer and the diffuse layer. Inside the Stern layer, one can discriminate two Helmholtz planes: inner (IHP), where the counter ions specifically adsorb on the interface, and outer (OHP) which is located on the plane of the centers of the next layer of non-specifically adsorbed ions. The diffuse layer, begins at the outer Helmholtz plane.

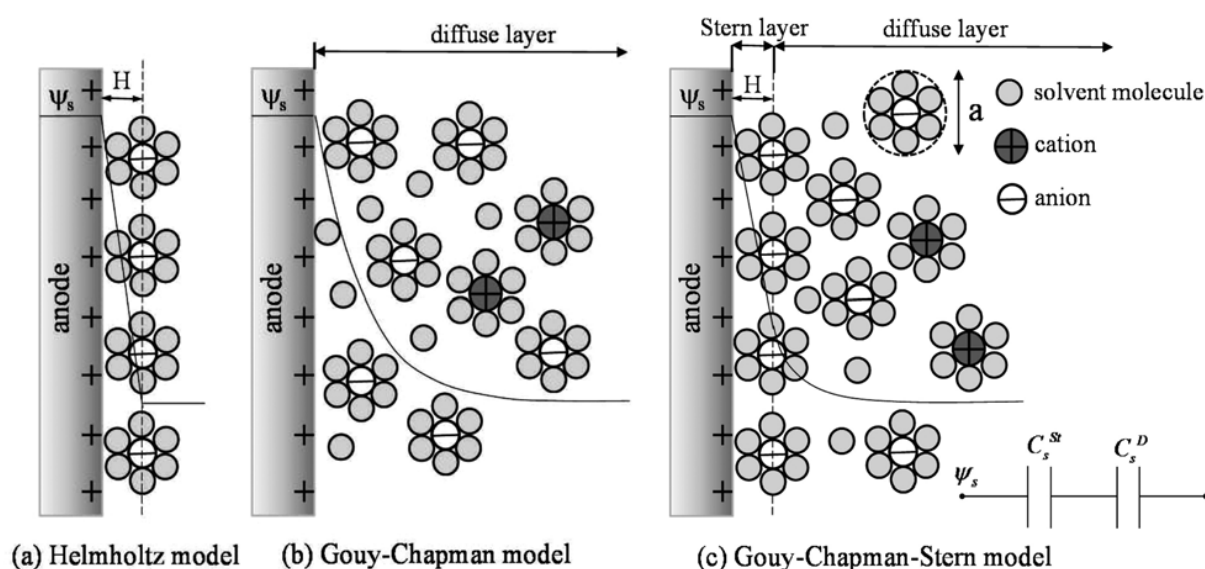


**Figure 1.11** – Schematic representations of EDL structures according to the **A** Helmholtz model, **B** the Gouy–Chapman model (b), and **C** the Gouy–Chapman–Stern model.  $H$  is the double layer distance described by the Helmholtz model.  $\Psi_s$  is the potential across the EDL. Reproduced from<sup>48</sup> with permission from the PCCP Owner Societies. Copyright 2014 Royal Society of Chemistry.

The relation between the counter ion concentration near the surface and the bulk counter ion concentration is subject to Boltzmann distribution and is given by an equation:

$$C = C_0 e^{-\left(\frac{-W}{k_B T}\right)} \quad (1.14)$$

where  $C$  is the counter ion concentration near the surface,  $C_0$  is the bulk counter ion concentration,  $W$  is work required to bring an ion closer to the surface from an infinitely far distance,  $\Psi$  is the surface potential,  $k_B$  - Boltzmann constant and  $T$  - temperature in Kelvin.

The electric work to move an anion or a cation to the surface with potential  $\Psi$  is equal to  $W^- = -e\Psi$  (for anion) and  $W^+ = e\Psi$  (for cation),<sup>49</sup> which transforms the Eq. 1.14 to:

$$C^- = C_0 e^{\left(\frac{\Psi e}{k_B T}\right)} \quad (1.15)$$

$$C^+ = C_0 e^{-\left(\frac{\Psi e}{k_B T}\right)} \quad (1.16)$$

where  $C^-$  and  $C^+$  is the local anion and cation concentration near the surface respectively,  $C_0$  is the bulk ion concentration,  $\Psi$  is the surface potential,  $e$  - elemental charge of electron ( $1.602 \times 10^{-19}$  C),  $k_B$  - Boltzmann constant and  $T$  - temperature in Kelvins.

Local volumetric electric charge density takes into account both anions and cation local concentration and is given by:

$$\rho_e = e(C^+ - C^-) \quad (1.17)$$

where  $\rho_e$  is the local electric charge density in  $C/m^3$ ,  $C^+$  is the local anion and cation concentration near the surface respectively,  $e$  - elementary charge of electron.

Furthermore, electrical potential and the local volumetric electric charge density are bound together with *Poisson's equation*:

$$\nabla^2 \Psi = \frac{\rho_e}{\varepsilon \varepsilon_0} \quad (1.18)$$

where  $\Psi$  is the surface potential,  $\rho_e$  is the local electric charge density in  $C/m^3$ ,  $\varepsilon$  is the dielectric constant (relative permittivity) of the solvent and  $\varepsilon_0$  is the permittivity of vacuum.

Merging the Eq. 1.14 and 1.18, a *Poisson-Boltzmann equation* is derived

$$\nabla^2 \Psi = -\frac{C_0 e}{\varepsilon \varepsilon_0} \left( e^{-\frac{\Psi e}{k_B T}} - e^{\frac{\Psi e}{k_B T}} \right) \quad (1.19)$$

where  $\Psi$  is the surface potential,  $C_0$  is the bulk ion concentration,  $\varepsilon$  is the dielectric constant (relative permittivity) of the solvent,  $\varepsilon_0$  is the permittivity of vacuum,  $e$  - elemental charge of electron,  $k_B$  - Boltzmann constant and  $T$  - temperature in Kelvins.

The Poisson-Boltzmann equation solution is the potential  $\Psi$  at a given distance, but is rather difficult to solve. Several solutions were proposed, including the *Debye-Hückel theory*, the main assumptions are: 1:1 salt solutions with cations of  $z$  valence and anions of  $-z$  and the spherical symmetry. The Eq. 1.19 is transformed to:

$$\nabla^2\Psi = \Psi \frac{2z^2 eFC_0}{k_B T \varepsilon \varepsilon_0} \quad (1.20)$$

$$\kappa^2 = \frac{2z^2 eFC_0}{k_B T \varepsilon \varepsilon_0} \quad (1.21)$$

where  $\Psi$  is the surface potential,  $z$  - charge of the ion,  $C_0$  - concentration of ions.

From the above, one can extract  $1/\kappa$ , which is a very important parameter in FET biosensing. It is called the *Debye length* ( $\lambda_D$ ) and can be expressed also with the following equation.<sup>50</sup>

$$\lambda_D = \sqrt{\frac{\varepsilon_0 \varepsilon_r k_B T}{2N_A q^2 I}} \quad (1.22)$$

where  $N_A$  is the Avogadro number,  $q$  is the charge on an electron, and  $I$  is the ionic strength of the solution.

**Debye screening** Debye length can be thought as a measure of a charge carrier's net electrostatic effect in a solution and how far its electrostatic effect extends. The potential distribution at a charged surface in contact with a liquid electrolyte predicts an exponential decay of the surface potential with increasing distance from the electrode  $x$  (see Fig. 1.12).

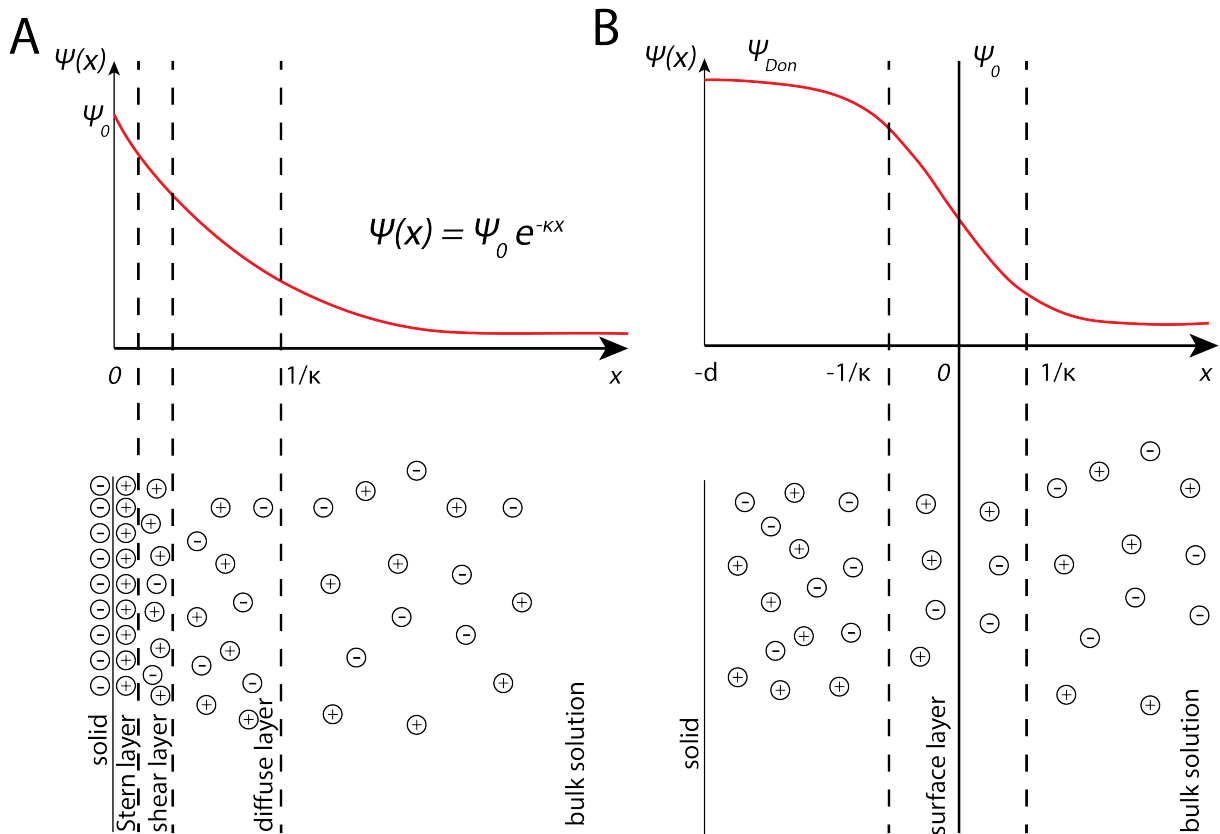


**Figure 1.12** – **A** Potential distribution vs. distance from electrode surface ( $x = 0$ ) with the potential decaying by  $1/e$  at the Debye length ( $1/\kappa$ ). **B** A surface layer separates the solid electrode surface from the liquid electrolyte. Ions are present within the surface layer resulting in a almost stable Donnan potential, which drops sigmoidal close to the surface layer/electrolyte interface. The decay is determined by the Debye length  $1/\kappa$  but starts further away from the sensor surface compared to **A**.

Debye screening has so far limited application of FET-based biosensors in real samples. An increase in ion concentration reduces the Debye length due to charge screening by counter-ions.<sup>51</sup> Thus, the Debye screening length, which is a physical distance where the charged analyte is electrically screened by the ions in the medium, strongly affects the biosensor sensitivity in high ionic strength buffers.

The Debye length is inversely proportional to the square root of the ionic strength (see Equation 1.22). For example, in 1 mM ionic strength aqueous solution, the Debye length is approximately 10 nm, while in physiological solutions, where the ionic strength  $\sim 150$  mM, it is merely 0.3 nm.

To overcome the Debye screening, the following solutions have been proposed: i) dilution of the fluid sample, ii) addition of a signal-enhancing label ("electronic ELISA"),

iii) the use of shorter receptors such as aptamers<sup>6,52,53</sup> and antibody fragments,<sup>54</sup> iv) high-frequency measurements<sup>55</sup> and, more recently, v) local desalting by a polyethylene glycol layer (PEG).<sup>5,6</sup> While highly effective in avoiding the Debye screening, the first two approaches i) and ii) require pre-treatment of physiological samples, additional reagents, washing buffers, and more complex liquid handling, which results in higher assay cost and longer measurement times.

A solution to the Debye screening problem is proposed in the later chapters, where semiconducting SWCNTs (Chapter 2) or graphene (Chapter 3) were used in as channels in an electrolyte-gated field-effect transistor based immunosensors in physiological conditions. Additional polymer (poly(ethylene glycol), PEG) layer was added, which can be thought as the surface layer described in the Donnan model<sup>56</sup> (see Fig. 1.12), where potential at the solid surface (the Donnan potential  $\Psi_{Don}$ ) remains almost constant within the surface layer due to presence of ions in this layer. The Debye screening starts to play a role further away from the electrode surface, namely close to the surface layer/electrolyte interface. In this case, if an analyte binding event take place within the surface layer, then a significant portion of its charge may be still detectable.

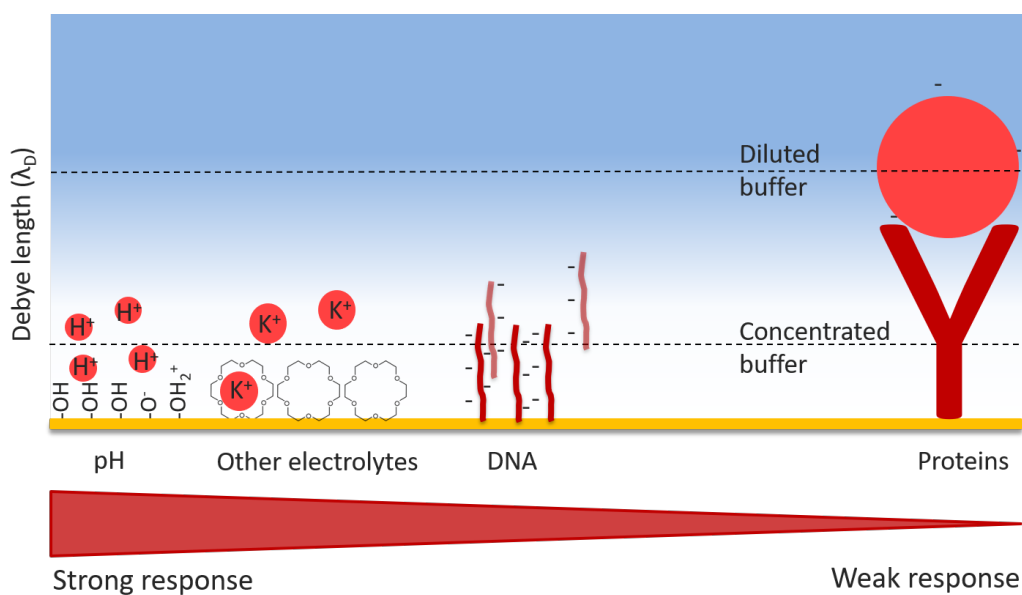


**Figure 1.13** – An illustration of Debye screening limitation in FET-based (bio)sensors. In low ionic strength solutions, it is possible to sense binding events far away from the surface (antigen-antibody interactions), while in high ionic strength solutions, so far only small, highly charged objects like ions or short DNA sequences were possible to detect.

### Electrolyte-gated field-effect transistor

Electrolyte-gated field-effect transistors differ significantly from classical ion-sensitive FETs. As mentioned in the previous subsection, in the "classical" FET, the channel of the transistor is covered with dielectric on top of which a gate electrode can be placed (Fig. 1.14 A). In the EGFET configuration, the semiconducting channel is in direct contact with an electrolyte instead of a conventional dielectric (Fig. 1.14 B).

The electrolyte covers the semiconductor surface and the mobile ions are even able to penetrate into porous semiconductors. When a negative (positive) voltage is applied to the gate electrode, the cations (anions) and anions (cations) move within the electric field and accumulate at the gate and the semiconductor, respectively. An electric double-layer (see Paragraph 1.2.2) at the electrolyte/semiconductor interface as well as the gate electrode/electrolyte interface is formed. Additionally, compensating opposite charge carriers are injected and accumulated within the semiconductor. Due to the nanometer thickness of the electric double-layer, the effective capacitance of the liquid electrolyte as the gate dielectric is in the range of 1-100  $\mu\text{F}/\text{cm}^2$  and is about 1000 times higher than the conventional silicon dioxide ( $\text{SiO}_2$ ) dielectric layer in a MOSFET.<sup>57</sup>

Also, voltages applied used for EGFETs are typically much smaller than those necessary for "standard" FETs and must not exceed the water splitting voltages ( $<1.5\text{ V}$ , *vs.*  $>10\text{ V}$  or even higher). Additionally, the adsorption of species on the surface of liquid exposed channel can change the transistor's characteristics in many ways:<sup>58</sup> 1) electrostatic gating, 2) Schottky barrier effect, 3) capacitance change and 4) charge carriers mobility change. These three characteristics (electrolyte compatibility, direct adsorption of species on the surface and low gating potentials) make EGFETs ideal candidates for the next generation of biosensors, particularly suitable for the detection and quantification of biological molecules inside aqueous media. With the advances of nanotechnology, new semiconducting materials were used as a channel in electrolyte-gated field-effect transistors, e.g. graphene.<sup>59,60</sup>

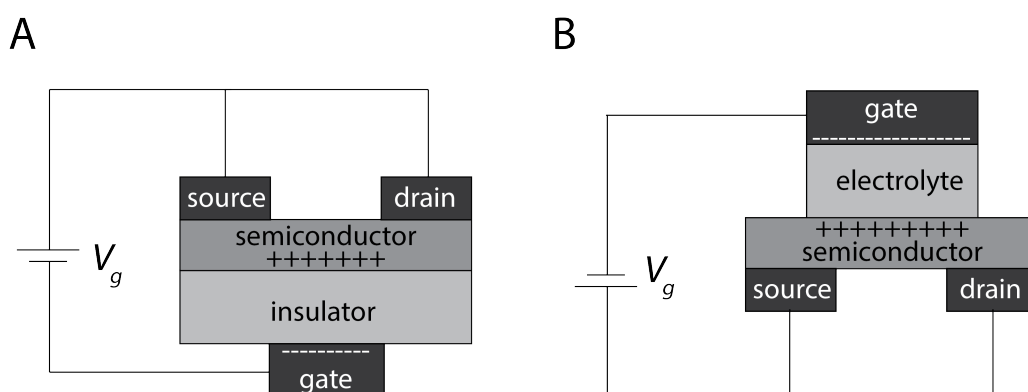


**Figure 1.14** – General scheme of an field-effect transistor (FET) (A) and an electrolyte-gated field-effect transistor (EGFET) (B).

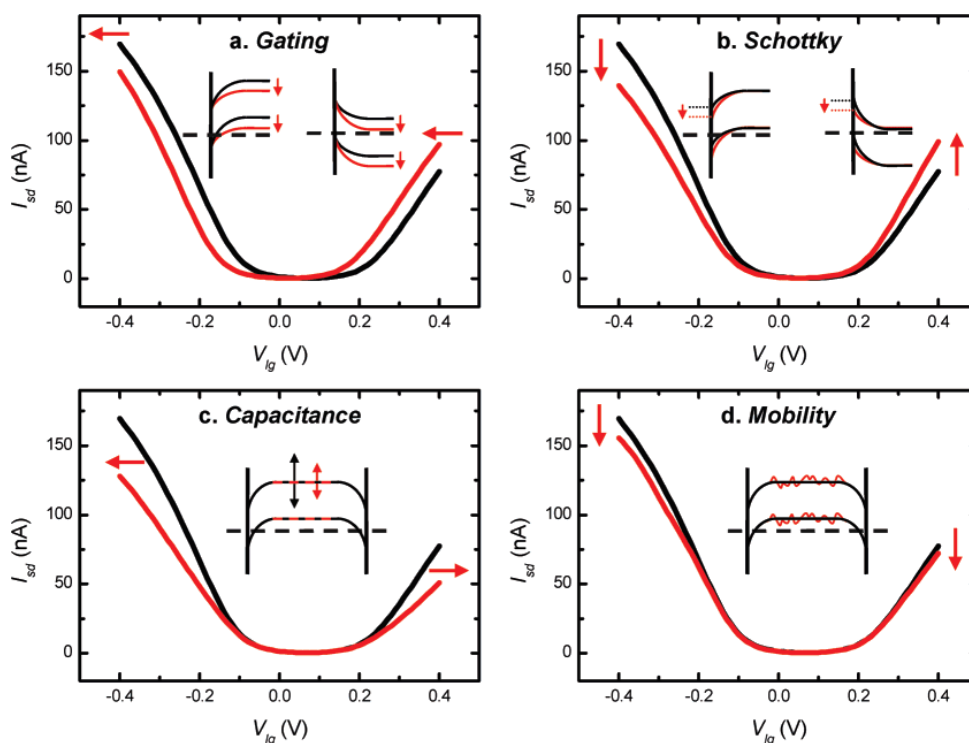
**Mechanisms of biosensing with carbon nanotube/graphene electrolyte gated transistors** Although electrolyte-gated CNT field-effect transistors have been first described in 2002,<sup>61</sup> until now, the physical mechanism that the (bio)sensing is based on, is still debatable.<sup>62</sup> Despite having significant differences, the mechanisms status expands also to electrolyte-gated graphene FETs. Among candidates to the title of "biosensing mechanism of CNT/graphene FET" are: 1) electrostatic gating effect,<sup>63-65</sup> 2) Schottky barrier effects,<sup>66-68</sup> 3) changes in gate coupling,<sup>69</sup> 4) charge scattering across the nanomaterial.<sup>70</sup>

Figure 1.15 A shows the first mentioned mechanism - *electrostatic gating*. The phenomenon that occurs here is that the adsorbed charged species induce a screening charge (doping) in the semiconducting carbon nanomaterial and thus shift the transfer curve ( $I_{SD}$  vs.  $V_g$ ). For example, positively charged molecules induce additional negative charge in the nanomaterial causing n-doping and consequently shifting the transfer curve to more negative gate voltages, and vice versa, negatively charged species cause p-doping and the transfer curves to shift to more positive potentials.

The Schottky barrier effect (shown in Fig. 1.15 B) is based on adsorption of (bio)molecules at the metal contacts that modulate the local work function and thus the band alignment. The Schottky barrier (semiconductor/metal) changes in opposite directions for hole (p) and electron (n) transport (Fig. 1.15 B, inset) resulting in characteristic asymmetric conductance change for hole and electron branches of a transfer curve.

Low permittivity of adsorbed molecules (relative to the electrolyte) is the reason for the reduction in gate capacitance (Fig. 1.15). For SWCNTs, the electrolyte interfacial capacitance is dominated by the quantum capacitance of SWCNTs.<sup>61</sup> Thus the electrostatic capacitance reduction due to biomolecule adsorption can only be the case for nearly full surface coverage with said biomolecules. In that situation, permeation of ions through the biomolecule layer can be hindered, but so far is a subject to dispute.<sup>71</sup>

The fourth proposed mechanism relies on the change in mobility of charge carriers in the carbon nanomaterial (Fig. 1.15 D). This mobility is proportional to the effective scattering time (time that the charge carrier travels through the atomic lattice before it is scattered). There are two major sources of scattering of charge carriers in carbon nanomaterials: intrinsic (specific to the nanomaterial itself) and extrinsic, which can happen due to presence of neutral and charged impurities, defects etc. In principle, if an adsorbed biomolecule is treated as an "impurity" at the surface of carbon nanomaterial, it can change the charge carrier mobilities as shown in Fig. 1.15.



**Figure 1.15** – Calculated  $I$ - $V_g$ -curves before (black) and after (red) protein adsorption for four different sensing mechanisms. The bias voltage is 10 mV. **A** Electrostatic gating effect corresponding to a 50 meV shift of the semiconducting bands downward. **B** Schottky barrier effect that corresponds to a change of the difference between metal and SWNT work functions of 30 meV. In panels a and b, left and right insets illustrate the corresponding changes in the band diagrams for hole and electron doping respectively. **C** Capacitance mechanism for a 90% coverage of SWCNT with protein. In panels c and d, the insets illustrate the corresponding changes in the band diagrams. **D** Mobility mechanism that corresponds to a mobility reduction to a mere 2% of the initial value. Reprinted with permission from.<sup>58</sup> Copyright 2008 American Chemical Society."

### 1.2.3 Surface characterization methods

#### Raman spectroscopy

Raman spectroscopy is a powerful spectroscopic technique based on inelastic scattering of monochromatic light (mostly laser). The frequency of photons emitted by a laser changes upon interaction with a sample: photons are scattered by the surface, which changes their frequency (*shift* up or down called Raman effect). Those shifts provide information about vibrational, rotational and other low frequency transitions in molecules. Study of solid, liquid and gaseous samples is possible with Raman spectroscopy.

Raman spectroscopy can be used for characterization of various carbon based (nano) materials disordered and amorphous carbons, fullerenes, diamonds, carbon chains and polyconjugated molecules and most importantly for this work - for carbon nanotubes<sup>72</sup> or graphene.<sup>73</sup>

Raman techniques are particularly useful for graphene because the absence of a band-gap makes all wavelengths of incident radiation resonant, thus the Raman spectrum contains information about both atomic structure and electronic properties.<sup>74</sup> It can provide information about the layer structure (number) of graphene and the density of defects. For example, perfect single-sheet graphene the intensity ratio of 2D to G should follow the rule  $\frac{I_{2D}}{I_G} \gg 1$ .

Typical graphene Raman spectra are shown in the Fig. 1.16a. The G band ( $1580 \text{ cm}^{-1}$ ) is an in-plane  $\text{sp}^2$  C-C stretching mode, the 2D band ( $2675 \text{ cm}^{-1}$ ) originates from an in-plane breathing-like mode of the carbon rings. The D-band resonance ( $1350 \text{ cm}^{-1}$ ) is a disorder-induced scattering process and is observed when there is symmetry breaking on the hexagonal  $\text{sp}^2$ -bonding lattices. The observation of a D band in the Raman spectra is, therefore, related to either the presence of defects (e.g., vacancies, dopants) or to the presence of amorphous-carbon material in the sample.

Typical carbon nanotube Raman spectra are shown in the Fig. 1.16b. Raman spectroscopy allows to distinguish the diameter of the carbon nanotubes. The spectra show characteristic for CNTs: the radial breathing modes (RBM), D-band, G-band and G' band features, in addition to weak double-resonance features associated with the M-band and the iTOLA second-order modes. The RBM is unique to carbon nanotubes and is not observed in other carbon materials. It has the very important property that is the RBM mode frequency is proportional to the inverse tube diameter. The G band in SWNTs is composed of two stronger peaks ( $G^+$  and  $G^-$ ) related to the circumferential (TO) and axial (LO) atomic vibrations.<sup>75</sup>

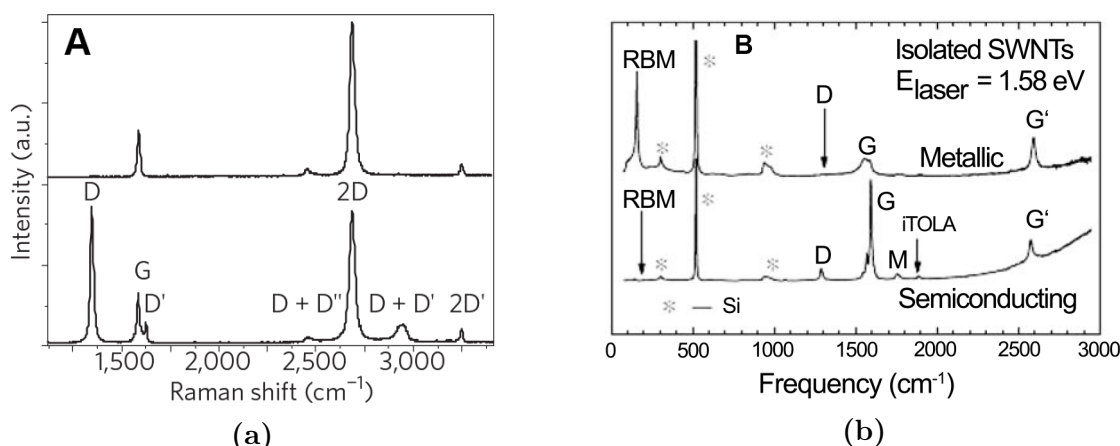


**Figure 1.16** – **A** Raman spectra of pristine (top) and defected (bottom) graphene. The main peaks are labelled. Reprinted with permission from.<sup>74</sup> Copyright 2013 Nature Publishing Group. **B** Raman spectra from a metallic (top) and a semiconducting (bottom) SWNT at the single-nanotube level. Reprinted from<sup>75</sup> with permission. Copyright 2005 Elsevier.

### Quartz crystal microbalance

An analytical technique allowing us to directly measure mass changes on the surface upon binding (surface modification, biosensing) is quartz crystal microbalance. This technique, established in 1964<sup>76</sup> is based on a piezoelectric property of quartz - upon applied voltage, the quartz crystal oscillates. When molecules interact with the surface of the crystal, the frequency of oscillations changes (binding - decreases, unbinding - increases). A QCM chip consists of a thin disk of single crystal quartz, with metal electrodes deposited on each side of the disk and the AC voltage is applied across the crystal, causing vibrational motion of the crystal at its resonant frequency.

Sauerbrey<sup>77</sup> first showed that in vacuum the amount of added mass to the electrodes is linearly related to the resulting shift in resonant frequency of the oscillator:

$$\Delta m = -C\Delta f \quad (1.23)$$

where  $\Delta m$  is the mass change,  $C$  is a constant that depends only on the thickness of the quartz slab and on the intrinsic properties of the quartz (for commonly used 5 MHz fundamental frequency crystals  $C = 17.7 \text{ ng/Hz}$ <sup>78</sup>) and  $\Delta f$  is the frequency change. The Sauerbrey equations rely on the following assumptions: 1) the added mass is evenly distributed over the electrode(s) and is much smaller than the weight of the quartz disk, i.e.,  $\Delta f \ll f$ , 2) the mass is rigidly attached to the electrodes, with no slip or deformation due to the oscillatory motion. Those assumptions limit the use of Sauerbrey equation when working with liquids and biological samples due to viscoelastic properties and uneven distribution of adsorbed species on the surface under study.<sup>79</sup>

Another important feature of QCM is the ability (in some configurations) to measure the dissipation (the loss of energy per oscillation period divided by the total energy stored in the system). Basically, when the AC voltage is turned off, the oscillation decays exponentially ("rings down") and is recorded to extract the resonance frequency and the dissipation factor ( $D$ ). Dissipation can also be expressed as the resonance bandwidth divided by the resonance frequency. The dissipation gives additional information about

the rigidity of the layers adsorbed on the surface of the crystal - when soft layers (e.g. PEG) are adsorbed, the dissipation increases, whereas when rigid layers are formed - decreases. QCM has also been used in liquids<sup>80</sup> and coupled with electrochemistry<sup>81</sup> became a powerful method for biosensing.

## 1.3 Carbon based nanomaterials

Carbon is one of the most widespread elements in the universe and the one that life as we know it, is based on. Due to its electron configuration  $(1s)^2(2s)^2(2p)^2$ , it is able to form different kinds of covalent bonds, including catenation - the property to form long chains of its own atoms. Elemental carbon may occur in different allotropes having the same hybridization, for example  $sp^2$  - fullerene (0 dimensional), carbon nanotubes (1 dimensional), graphene (2 dimensional), graphite (3 dimensional).<sup>82</sup> The article that started the carbon nanotube trend was published in 1991<sup>3</sup> and from then, the interest in CNTs only rose 1.17. The experimental proof for graphene was published in 2004<sup>4</sup> and it attracted thousands of researchers (Fig. 1.17). In 2018, the number of records in Scopus database for "graphene" exceeded 100.000 and in 2016 the number of records for "graphene" was for the first time in history higher than the number of records for "carbon" AND "nanotubes" query. Since carbon nanotubes can be treated as rolled-up graphene, graphene basic properties need to be addressed before introducing carbon nanotubes. Both carbon nanotubes and graphene are proven to be applicable in the Point-of-Care diagnostic devices and due to their unique properties, they make the devices highly sensitive, specific, rapid in analysis, low cost, and easy to use. Biosensors based on CNTs and graphene are improved in terms of portability, functionality, reliability, and real-time diagnosis for Point-of-Care analysis.<sup>83</sup> The basic properties of both carbon nanotubes and graphene will be discussed in this section.

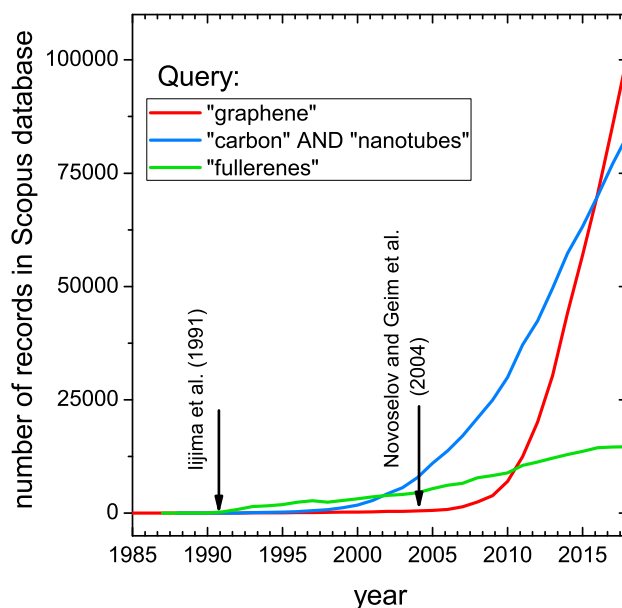


**Figure 1.17** – Number of records in Scopus database every year from 1985 to 2018 for the queries: "fullerenes", "carbon" AND "nanotubes", and "graphenes", respectively. Note the increase in records after two milestones: official carbon nanotubes "discovery" by Iijima et al. (1991)<sup>3</sup> and official graphene "discovery" by Geim and Novoselov et al. (2004).<sup>4</sup> Data retrieved and analysis done on 24.04.2019 from [www.scopus.com](http://www.scopus.com) online scientific publication database.

### 1.3.1 Graphene

Graphene is a flat monolayer of carbon atoms in a honeycomb lattice.<sup>84</sup> As mentioned before,  $sp^2$  hybridized carbon atoms in graphene are bonded *via*  $\sigma$  bonds. Due to its hybridization, each carbon atom has an unpaired electron ( $\pi$  electron), which due to the structural symmetry is delocalized. Because of this delocalized electrons, graphene possesses high electrical conductivity and the extremely high mechanical resistance of graphene comes from very short C-C bonds - 0.142 Å compared to 0.154 Å in diamond ( $sp^3$  hybridized carbon atom crystal).<sup>85</sup>

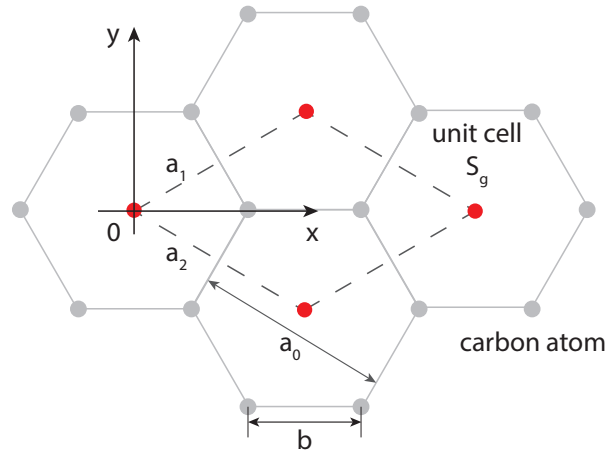


**Figure 1.18** – Bravais lattice of graphene.  $\mathbf{a}_1$  and  $\mathbf{a}_2$  are the basis vectors of same length ( $|\mathbf{a}_1| = |\mathbf{a}_2| = a_0 = \sqrt{3}b$ ), which form a  $\pi/3$  ( $60^\circ$ ) angle,  $b \approx 1.42$  Å - carbon-carbon bond length.

The unit cell is spanned by the two vectors,  $\mathbf{a}_1$  and  $\mathbf{a}_2$  and contains two carbon atoms. The basis vectors ( $\mathbf{a}_1$ ,  $\mathbf{a}_2$ ) are of the same length,  $|\mathbf{a}_1| = |\mathbf{a}_2| = a_0 = \sqrt{3}b$  and form an angle  $\pi/3$  ( $60^\circ$ ), where  $a_0$  is the lattice constant and  $b \approx 1.42$  Å is the carbon-carbon bond length. The components of those vectors are, respectively:  $a_1 = (\sqrt{3}/a_0, a_0/2)$ ,  $a_2 = (\sqrt{3}/a_0, -a_0/2)$ . Additionally, the surface area of the cell can be calculated -  $A_g = \sqrt{3}a_0^2/2$ .

Due to hexagonal honeycomb lattice of graphene, with two carbon atoms per unit cell (Fig. 1.19 A), graphene exhibits unique electronic properties<sup>86</sup>(Fig. 1.19 B). The valence band is formed by the  $\pi$ -states and the conduction band by the  $\pi^*$ . The two bands touch at six points, the so-called Dirac or neutrality points. Due to the high symmetry, they can be reduced to a pair, K and K', which are independent of one another. In the low energies regime (relevant for electron transport), the bands exhibit a linear dispersion and the band structure can be displayed as two cones touching at  $E_{Dirac}$  (Fig. 1.19 C, D). The two bands touching at  $E_{Dirac}$  indicates that graphene is a zero-band semiconductor (sometimes referred to zero-overlap semimetal) and because of the symmetric band structure, graphene exhibits ambipolar behaviour: both electrons and holes being the charge carriers<sup>82</sup> with Fermi velocities of  $\nu_F \approx 10^6$  m/s.<sup>87</sup>

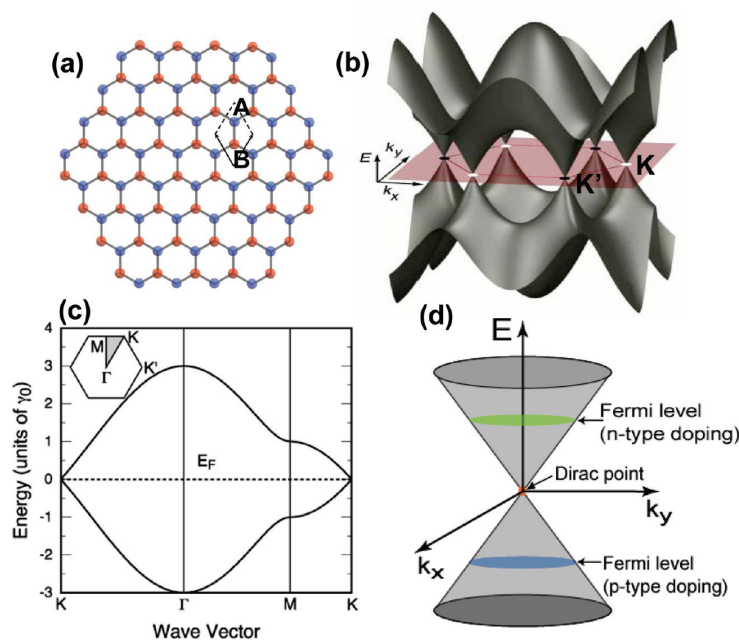


**Figure 1.19** – **A** Hexagonal honeycomb lattice of graphene with two atoms (A and B) per unit cell. **B** The 3D bandstructure of graphene. **C** Band structure of graphene plotted along the symmetry points. **D** Approximation of the low energy bandstructure as two cones touching at the Dirac point. The position of the Fermi level determines the nature of the doping and the transport carrier. Reprinted with permission from.<sup>86</sup> Copyright 2010 American Chemical Society.

## Graphene synthesis

Graphene synthesis can be divided into two subgroups taking into account the strategy: top-down (e.g. mechanical exfoliation) and bottom-up (e.g. chemical vapour deposition - CVD).<sup>88</sup> Briefly, top-down (TD) fabrication strategy implies that there is a bulk (bigger) starting material (graphite) which can be turned into the desired (smaller) material (graphene) by means of machining like e.g. cutting, exfoliation or ablation. The bottom-up (BU) on the other hand is based on fabrication of the material (graphene) from its elementary parts (carbon containing gases). Historically, TD has been applied first in e.g. silicon industry.<sup>89</sup>

Graphene was first mechanically exfoliated on purpose in 2004<sup>4</sup> using the scotch tape method: the graphite flakes were spread on a substrate, a piece of scotch tape was glued attached and then peeled-off to separate the layers of graphite. After several iterations of this low-budget process, graphene flakes could be obtained. This work initiated a graphene revolution or "graphene rush". Other top-down methods include liquid exfoliation starting from graphite using modified Hummer's method to obtain graphene oxide (GO)<sup>90</sup> and then reducing the graphene oxide to obtain reduced graphene oxide (rGO). The biggest problem of TD methods is that it is not possible to obtain large scale high quality uniform graphene layers.

Epitaxial growth on silicon carbide (SiC) is an interesting alternative for acquiring high-quality few-layer and large scale graphene sheets. Briefly, due to difference in vapor pressures between carbon and silicon, the Si atoms from an annealed SiC surface (>1000 °C) desorb leaving the C atoms, which form graphitic layers. The process is

normally performed in (ultra-)high vacuum giving a few-layer graphene. Interestingly, using argon environment instead and temperatures above 1650 °C, it is possible to obtain single-layer graphene.<sup>91</sup>

More recently, chemical vapor deposition (CVD) from carbon containing gases on catalytic metal surfaces became a wide-spread graphene growth technique. Starting from nickel as the growth substrate and achieving from 1-12 graphene layers,<sup>92</sup> to copper to achieve a purely surface mediated, self limiting process that stops after a monolayer is formed.<sup>93</sup> Various other graphene-CVD processes were developed and optimized over the last ten years.<sup>94</sup>

Although the mechanical exfoliation of graphene provides very high quality and purity, the size of obtained flakes is very small and not suitable for industrial applications. On the other hand, graphene growth on surfaces via e.g. CVD or epitaxial methods, allows a much larger size of the graphene layers and a high controllability, which is the pre-requisite for industrial production.

To use a CVD grown graphene in e.g. constructing a field-effect transistor, a transfer process needs to be performed. One of the most widespread methods is to coat the as-grown graphene on copper foil with poly(methyl methacrylate) (PMMA)<sup>95</sup> as a protection layer. The next step is to wet etch the copper (e.g. with  $(\text{NH}_4)_2\text{S}_2\text{O}_8$ ) resulting in graphene covered with PMMA floating on the surface of the aqueous solution of the etchant. After transferring into clean solvent ( $\text{H}_2\text{O}$ ), graphene/PMMA can be collected with an arbitrary substrate ( $\text{SiO}_2$ , glass, PET etc.) and further processed (e.g. patterning, removing PMMA with acetone).

The growth of graphene and transfer process into the final substrate have a huge influence on the performance of the manufactured device. Continuous CVD graphene films are usually polycrystalline and with small grain size (several micrometers). The grain boundaries between each grain of graphene were found to negatively impact both charge carrier transport and mechanical properties.<sup>94</sup> During the transfer process, since the less-than-nanometer thick and micro- to millimeter sized graphene is handled with macroscale methods and techniques (e.g. wet etching, PMMA removal, baking etc.), holes and ripples can occur which naturally would again affect the properties of the final graphene device.

### 1.3.2 Carbon nanotubes

Carbon nanotubes can be imagined as rolled-up graphene sheets with up to 3 nm in diameter - single-walled NTs, and up to 100 nm in diameter - multi-walled NTs, and typically up to  $\mu\text{m}$  length. Since there are many ways of selecting a stripe to roll up, there are correspondingly many different nanotube structures. The nanotube nomenclature is based on a graphene sheet chirality vector (Fig. 1.20 A).  $T$  is the nanotube axis, and  $C$  is the "roll up" vector.  $a_1$  and  $a_2$  are the unit vectors of graphene and  $n$  and  $m$  are the indices. There are basically 3 different types of single-walled nanotubes, based on the  $(n,m)$  nomenclature (Fig. 1.20 B):

- $(n,0)$  - when  $m = 0$ , the nanotube is a zigzag type (achiral)
- $(n,n)$  - when  $n = m$ , the nanotube is an armchair type (achiral)
- $(n,m)$  - all the other  $n$  and  $m$  combinations

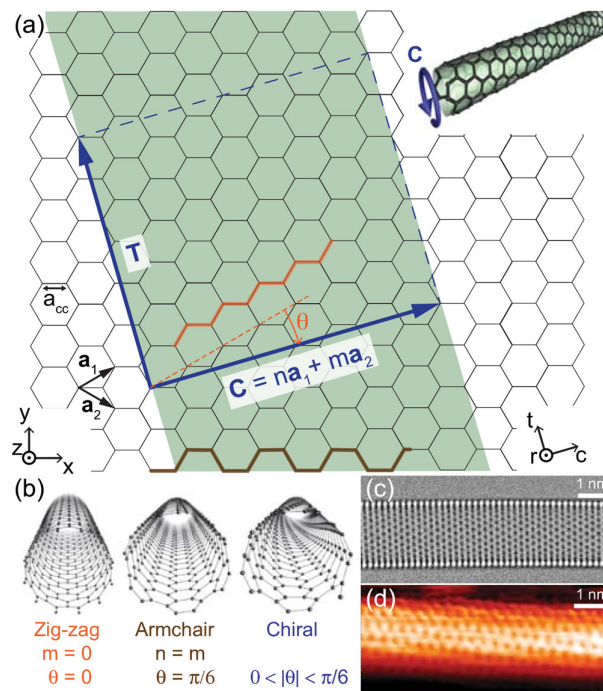


**Figure 1.20** – Atomic structure of carbon nanotubes. **A** Derivation of nanotube structure from graphene. A single-walled nanotube is equivalent to a rolled-up graphene stripe (shaded, with the direction of rolling chosen so that the printed pattern faces outward). The chiral vector  $C$  spans the nanotube circumference (inset) and connects lattice sites that are brought together by rolling up. The unit cell of the nanotube (much larger than the unit cell of graphene) is outlined by dashed lines, and the unit vector  $T$  is indicated. Graphene coordinates  $(x, y, z)$ , nanotube coordinates  $(t, c, r)$ , and the chiral angle  $\Theta$  are also marked. **B** Nanotubes are divided into three classes according to their chiral indices: zigzag, armchair, or chiral. **C** Carbon nanotube imaged by transmission electron microscopy (TEM). **D** Carbon nanotube imaged by scanning tunneling microscopy (STM). Reprinted with permission from<sup>96</sup> Copyright 2015 by the American Physical Society.

Zigzag and armchair nanotubes are so called because of the shape of the edge formed by a cut perpendicular to the nanotube axis. Electronic band structure calculations predict that the  $(n,m)$  indices determine whether a SCWNT is a metal or a semiconductor.<sup>97</sup> For a given  $(n,m)$  nanotube, if  $n = m$ , the nanotube is metallic; if  $n - m$  is a multiple of 3 and  $n \neq m$  and  $n \times m \neq 0$ , then the nanotube is quasi-metallic with a very small band gap, otherwise the nanotube is a semiconductor.<sup>96</sup>

The diameter of the nanotube can be calculated using the following equation:<sup>85</sup>

$$d = \frac{a}{\pi} \sqrt{(n^2 + nm + m^2)} \quad (1.24)$$

where  $d$  is the diameter,  $a = 0.246$  nm and  $n$  and  $m$  are the parameters from the rolling vector.

In a tight-binding model, the diameter of SWCNTs can be used to approximate the band gap using the equation:<sup>98</sup>

$$E_g = \gamma \left( \frac{2b}{d_{CNT}} \right) \quad (1.25)$$

where  $\gamma$  is the hopping matrix element ( $\sim 3$  eV),  $b$  is the C-C bond length and  $d_{CNT}$  is the carbon nanotube diameter.

### Carbon nanotube synthesis

Almost all carbon nanotube synthesis methods require a solid substrate and a gaseous precursor. The three main techniques are: 1) carbon arc discharge, 2) laser ablation and, a family of techniques mostly explored 3) chemical vapor deposition (CVD). Arc discharge nanotube synthesis is based on flowing a high current between two graphite electrodes (often catalyst - Co, Ni, Fe covered) in gas (helium mostly, methane or hydrogen is also used) atmosphere thus creating an electrical arc between them (which can heat the system up to 1700 °C).<sup>99</sup> The carbon atoms evaporate from the anode and deposit on the cathode in a form of carbon nanotubes. By using of high-power laser vaporization (yttrium aluminum garnet (YAG) type), a quartz tube containing a block of pure graphite is heated inside a furnace at 1200 °C, in an Ar atmosphere.<sup>100</sup> The aim of using laser is vaporizing the graphite within the quartz. Finally, the chemical vapor deposition technique, like with graphene, enables fine tuning of the quality and type of carbon nanotubes. For CNT synthesis, the most used CVD type is catalytic CVD including thermal and plasma assisted processes. Briefly, a heated reactor to  $\sim 700$  °C is fueled with carbon containing gases, which break down on catalyst (metal nanoparticle - Ni, Co, Fe) covered substrate (Si) with holes, serving as a nanotube growth template.<sup>101</sup>

A special type of CVD worth mentioning is high-pressure carbon monoxide disproportionation (HiPCO), which results in high purity (99%) single-walled carbon nanotubes with small diameters (0.8 - 1.2 nm).<sup>102</sup> Another example of "special" CVD is CoMoCat - perhaps the most scalable process which uses a fluidized bed reactor similar to those used in petroleum refining, albeit, currently on a much smaller scale.<sup>103</sup> The supported catalyst approach provides a substantial degree of chirality control during synthesis. Both of the methods are commercialized.

Synthesizing high purity carbon nanotubes pose no problem nowadays. The challenging part for the application of SWCNTs in devices like transistors or logic gates is their

polydispersity and thus mix of metallic and semiconducting nanotubes. A number of methods to select only the SWCNTs of desired qualities were developed including DNA wrapping, density gradient ultracentrifugation, gel chromatography, and conjugated polymer wrapping.<sup>104</sup> Selective dispersion by wrapping with conjugated polymers has become one of the most effective and popular methods to produce semiconducting nanotube dispersions with high selectivity (>99.8 % s-SWCNTs) and high yield.<sup>105</sup> Depending on the chosen nanotube raw material and wrapping polymer the obtained dispersions contain mixtures of certain semiconducting SWCNT species with different diameters and thus different bandgaps.

While being extremely promising due to their high sensitivity, single walled carbon nanotube field-effect transistors have faced significant fabrication challenges, in part because the selective production of semiconducting CNTs is very difficult and the presence of metallic CNTs can compromise the transistor performance and device reproducibility. Recently, tremendous progress has been made in CNT separation, and high performance transistors based on CNTs networks have been demonstrated.<sup>106,107</sup> Although there has been several notable articles about biosensors made from semiconducting CNT networks,<sup>108,109</sup> the field seems to be underexplored.

### 1.3.3 Graphene and CNT comparison

Since both the nanomaterials were used in this work, it is worthwhile to compare the two. When it comes to the charge transport properties of graphene and carbon nanotubes, it seems that they are highly similar. Both the nanomaterials exhibit ambipolar (both hole and electron) transport<sup>86</sup> and the electric capacity for both was reported to be above  $10^9 \text{ A cm}^{-2}$ .<sup>110,111</sup> The carrier mobility in semiconducting single-walled carbon nanotubes was measured to be  $80,000 \text{ cm}^2\text{V}^{-1}\text{s}^{-1}$ ,<sup>112</sup> while the mobility of exfoliated graphene ranges from  $100,000 \text{ cm}^2\text{V}^{-1}\text{s}^{-1}$ <sup>113</sup> on insulating substrates to  $230,000 \text{ cm}^2\text{V}^{-1}\text{s}^{-1}$  for suspended graphene.<sup>87</sup> However, there are also other, more basic differences i.e. dimensionality (1D *vs.* 2D) and the presence of a band gap in semiconducting nanotubes. From the practical point of view, nanotubes, being heterogeneous in diameter and type, make producing a well-defined starting material for technology, a problem. Also, CNT network FET require the positioning of the CNTs in a specific direction, with desired density. Graphene, on the other hand, is well-defined and its planar geometry allows the use of the highly advanced semiconductor industry techniques. The highest achieved so far ON/OFF ratios for graphene transistors are  $\sim 10$ ,<sup>114</sup> while the SWCNT network transistors<sup>105,115,116</sup> easily exceed  $10^6$ . A good overview of electrolyte-gated SWCNT network FET *vs.* graphene FET transfer curves is shown in the Fig. 1.21. In this particular case, Trivial Transfer Graphene (commercially available single-sheet CVD grown graphene transferred into a hydrogel making the transfer process trivial) used as a FET transducer in Chapter 3 and polymer sorted semiconducting SWCNT network FET used in Chapter 2 are presented.

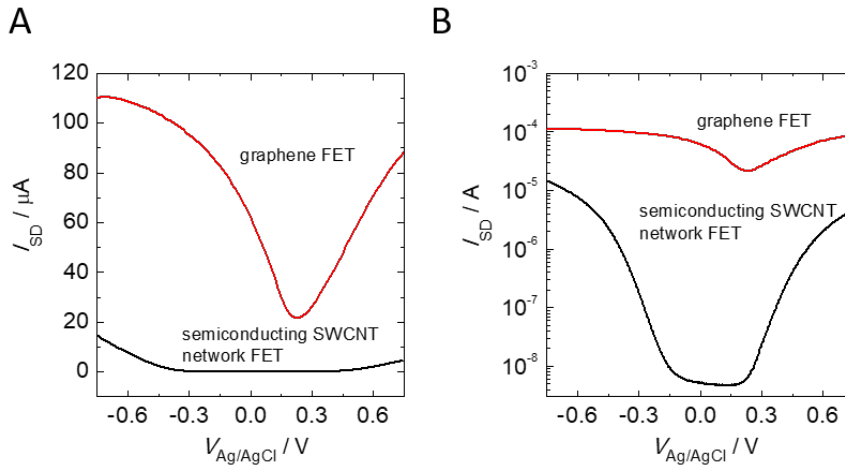


**Figure 1.21** – Comparison between transfer curves of FET devices based on two different carbon nanomaterials: graphene and semiconducting single-walled carbon nanotubes. In both cases, the source-drain voltage  $V_{SD} = 100 \text{ mV}$ . **A** Transfer curves presented with current in linear scale. **B** Transfer curves presented with current in logarithmic scale.

## 2 | Carbon nanotube field-effect transistors with nanobody receptors for immunodetection in physiological solutions

The study described in this chapter was previously published as "*Highly sensitive, selective and label-free protein detection in physiological solutions using carbon nanotube transistors with nanobody receptors*" in *Sensors and Actuators B: Chemical*<sup>117</sup> with Marcin S. Filipiak as first author.

### 2.1 Introduction

Field-effect transistor (FET) based transducers were proven to be highly sensitive and found applications in environmental monitoring, screening or even diagnostics. As for the choice for FET channels, a wide variety of nanomaterials were explored including semiconducting nanowires,<sup>118–120</sup> carbon nanotubes,<sup>121–124</sup> graphene,<sup>6,125–127</sup> organic semiconductors<sup>128,129</sup> and other layered two-dimensional materials.<sup>130,131</sup> Carbon nanotubes seem to be particularly interesting due to excellent electronic and mechanical properties as well as the option of solution-based processing, which can be implemented in low-cost printed electronics<sup>132</sup> and sensors.

While being extremely promising due to their high sensitivity, single walled carbon nanotube FETs have faced significant fabrication challenges, in part because the selective production of semiconducting CNTs is very difficult and the presence of metallic CNTs can compromise the transistor performance and device reproducibility. Fortunately, the progress in sorting the CNTs has overcome this challenge resulting in high purity semiconducting nanotubes with remarkable current on/off ratios and reproducible device characteristics.<sup>116,122,124,133–137</sup> Although there has been examples of carbon nanotube field-effect transistor based biosensor made from single carbon nanotubes,<sup>58,123,138,139</sup> to date, surprisingly biosensors made from semiconducting CNT networks is a rather underexplored field given the potential.<sup>108</sup>

FET-based (bio)sensors working principle is based on adsorption of charged species on the sensors surface, in case of electrolyte-gated FETs - the semiconducting channel surface. The charges added through this binding event cause a surface potential change and thus a current change in the transistor channel *via* the field effect. However, two main issues have so far limited their use beyond proof-of-principle studies: 1) Debye

screening, in which the analyte charge is screened by electrolyte ions and 2) significant non-specific adsorption of other species present in complex matrices (e.g. serum, blood). In physiological conditions, where the ionic strength oscillates between 100 and 200 mM, the effective distance for charge detection is  $<1$  nm.

Several solutions have been proposed in order to sense beyond the Debye screening length: **1**) dilution of the fluid sample,<sup>140</sup> **2**) enrichment followed by elution into low ionic strength buffer,<sup>141</sup> **3**) addition of a signal-enhancing label ("electronic ELISA"),<sup>142</sup> **4**) use of polyelectrolyte multilayer films,<sup>143</sup> **5**) high frequency AC measurements,<sup>55</sup> **6**) the use of shorter receptors<sup>6,7,14,15,52-54,59,144,145</sup> and finally **7**) co-immobilization of receptor within a polyethylene glycol layer (PEG).<sup>6,7,59</sup> While highly effective in avoiding the Debye screening, the mentioned approaches require pre-treatment of physiological samples (**1**), additional reagents (**3**), washing buffers (**2**), elaborate labelling (**3**) and more complex liquid handling (**1**, **2** and **3**), which results in higher assay cost and longer measurement times. Polyelectrolyte multilayer films (**4**) seem like an interesting solution, but the preparation times of such films are very long and cumbersome. The high frequency AC measurements (**5**) require special instrumentation, which limits the use in Point-of-Care environment.

The approach of using smaller receptors (**6**) seem to be the prevailing trend. The typical antibody receptor size is on the order of 10-15 nm ( $M_w \sim 140$  kDa), which makes the direct detection of antigens (e.g. proteins) very difficult. The receptor size is crucial for the FET-based biosensors in two ways: a) smaller receptors bring the antigen-receptor interaction closer to the surface and b) the density of the smaller receptors on the surface can be higher, increasing the amount of binding events in the first place. To overcome the Debye screening, smaller alternative receptors were proposed including aptamers<sup>6,52,144</sup> ( $\sim 5$ -15 kDa,  $\sim 2$ -3 nm), F(ab')<sub>2</sub> fragments<sup>7,59</sup> ( $\sim 110$  kDa,  $\sim 7$ -8 nm), single Fab fragments ( $\sim 50$  kDa,  $\sim 7$ -8 nm)<sup>14,15</sup> or single-chain variable fragments (scFv,  $\sim 27$  kDa).<sup>145</sup> Camelid heavy-chain VHH antibody fragments (also called "nanobodies") are one of the shortest available biological receptors ( $\sim 13$  kDa,  $<3$  nm) and the easy production and stability in a range of different conditions,<sup>16</sup> make them even more suitable receptor for FET-based biosensors. Yet, their usefulness as recognition elements of a biosensor was proven only in photoelectrochemical<sup>17,18</sup> and electrochemical<sup>19,20</sup> formats, not in combination with transistor-based sensors.

On the other hand, using short receptors alone may not be sufficient to achieve sufficient signals, as a large part of the analyte may be still screened by the electrolyte ions due to very short Debye length in high ionic strength solutions ( $<1$  nm). Therefore, the use of poly(ethylene glycol) (PEG) layer co-immobilized with the receptors (**7**) is a promising strategy for overcoming the Debye screening limitation and was proven to work even in undiluted serum.<sup>7,59</sup>

In this work, the combination of using green fluorescent protein (GFP - model antigen) specific nanobody receptors (**6**) along with poly(ethylene glycol) (**7**) were used to overcome the Debye length problem. First, a systematic study of the "PEG effect" is carried out by comparing two different nanobody-coated surfaces, with and without the addition of PEG. The surface modification is carried out directly on the semiconducting SWCNT network FET channels. Strikingly, even without PEG, significant signals are measured which is attributed to the small size and random orientation of nanobodies on the surface. Additionally, the signal is strongly enhanced in the presence of PEG even in

high ionic strength buffer. With the PEGylated devices, highly sensitive, selective and label-free immunosensing with a low detection limit ( $<1$  pM) is demonstrated. Finally, the sensor stability is assessed, where signal *vs.* time is measured and compared with other biosensing platforms, showing extraordinary stability of semiconducting CNTs *vs.* conventional semiconductors.

## 2.2 Results

### 2.2.1 Characterization of the electrolyte-gated CNT FET

The single-wall carbon nanotube network FETs were operated in an electrolyte-gated configuration (see Subsection 1.2.2), as shown in Fig. 2.1 A. The semiconducting SWCNTs were enriched using conjugated polymer sorting method and aligned in an AC electric field following a previously published protocol.<sup>115,146</sup> More details are given in Section 6.1. Electrical characterization i.e. transfer curves are presented in Figure 2.1 B. All measured transistors ( $n = 15$ ) showed ambipolar behavior (both hole and electron transport) with small hysteresis, current on-off ratios exceeding  $10^3$  at low gate voltages, and steep subthreshold swings  $>110$  mV/dec which can be explained by highly efficient electrolyte gating through the double-layer capacitance. An atomic force micrograph of a typical SWCNT network is shown in Figure 2.1 C. The two horizontal stripes at the top and the bottom of the image are the edges of the gold electrodes with a dual function: firstly used to align the carbon nanotubes in an electric field applied between the electrodes, and next, used as the source and drain electrodes of the FET. Between the electrodes, carbon nanotube network is seen orientated perpendicular to the gold electrodes. The geometric channel dimensions are defined by the interdigitated gold contacts, with the nominal channel length  $L_{geom} = 20$   $\mu\text{m}$  and the channel width  $W_{geom} = 2$  mm. Single nanotubes do not bridge the whole channel, since their length varies between  $0.3 - 4$   $\mu\text{m}$ , but the network allows charge percolation pathways between source and drain.<sup>147</sup> The average CNT density over the width of the channel is estimated to be around  $5-6$   $\mu\text{m}^{-1}$  and taking into account the diameter of a single nanotube ( $0.9-1.9$  nm), the effective channel width is in the range of  $W_{eff}$  10 - 20  $\mu\text{m}$ , which is only  $\sim 0.5-1\%$  of the geometric channel width ( $W_{geom} = 2000$   $\mu\text{m}$ ).

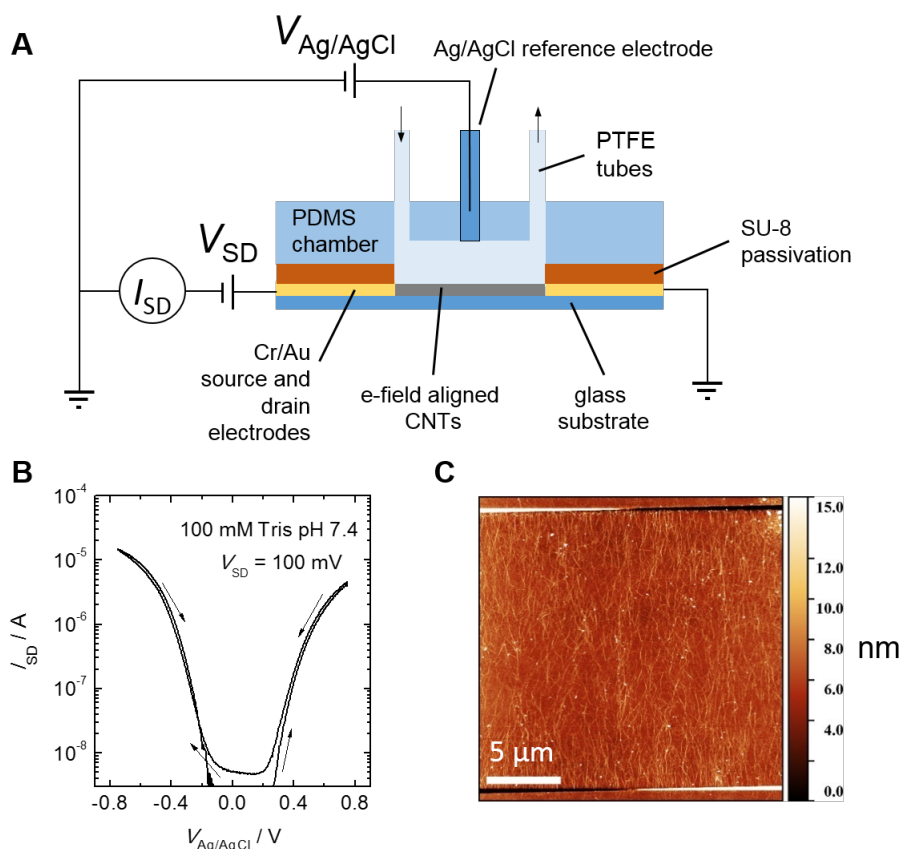


**Figure 2.1** – **A** Schematic illustration of the measurement setup. The semiconducting SWCNT network is aligned between interdigitated Au electrodes. Additionally, the contacts are passivated with SU-8 photoresist to avoid leakage current. To provide different liquids to the sensing surface, a microfluidic PDMS chamber with PTFE tubing is used. The Ag/AgCl reference electrode is placed in the middle of the microfluidic channel. **B** Typical transfer curves in both voltage sweep directions. The hysteresis is very small. **C** AFM image of the electric field aligned SWCNT network. Horizontal stripes at the top and bottom are the edges of the gold electrodes used to align SWCNTs. The same electrodes were later used as source and drain contacts for electrical measurements. The network shows a preferred overall orientation perpendicular to the contact lines. The estimated SWCNT density is  $5\text{-}6\ \mu\text{m}^{-1}$ . From this density, the effective channel width can be estimated to be  $10\text{-}20\ \mu\text{m}$ . The channel length is  $20\ \mu\text{m}$ . Reprinted from.<sup>117</sup> Copyrights 2017 Elsevier.

### 2.2.2 Surface functionalization of CNT FET

To construct a biosensor, CNT FET were functionalized using non-covalent pyrene chemistry (based on  $\pi$ - $\pi$  stacking, see Paragraph 1.1.3) to preserve the devices' remarkable electronic properties. 1-pyrenebutyric acid (PBA) (for chemical structure see Fig. 1.5 B) was used as a bifunctional linker molecule between the CNTs (binding *via* pyrene moiety) and nanobodies (binding *via* -COOH functional group, used to aminocouple  $-\text{NH}_2$  from nanobody surface lysines *via* EDC/NHS chemistry, see Paragraph 1.1.3). To enhance the biosensor signal in high-ionic strength, PEGylated pyrene derivative (mPEG pyrene, 10 kDa) was co-immobilized. A simple scheme of surface modification with the linker molecule PBA and the mPEG-pyrene can be seen in Fig. 2.2 A.

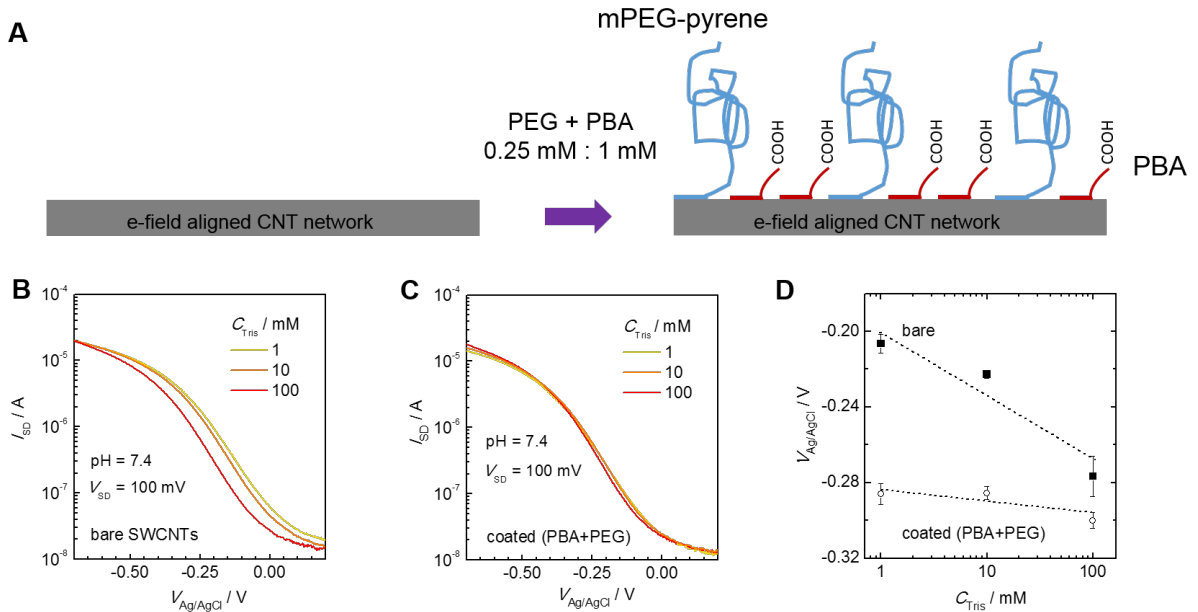


**Figure 2.2** – Measurements of bare (*i.e.* after THF cleaning) and coated SWCNTs in different ionic strength solutions, prior to receptor immobilization. **A** The surface functionalization was based on non-covalent  $\pi$ - $\pi$  stacking of 2 pyrene derivatives on SWCNTs: pyrenebutyric acid (PBA) as a linker for the receptor molecules, and mPEG-pyrene (10 kDa) for signal enhancement.<sup>5</sup> Transfer curves of bare (**B**) and coated SWCNTs (**C**) in 3 different Tris buffer concentrations ( $C_{Tris}$ ). The curves of bare SWCNTs shift to more negative potentials with increasing  $C_{Tris}$ , whereas nearly no shift is visible for the modified SWCNTs. The voltage  $V_{Ag/AgCl}$  at  $1 \mu A$  is shown (**D**) for bare and coated SWCNTs from **B** and **C**. Reprinted from.<sup>117</sup> Copyrights 2017 Elsevier.

Before attaching the receptor molecules, the bare and PBA+PEG modified SWCNTs were characterized in different ionic strength solutions (Fig. 2.2 B-C). As shown in Fig. 2.2 B, the transfer curves of bare SWCNTs shifted to more negative values when exposed to increasing ionic strength. The voltage at  $I_{SD} = 1 \mu A$  shifts by approximately -35 mV/dec (Fig. 2.2 D), which can be attributed to the non-specific interaction of alkali ions with conjugated  $\pi$  systems and defect sites.<sup>148</sup> In the case of PBA coated CNT FET, similar ion dependence was observed (32 mV/dec, not shown), whereas the whole transfer curves were shifted by  $\sim 20$  mV towards more negative values, ionic strength independent. This can be explained by charge transfer doping of SWCNTs by the COOH groups.<sup>149</sup> The ionic strength dependence is strongly suppressed, when a PBA+mPEG-pyrenes are attached to the surface of carbon nanotubes (Fig. 2.2 D), (the shift is  $< -5$  mV/dec). This observation suggests that co-immobilized poly(ethylene glycol) layer effectively reduces ion adsorption on SWCNT surface.

### 2.2.3 Electrical characterization of VHH immobilization on CNT FET

After the surface functionalization, GFP-specific VHH was attached to the PBA (or PBA+PEG) modified carbon nanotubes *via* the EDC/NHS aminocoupling (Fig. 2.3). The VHH immobilization resulted in a significant voltage shift to more negative poten-

tials of the transfer curve for both PBA only (Fig. 2.3 A) and PBA+PEG (Fig. 2.3 C) coated SWCNTs, which is expected due to the positive charge of VHH at pH 7 (theoretical isoelectric point = 7.18). A larger shift was obtained for the PBA+PEG surface ( $\sim 50$  mV, Fig. 2.3 D) rather than for PBA only ( $\sim 25$  mV, Fig. 2.3 B), which may be due to lowered dielectric constant of the surface in the presence of PEG.<sup>5</sup> The complete immobilization protocol is further described Section 6.1.

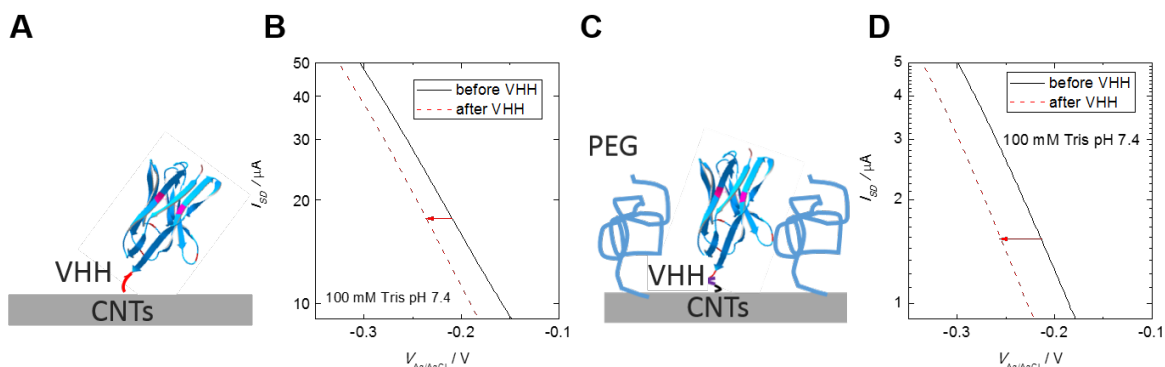


**Figure 2.3** – Immobilization of VHH on PBA only (A, B) and PBA+PEG (C, D) coated SWCNTs. Typical transfer curves in 100 mM Tris buffer for the surfaces prior to VHH immobilization (black lines) and after VHH immobilization (red lines) shown for PBA functionalized (B) and PBA+PEG functionalized (D) surfaces. Due to binding of VHH, the transfer curves shift to more negative potentials because VHH is positively charged at pH 7.4. The shifts are larger for PBA+PEG ( $\sim 50$  mV) than for PBA only ( $\sim 25$  mV). Reprinted from.<sup>117</sup> Copyrights 2017 Elsevier.

### 2.2.4 QCM reference measurements: GFP specific VHH immobilization and GFP binding

The immobilization of VHH as well as binding of GFP was also confirmed by independent quartz crystal microbalance (QCM, see Section 1.2.3) measurements (Fig. 2.4). Gold QCM chips were functionalized first with 6-mercaptophexanoic acid to assemble a monolayer with functional -COOH groups. After that, VHH was aminocoupled to the functionalized QCM chips via EDC/NHS chemistry. The surface modification steps details are provided in Chapter 6.

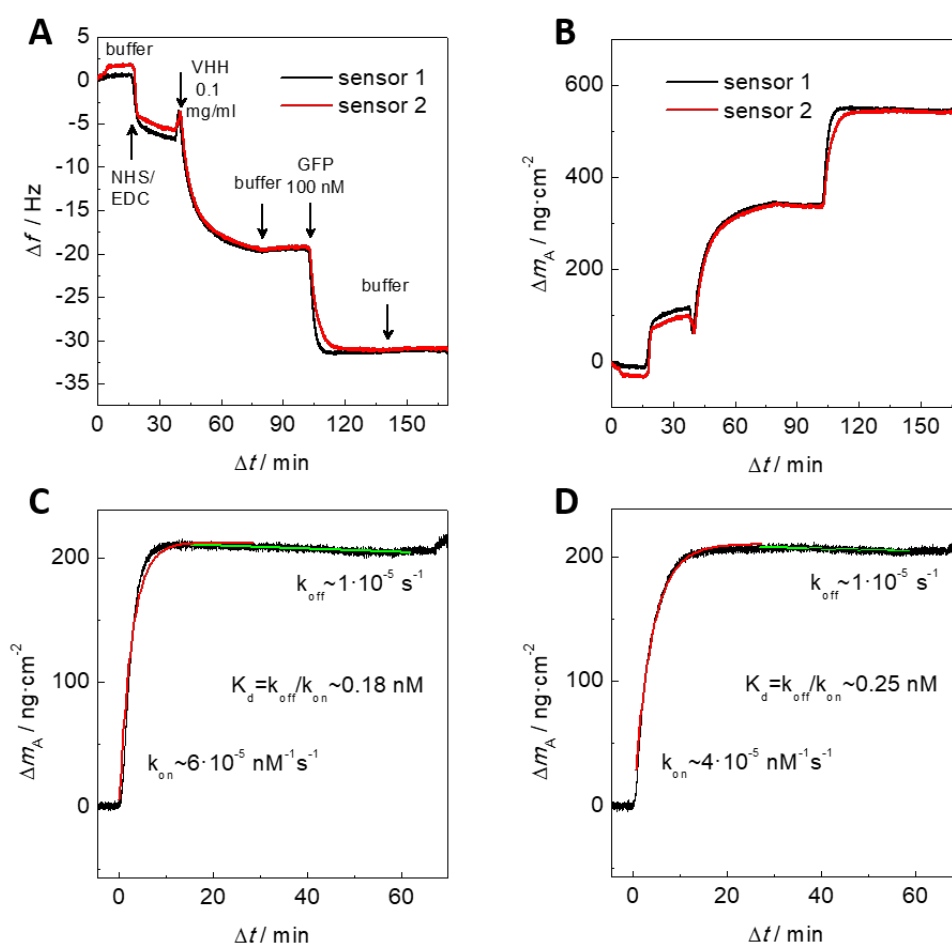


**Figure 2.4** – **A** Quartz crystal microbalance (QCM) results showing oscillation frequency changes  $\Delta f$  as a function of time  $\Delta t$  for 2 different sensor chips. The arrows indicate the exchange of different solutions as described in the text. The frequency decreases upon addition of VHH and GFP, indicating successful binding that cannot be easily removed by washing in buffer. **B** The frequency change was converted to the areal mass change  $\Delta m_A$  using the Sauerbrey equation (Equation S1). **C, D** The binding curves for 100 nM TSH obtained with sensor chip 1 (C) and sensor chip 2 (D) were fitted using Equation S2 (association; red lines) and Equation S3 (dissociation; green lines). The dissociation constants  $K_d$  estimated for both chips agree well with each other and were used for comparison (Tab. 2.2). Reprinted from.<sup>117</sup> Copyrights 2017 Elsevier. These measurements were performed by Arne Knudsen.

The areal mass change  $\Delta m_A$  can be estimated from measured frequency changes  $\Delta f$  using the Sauerbrey equation<sup>77</sup> (Equation 1.23; Fig. 2.4 B). To estimate the dissociation constant  $K_D=k_{off}/k_{on}$ , where  $k_{off}$  is the dissociation rate and  $k_{on}$  is the association rate, the GFP binding data were fitted using the following equations:<sup>127</sup>

$$\Delta m_A = \Delta m_{A,eq} \times (1 - e^{-(k_{on}C+k_{off}t)}) \quad (2.1)$$

$$\Delta m_A = \Delta m_{A,eq} \times (e^{-k_{off}t}) \quad (2.2)$$

where  $\Delta m_A$  is the sensor response *vs.* time  $t$ ,  $\Delta m_{A,eq}$  is the equilibrium response,  $C$  is the GFP concentration (100 nM). The fits for 2 different chips are shown in Fig. 2.4 C, D and yield similar  $K_D$  values. The resulting values agree well with previous reports and with the results of FET study (Tab. 2.2).

### 2.2.5 Effect of PEGylation on GFP binding to the VHH modified CNT FET surface

To investigate the effect of PEG on the GFP specific binding signal, VHH was again immobilized on both the PBA+PEG modified surface (Fig. 2.5 A) and on the control SWCNT samples modified with PBA only (Fig. 2.5 D). Both biosensor surfaces were then introduced to different GFP concentrations in 1 mM and 100 mM Tris buffer. The transfer curves are shown in Fig. 2.5 **B** for PEGylated surface and **F** for the non-PEGylated case. The readouts of transfer curves 2.5 **B** and **E** at currents indicated by a dashed line are shown in Fig. 2.5 **C** and **F**, respectively. In both cases, the transfer curves shift to more positive values with increasing GFP concentrations, wherein the PEGylated surface exhibits higher shifts. Importantly, the signal of the PEGylated sensor exhibits a 3-fold enhancement in 100 mM buffer compared to the non-PEGylated surface (25 mV *vs.* 8 mV for 100 nM GFP) as predicted by Haustein et al. analytical model of the PEG effect.<sup>150</sup> Signal (voltage shift) enhancement in low ionic strength (1 mM) is lesser and amounts to an approximately 2-fold increase (47 mV *vs.* 25 mV for 100 nM GFP). Strong positive impact on the maximum achievable sensor response by using PEGylated surface is indicated, which is in agreement with previous reports.<sup>5-7</sup>

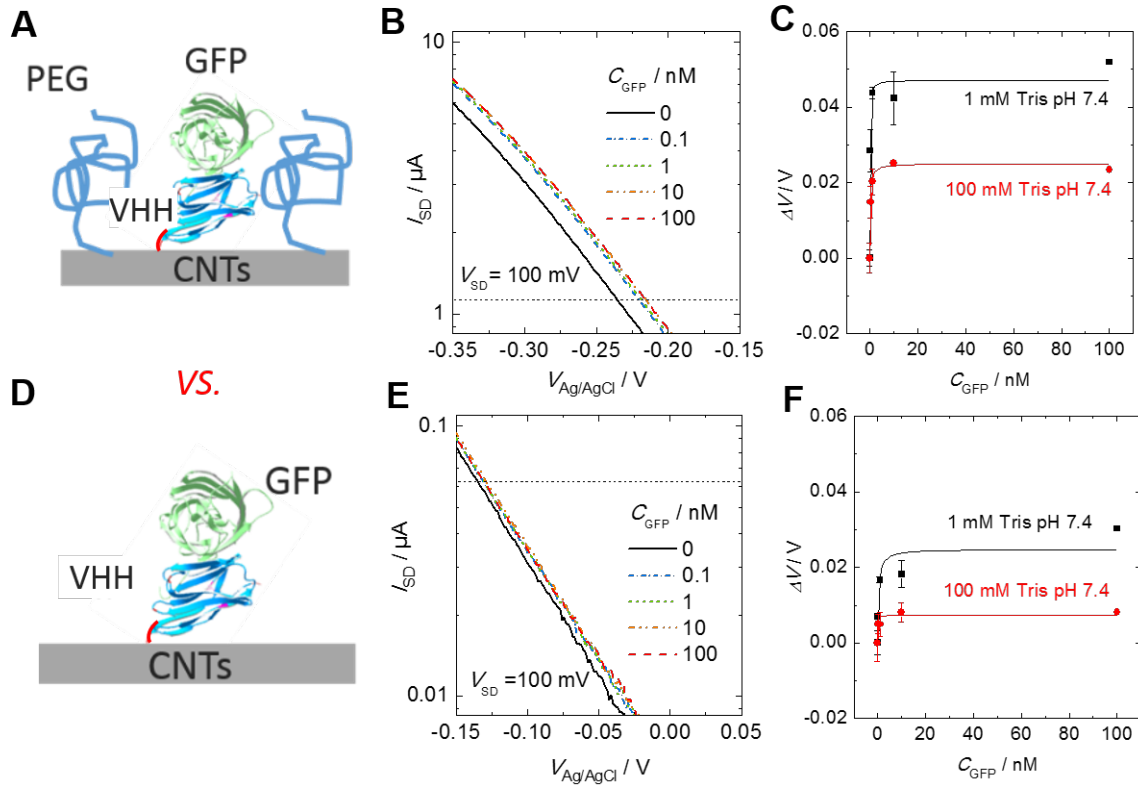


**Figure 2.5** – Comparison of GFP detection with PEGylated (**A-C**) and non-PEGylated SWCNT FETs (**D-F**). The surface of the SWCNTs was modified either with a mixture of pyrene butyric acid (PBA) with methyl PEGylated pyrene (**A**) or with PBA only (**D**). Camelid nanobodies (VHH), specific to green fluorescent protein (GFP), were then immobilized on both surfaces and exposed to GFP solutions to assess the VHH-GFP binding. **B** and **E** show the transfer curves measured in different concentrations of GFP in 100 mM Tris buffer. A shift to more positive potentials is visible in both cases with a stronger response in the PEGylated case (**B**). **C** and **F** summarize the potential shift  $\Delta V$  obtained as a function of GFP concentration  $C_{GFP}$  in 1 mM (squares) and 100 mM (circles) ionic strength solutions.  $\Delta V$  was read out at a constant  $I_{SD}$  value, as indicated by horizontal lines in **B** and **E**. The signal (voltage shift) in **C** is up to  $3 \times$  larger than that in **F**. Reprinted from.<sup>117</sup> Copyrights 2017 Elsevier.

### 2.2.6 Control experiments with "off-receptor" and "off-target"

To control for specificity of biosensor's response, additional experiments (Fig. 2.6) were conducted. As a control for the receptor specificity, the VHH was exchanged for bovine serum albumin (BSA, "off-receptor", Fig. 2.6 **A**), unspecific for GFP maintaining the same immobilization protocol, and measured in the same set of GFP concentrations in 100 mM buffer as the nanobody immobilized biosensors presented before. The transfer curves are plotted in Fig. 2.6 **B** and the response *vs.* GFP concentration is shown in Fig. 2.6 **C**. A small voltage shift of up to 5 mV due to unspecific GFP binding to the biosensor's surface is observed, which corresponds to approximately 20 % of the overall signal obtained with VHH (Fig. 2.6 **C**). In the second experiment, we focused on receptor specificity, where the VHH-modified biosensor was exposed to an "off-target" protein,

tobacco etch virus protease (TEV, Fig. 2.6 D-F). TEV protease was chosen due to similar molecular weight to GFP ( $M_{TEV} = 29$  kDa,  $M_{GFP} = 27$  kDa). In fact, similarly low levels of non-specific adsorption were observed for TEV (around 5 mV). However, the response trend was opposite to that of GFP (Figure 2.6 F). This is due to a difference in charge of the two proteins. In the measurement buffer pH = 7.4, TEV is positively charged (isoelectric point, IEP = 8.5 – 9.6), whereas GFP is negatively charged (IEP = 5.3 – 5.9). The transfer curves shift up to 8 mV to more negative potentials, which in combination with the previous non-specific adsorption experiment allows the claim that the VHH is indeed specific to GFP and the residual voltage shift is due to unspecific binding of TEV to the surface itself. Based on these experiments, we conclude that most of the signal presented in Fig. 2.5 C is due to specific interaction between VHH and GFP. However, up to 20 % of the signal can be a result of non-specific interactions of the sensor surface with proteins in solution (Fig. 2.6) and is a subject for further surface passivation.

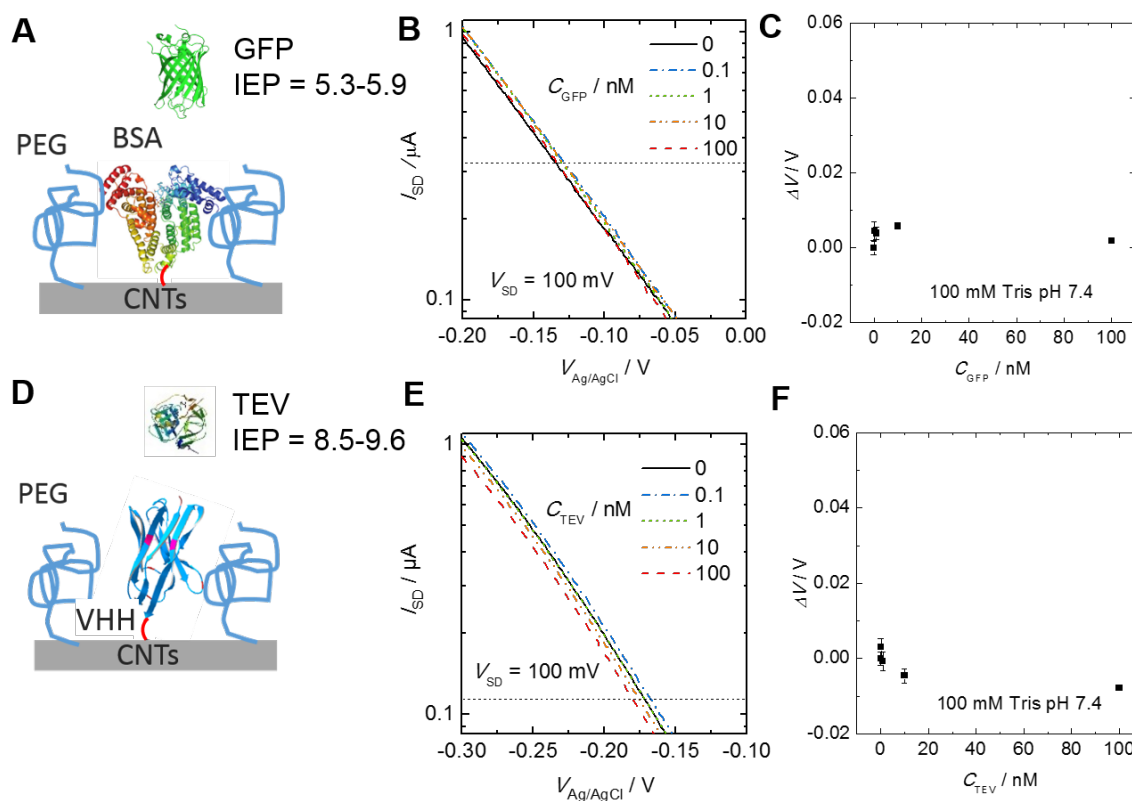


**Figure 2.6** – Non-specific adsorption experiments in 100 mM buffer with pH 7.4. **A-C** Non-specific binding of target protein (GFP) to BSA-coated SWCNTs. **B** The transfer curves only slightly shift to more positive voltages with increasing GFP concentration in 100 mM Tris buffer. **C** The non-specific sensor response is much smaller than the specific binding shown in Figure 2.3 C. The potential shift is positive because GFP is negatively charged at pH = 7.4 ( $IEP_{GFP} = 5.3-5.9$ ). **D-F** The selectivity of the VHH-coated sensor was tested using TEV protease, a protein similar in size and molecular weight to GFP but with the opposite net charge at pH = 7.4. **E** The curves shift only slightly to more negative voltages, indicating good selectivity of the sensor. **F** The sensor response has the opposite sign compared to GFP, because the isoelectric point of TEV is above the pH of the measurement buffer ( $IEP_{TEV} = 8.5-9.6$ ). Reprinted from.<sup>117</sup> Copyrights 2017 Elsevier.

### 2.2.7 Optimized SWCNT FET-based assay for GFP detection

The reduction of non-specific adsorption of the sensor was performed with 10  $\mu\text{M}$  BSA solution (Fig. 2.7 A). After the surface passivation, the transfer curve was measured again in blank Tris buffer (Fig. 2.7 B). To ensure surface passivation, the biosensor was exposed to two control proteins with different isoelectric points: 100 nM BSA (IEP  $\sim 4.8$ ,<sup>151</sup> close to the IEP of GFP  $\sim 5.3$ -5.8) and 100 nM TEV ( $\sim 8.5$ -9.6). As seen in Fig. 2.7 C, the voltage shift for non-specific adsorption of these 2 proteins (positively charged TEV and negatively charged BSA) is nearly zero. Using this passivated biosensor, the specific detection of even lower GFP concentrations ranging from 1 pM to 1  $\mu\text{M}$  was performed. The maximum response is lower than shown in initial experiments without BSA blocking (Fig. 2.5 C). The reduction of the signal comes from a significant decrease of non-specific protein adsorption. Even for the lowest GFP concentration of 1 pM, the voltage shift is well above the level of non-specific adsorption of 100 nM BSA and 100 nM TEV. The biosensor reaches its maximum response ("saturates") at  $\sim 100$  nM (Figure 2.7 C). The dynamic range of the biosensor spans from 1 pM to 100 nM (5 orders of magnitude) with a possibility of further extension into the sub-pM regime. For comparison, a commercial ELISA sandwich assay for GFP quantification<sup>152</sup> has a measuring range of 3 orders of magnitude ( $\sim 0.1$  pM -  $\sim 0.1$  nM), is time-consuming (few hours) and requires multiple washing steps. The additional blocking by BSA strongly suppresses the non-specific adsorption below the detection limit, which is a significant improvement compared to previously reported relatively high levels of non-specific adsorption (up to 30%<sup>6</sup>).

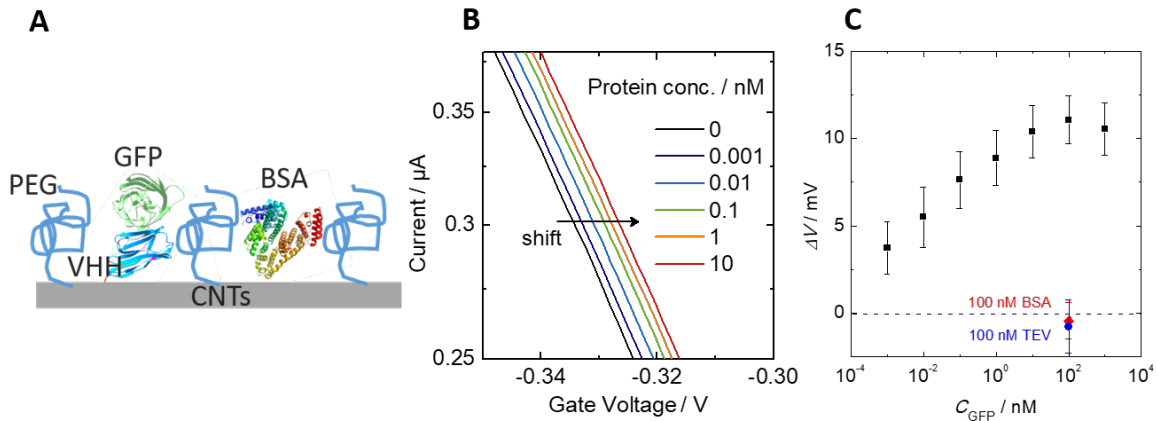


**Figure 2.7** – *Optimized SWCNT FET-based assay for GFP detection.* **A** The PEGylated sensor was additionally passivated with BSA to further reduce the non-specific adsorption. **B** The transfer curves were measured in 100 mM buffer over a large range of GFP concentrations. A shift of the transfer curve to more positive voltages is visible with increasing GFP concentration (indicated by the arrow). **C** The sensor response  $\Delta V$  vs. the concentration of GFP on a log scale (squares). The dashed line represents the blank value ( $C_{\text{GFP}} = 0$ ). The non-specific response to 100 nM TEV (circle) and BSA (diamond) is negligible. Reprinted from.<sup>117</sup> Copyrights 2017 Elsevier.

### 2.2.8 CNT FET long-term stability

Next, the carbon nanotube field-effect transistors long-term stability is assessed. After initial 0.5 h equilibration, the I-V curves (Fig. 2.8 A) scanned during the time frame of 96 hours do not exhibit significant shifts – a small drift of about -0.05 mV/h can be observed (Fig. 2.8 B). This result confirms that the signal shifts in all experiments arise from the binding events of different species to the surface of the nanotubes and are not a result of signal drift in time.

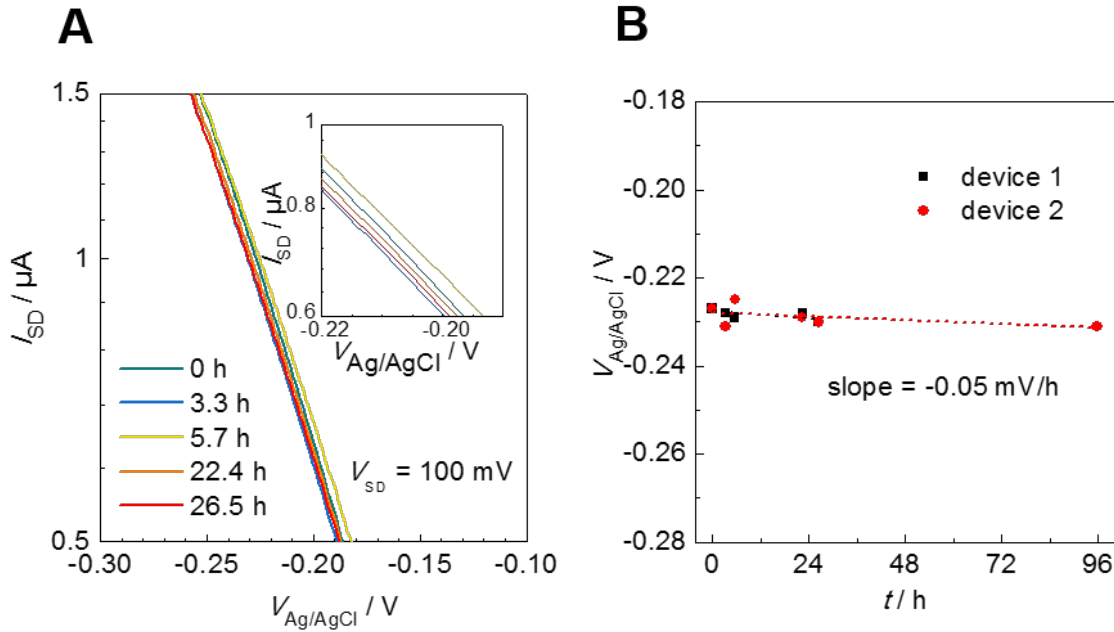


**Figure 2.8** – Long-term stability measurements. **A** Transfer curves in buffer after different waiting times with an enlarged view in the inset. **B** The voltage at 1  $\mu A$  is shown for 2 different devices. Almost linear drift is observed with the slope of -0.05 mV/h. This value is lower (better) than for conventional Si devices, as shown in Tab. 2.1. Reprinted from.<sup>117</sup> Copyrights 2017 Elsevier.

**Table 2.1** – Long-term stability measurements comparison with silicon nanowires technology. Reprinted from.<sup>117</sup> Copyrights 2017 Elsevier.

	this work	fin FET <sup>153</sup>	HfO <sub>2</sub> dielectric <sup>154</sup>	Al <sub>2</sub> O <sub>3</sub> dielectric <sup>155</sup>
$\delta V/\delta t$ / mV/h	0.05	0.1	1.88	0.3

Furthermore, an estimation of the dissociation constants ( $K_D$ ) of the GFP specific VHH using Langmuir adsorption isotherm following the equation (Equation 2.3) is performed:

$$\Delta V = \frac{\Delta V_{max} \times C}{K_D + C} \quad (2.3)$$

where  $\Delta V$  is the voltage shift in subthreshold region of the transfer curve,  $\Delta V_{max}$  is the maximum voltage shift,  $K_D$  is the dissociation constant and  $C$  is the concentration of the analyte (GFP).

**Table 2.2** – Comparison of dissociation constant values for VHH-GFP binding, obtained with different sensor systems. The estimated  $K_D$  values are consistent with previous reports and our QCM data (see Fig. 2.4). Reprinted from.<sup>117</sup> Copyrights 2017 Elsevier.

Transducer	Sensor surface	PEGylated	$K_D$	Ref.
FET	SWCNT	yes + BSA blocking	$0.08 \pm 0.06$	this work
FET	SWCNT	yes	$0.08 \pm 0.03$	this work
FET	SWCNT	no	$0.16 \pm 0.02$	this work
QCM	gold	no	$0.21 \pm 0.11$	this work
QCM	gold	no	$0.59 \pm 0.11$	<sup>156</sup>
SPR	gold	no	0.32	<sup>157</sup>
SPR	gold	no	0.23	<sup>158</sup>

The estimated  $K_D$  values for different surface modifications studied here are shown in Tab. 2.2 and are in agreement with previous reports<sup>156–158</sup> and the obtained QCM data (Fig. 2.4). This further confirms the selective binding of GFP to the immobilized nanobody receptors.

## 2.3 Discussion

In this work, I present a GFP-specific FET-based biosensor that employs high quality sorted semiconducting SWCNT networks as the transducer and nanobodies as the receptors. The polymer sorting process enables fabrication of highly uniform, homogeneous and reproducible CNT FETs with high on/off ratios over 1000<sup>115,116,122</sup> (see Fig. 2.1 B). The approach used in this work is scalable and can be easily translated into printing techniques, as shown recently by Rother et al.<sup>159</sup> The CNT FETs are also proven to be highly stable (the transfer curves shift only by 0.05 mV/h during long-term experiment, see Fig. 2.8), which in comparison to the conventional silicon based devices is far more stable (less drift observed, see Tab. 2.1).

As for receptors, it is the first time very short and stable nanobodies (VHH) are employed in an FET setting. According to Ries et al.,<sup>160</sup> the size of VHH specific to GFP is merely  $\sim 2 \times 4$  nm, whereas the epitope (binding site) is located on the longer edge of the nanobody.<sup>14</sup> The linker (pyrenebutyric acid, PBA) size can be estimated as a sum of different bonds to be  $\sim 0.7$  nm ( $\pi$ - $\pi$  stacking itself  $\sim 350$  pm,<sup>161</sup>  $4 \times$  C-C bonds  $\sim 150$  pm and  $1 \times$  C-O bond  $\sim 180$  pm<sup>162</sup>). Recently it has been shown by Hinnemo et al.<sup>37</sup> that the average thickness of a saturated self-assembled monolayer formed by using PBA solution is 0.7 nm. Given that the large pyrene anchoring sites provide some spacing between the receptor molecules as well as a 4-carbon aliphatic chain may allow some flexibility, I can assume that the distance of linker and nanobody binding can be less than 0.7 nm. The random orientation of VHH on the surface may be the reason that there is a small signal

detected attributed to GFP adsorption even in high ionic strength buffer (100 mM), where the Debye length is approximately 1 nm (Fig. 2.5 **E, F**).

This work provides an evidence that poly(ethylene glycol) co-immobilized with receptor molecules on the surface of a FET biosensor enhances the overall specific signal of the given biosensor. Here, I used 10 kDa PEG, which is about 7<sup>6</sup> to 10 nm<sup>150</sup> long. Both in low ionic strength (1 mM) and high ionic strength (100 mM) (see Fig. 2.5 **A-C**), a substantial signal enhancement is recorded. In 100 mM buffer, a 3x signal increase is achieved compared to no-PEGylated sensor. In low ionic strength buffer (1 mM), only about 1.5 times signal enhancement is seen, most probably because the Debye length in 1 mM (10 nm) is long enough for the detectable charge to be almost 100%.<sup>150</sup> The additional signal enhancement in 1 mM buffer is most likely due to a PEG molecules that are stabilizing and properly spacing the immobilized biomolecules.<sup>163</sup>

The "PEG effect" i.e. signal enhancement in presence of PEG in high ionic strength buffers is robust and reproducible, the exact mechanism of this phenomenon is still not understood. The original papers by Gao et al.<sup>5,6</sup> mention that PEG is responsible for changing the dielectric properties of the interface. Haustein et al.<sup>150</sup> discuss different parameters (capacitance, receptor density, dissociation constant of the receptor, and analyte charge) that can influence the FET-based immunosensors by presence of a PEG layer and conclude that the analyte charge is the only changing parameter. The analytical model includes the assumption of the presence of Donnan potential, where the Debye screening starts to occur not at the sensor surface (metal, oxide, CNTs etc.), but rather at the surface layer (PEG)/electrolyte interface.

Compared to the original works on PEG-enabled specific detection of analyte by FET biosensor in high ionic strength buffer,<sup>6</sup> this work shows systematic concentration-dependent studies with a wide dynamic range of analyte (GFP) determination (4 orders of magnitude) with sub-picomolar lower limit of detection (LoD), and negligible non-specific adsorption. Gao et al.<sup>6</sup> presented the results only for relatively high PSA concentration  $\sim$ 100 nM with rather high non-specific adsorption signals of up to 30 % and low signal-to-noise ratio. Gutierrez et al.<sup>7</sup> presented the gold extended-gate FET assay for TSH determination using PEG for the same purpose - signal enhancement in high ionic strength buffer. The authors used F(ab')<sub>2</sub> fragments and were able to determine thyroid-stimulating hormone (TSH) concentration in horse serum (natively TSH free) from 0.5 to 10 000 pM, but observed only 17 mV maximum voltage shift for optimized assay conditions (37 °C). In the case of CNT FET, a maximum voltage shift of 25 mV with <1 pM limit of detection was observed in high ionic strength buffer in room temperature. Further studies at elevated temperatures may increase the overall signal as well as decrease the lower limit of detection of the assay.

In the past years, CNT FET based immunosensors have gained much attention (see Tab. 2.3) showing high sensitivity and remarkably low detection limits ( $\leq$ 100 fM).<sup>54,164-166</sup> Although, to best of my knowledge, those experiments were conducted in diluted buffer or serum<sup>54,121,164,166-169</sup> or even in the dry state.<sup>165,170,171</sup> The challenge to overcome Debye screening is valid for all the FET-based biosensors<sup>109</sup> and limits the applicability of such in e.g. Point-of-Care environment, where the time to result is crucial. This setting requires simplicity and robustness, therefore sample dilution, low ionic strength washing (or reading) buffers, or drying the sensor surface after the binding event, are not preferred. The receptor length influence on the Debye screening problem in CNT FETs has been

explored by Kim et al.<sup>54</sup> The authors studied whole antibodies ( $\sim 10\text{-}12$  nm),  $F(ab')_2$  ( $\sim 5$  nm) and Fab ( $\sim 3\text{-}5$  nm) fragments and have found that the smaller the receptor, the higher FET signal and lower the detection limit can be achieved. The presented study has been performed in rather low ionic strength buffer (10 mM), where the Debye length is expected to be  $\sim 3$  nm. In here, I present the direct detection of GFP in high ionic strength solutions (Debye length  $< 1$  nm) using CNT FET in combination with even shorter and more stable receptors - nanobodies.<sup>156</sup> Although PEG is proven to reduce the non-specific interactions,<sup>164,167,169</sup> in this work, its main purpose is to enhance the FET signal to enable immunosensing in physiological conditions<sup>5-7</sup> as discussed above.

**Table 2.3** – Comparison of different CNT FET biosensors that employed antibodies and fragments thereof as receptors. Reprinted from.<sup>117</sup> Copyrights 2017 Elsevier.  
(\* PEG used to reduce non-specific adsorption, § PEG used to enhance signal)

Receptor	Analyte	Dynamic range	Sample	Ref.
anti IL-6	IL-6	1.37 pg/ml-100 pg/ml (65 fM – 4.76 pM)	diluted serum (1:100) in buffer	164
anti ARG 1	human ARG-1	30-100 ng/ml (0.857 – 2.857 nM)	dry state	170
APQ4 loop peptide	AQP4 antibody	1 ng/l - 1µg/l (28.57 fM – 28.57 pM)	diluted serum (1:100 000) in buffer	166
p41 antibodies	B. burgdorferi antigen (p41)	1 ng/l - 1µg/l (27.4 fM – 27.4 pM)	dry state	165
whole antibody (10-12 nm)	human IgG	$\sim 1000$ ng/ml ( $\sim 6.67$ nM)	10 mM buffer	54
Fab'2 fragment (5-8 nm)	human IgG	10 ng/ml-1000 ng/ml (66.7 pM – 6.67 nM)	10 mM buffer	54
Fab fragment (3-5 nm)	human IgG	1 pg/ml-100 pg/ml (6.67 – 666.67 fM)	10 mM buffer	54
polymer+biotin	streptavidin	$\sim 2.5$ µM	10 mM buffer	169 *
streptavidin	IgG	$\sim 100$ nM	10 mM buffer	167 *
U1A protein	10E3 antibody	1 nM- $>30$ nM	10 mM buffer	167 *
hemagglutinin	anti-hemagglutinin	$5 \times 10^{-8}$ - $1 \times 10^{-5}$ mg/ml (0.79 pM – 158.73 pM)	dry state	171
anti-pig serum albumin	pig serum albumin	$\sim 2$ µM	10 mM buffer	168
anti-PSA antibody	prostate specific antigen	$< 100$ pM-100 nM	5 mM buffer	121
GFP specific nanobody	GFP	1 pM – 10 nM	100 mM buffer	this work §

## 2.4 Conclusions

In this work, field effect transistors based on high-purity semiconducting carbon nanotube network were investigated as transducer, and in combination with short and stable nanobodies as biological receptors, to produce a highly sensitive and stable biosensor. The Debye length limitation (charge screening by ions in high ionic strength solutions) was overcome by a mixed surface functionalization consisting of short receptors (nanobodies) with poly(ethylene glycol) as a signal enhancer. This is the first time nanobodies were applied in the FET-based biosensor setting. Immunosensing of GFP as a model antigen was performed with the biosensor showing sensitive, selective and label-free protein determination over a 4 orders of magnitude concentration range with a sub-picomolar detection limit in high ionic strength (100 mM) solutions. Even without PEG, detectable voltage shifts in high ionic strength solutions were recorded, only due to the presence of nanobodies, which suggests that the small size and random orientation of VHH receptors on the surface can enable analyte binding within the Debye length. The mechanism of PEG-induced signal enhancement may be explained within the Donnan potential theory,<sup>150</sup> where the Debye screening starts to occur at the surface layer/electrolyte interface. Further studies are needed to completely understand this effect. The estimated dissociation constants are not strongly affected by the presence of PEG and are in agreement with previous reports for the GFP-nanobody binding. The presented CNT FET showed long-term stability with very low drift of 0.05 mV/h, which is much lower than for conventional silicon-based devices. The GFP determination range shown here is much wider and significantly faster (<20 min vs. few hours) than for a commercially available ELISA sandwich immunoassay. Finally, the presented direct nanoelectronic immunoassay is fast, label-free, does not require any washing or sample dilution steps, and has the potential to be used in Point-of-Care environment, where reliable results are needed within minutes.

# 3 | TSH immunosensing with single-sheet graphene field-effect transistor

The study described in this chapter was previously published as "*Graphene-Based Electronic Immunosensor with Femtomolar Detection Limit in Whole Serum*" in *Advanced Materials Technologies*<sup>59</sup> with Dr. Nesha M. Andoy as the first author and Marcin S. Filipiak as the second author.

## 3.1 Introduction

Graphene, a two-dimensional material with a single-atom thickness, is extremely sensitive in sensing molecules that interact with its surface,<sup>84,172</sup> which makes it an attractive transducer for (bio)sensing.<sup>173,174</sup> In the field-effect transistor based biosensing, graphene is widely used in so called "electrolyte-gated" configuration<sup>69,126,175–177</sup> (for more details see Section 1.2.2). Briefly, the receptor molecules (antibodies, aptamers etc.) are directly immobilized on the surface of graphene serving as the channel in a field-effect transistor, which is directly in contact with the liquid sample with the analyte. The gating occurs through a reference electrode (e.g. Ag/AgCl) and the electric double layer forming in electrolyte solution serves as the "dielectric" (in terms of classical MOSFET). Due to highly sensitive charge transport in graphene, any electronic disturbance that can arise from the binding event of a charged molecule to the surface of graphene, can lead to drastic changes in the charge carriers transport (both holes and electrons).<sup>69,176,178</sup> These changes can be caused by different mechanisms: **1**) electrostatic gating, **2**) charge transfer between the graphene and the analyte (acceptor or donor), **3**) charge scattering across graphene, **4**) Schottky barrier effect or **5**) capacitance modulation, often appearing as a result of different effects at the same time.<sup>58,69,179,180</sup>

An interesting approach has been proposed by Gao et al.,<sup>5</sup> where the authors co-immobilize the receptor molecule with poly(ethylene glycol) on the sensor's surface, enabling the protein immunosensing even in high-ionic strength solutions. Recently, Gutierrez et al.<sup>7</sup> have shown that this strategy could be applied to thyroid stimulating hormone (TSH) electronic immunoassay in whole serum, covering wide concentration range from 0.5 to 10 000 pM with  $\sim$ pM detection limit at 37 °C. The reference cutoff value for hyperthyroidism is  $<100$  fM<sup>181</sup> and thus a need for even lower detection limit of TSH with FET-based biosensor is still unrealized, not to mention e.g. cancer and cardiac biomarkers that require even lower limits of detection.<sup>182</sup> Therefore, a new generation of highly-sensitive

biosensing devices has to be developed to address the Point-of-Care application.<sup>183–185</sup>

Based on the concepts developed for CNT based biosensors, here, an electrolyte-gated graphene field-effect transistor (GFET) was used as a transducer element to develop a highly selective and sensitive TSH biosensor at room temperature with low-fM lower limit of detection (LoD) in high ionic strength buffer. To do so, a mixed surface functionalization has been employed: F(ab')<sub>2</sub> antibody fragments were co-immobilized with poly(ethylene glycol). Commonly, the voltage shift in charge neutrality point of GFET serves as the analytical signal and therefore, the analyte detection with GFET is said to be caused by electrostatic gating effect. In this chapter, the precise analysis of multiple parameters of the analyte binding induced changes in graphene's electronic response suggests that the mechanism of analyte detection may be the scattering by charged impurities.

## 3.2 Results and discussion

### 3.2.1 Device fabrication

The fabrication of the GFET is described in more detail in Chapter 6. Briefly, the GFETs were fabricated by the wet transfer of CVD grown Trivial Transfer Graphene pieces floating on the surface of water to patterned gold coated glass chips (Fig. 3.1 A and B). After the transfer, the graphene support layer - PMMA, was removed by acetone using a Soxhlet extractor. The gold electrodes were used as source and drain contacts, graphene as a channel of the FET and a bulk Ag/AgCl reference electrode (RE) as the gate terminal. A PDMS slab with microfluidic channel was placed on the top of the graphene coated glass chip to expose only graphene to the liquid in microfluidic channel. Inlet and outlet tubes, as well as RE, were inserted into the PDMS slab as shown in the Fig. 3.1 A. A representative Raman spectrum of the bare graphene on the glass substrate is presented in the Fig. 3.1 C. A signature 2D band peak at 2684 cm<sup>-1</sup> and G band at 1588 cm<sup>-1</sup>, the peak ratio (2D/G = 2.6) as well as the absence of defect peaks indicate that the graphene sample is of high-quality and single-layer.<sup>74</sup> The charge neutrality point (CNP),  $V_{g,min}$ , is shifted towards positive potential ( $V_{g,min} = 120 \pm 60$  mV ( $n = 20$ ) Fig. 3.1 D), suggesting p-doping by the glass substrate and surrounding air.

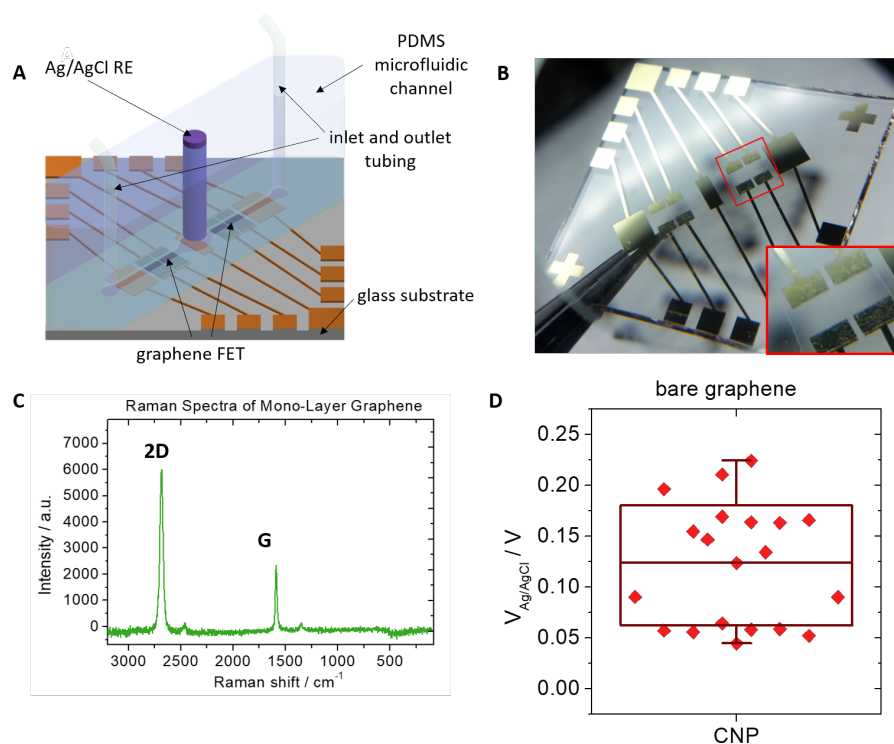


**Figure 3.1** – Graphene FET measurement setup. **A** Microfluidic graphene FET glass chip with single sheet graphene as FET channel, gold planar electrodes contacts and bulk Ag/AgCl as RE. **B** Photograph of as manufactured graphene FET device **C** Raman spectrum of single-sheet graphene showing characteristic peaks - 2D and G. **D** Reproducibility of charge neutrality point (CNP) of GFET in PBS buffer pH 7. Copyright 2018 by John Wiley & Sons, Inc.

### 3.2.2 Surface functionalization of graphene

A schematic illustration of surface functionalization is shown in the 3.2 A. First, the surface of graphene was functionalized using the mixed pyrene chemistry (i.e. 1-pyrenebutyric acid : *N*-(1-pyrenyl)maleimide - molar ratio 10:1) by means of  $\pi - \pi$  stacking (see Section 1.1.3). PyMal was introduced in order to bind the 10 kDa thiolated poly(ethylene glycol) (PEG) - SH-PEG-OCH<sub>3</sub> (see Section 1.1.3), while the PBA was used to introduce -COOH groups that were later on used to aminocouple the antibody fragments (F(ab')<sub>2</sub>) using the EDC/NHS chemistry (see Section 1.1.3). As described in Chapter 2, the presence of PEG decreases the Debye screening, making the immunosensing in high ionic strength solutions possible.<sup>6,7,60</sup>



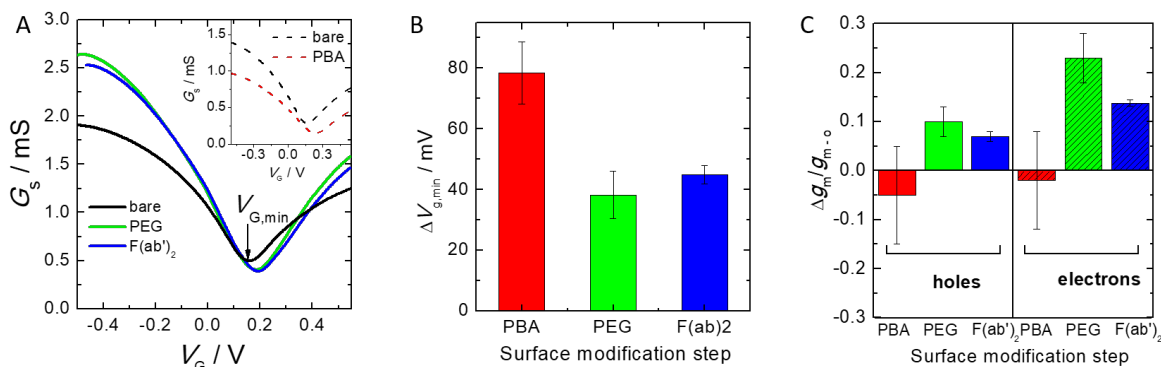


**Figure 3.3** – **B** Conductance  $G_s$  vs. gate voltage applied to the reference electrode  $V_G$  before and after surface functionalization (transfer curve). The gate potential at the minimum  $G_s$  ( $V_{g,min}$ ) for the bare graphene is indicated by the black arrow. Inset: Graphene's transfer curve before and after functionalization with pyrenebutyric acid (PBA). **C** Difference in  $V_{g,min}$  ( $\Delta V_{g,min}$ ) after various surface modification steps (relative to bare graphene). **D** Relative changes in transconductance ( $\Delta g_m/g_{m-o}$ ) of the hole and electron transport regions after the same surface modification steps. Adapted from.<sup>59</sup> Copyright 2018 by John Wiley & Sons, Inc.

\* pyrene = 10:1 1-pyrenebutyric acid (PBA):N-(1-pyrenyl)maleimide (PyMal).

After the PEG was immobilized, the -COOH groups from PBA coated graphene were activated using the EDC/NHS chemistry (see Section 1.1.3 in order to aminocouple the TSH specific F(ab')<sub>2</sub> antibody fragments (receptor molecules). F(ab')<sub>2</sub> immobilization shifts the  $V_{g,min}$  towards more positive potentials (p-doping) in comparison to PEG only modified graphene surface (Fig. ?? B & Fig. ?? C). Additionally, an asymmetric decrease in relative transconductance  $\Delta g_m/g_{m-o}$  can be also observed, with a more pronounced decrease for the electron part again (Fig. ?? D). Since TSH specific F(ab')<sub>2</sub> (IEP  $\sim$  7.5 - 8) is positively charged in PBS pH 7, when considering the electrostatic gating effect only, the  $V_{g,min}$  should shift to more negative potentials, while the transconductance should not change.<sup>58,69,180,188</sup> This points to the fact that the electrostatic gating mechanism is not responsible for the change in transfer curves and therefore other mechanisms should be taken into consideration (see Paragraph 3.1).

### 3.2.3 TSH detection in high ionic strength buffer

#### Specific TSH detection

The GFET-based F(ab')<sub>2</sub> modified biosensor was exposed to different TSH concentrations in high ionic strength buffer (100 mM NaCl + 5 mM phosphate buffer pH 8). A transfer curve shown in Fig. 3.4 A presents a representative graphene device measured in buffer containing different TSH concentrations ranging from 10 fM to 10 nM with evident changes around  $V_{g,min}$ . With increasing TSH concentrations, the transfer curve shifts to more negative potentials (n-doping of graphene). Taking  $\Delta V_{g,min}$  normalized to  $V_{g,min}$  measured in buffer, a calibration curve ( $\log C$  vs.  $\Delta V_{g,min}$ ) can be plotted (Fig. 3.4 B (circle)), revealing that concentrations down to 10 fM are measurable and achieving a dynamic range of  $>6$  orders of magnitude (i.e., fM - nM). The calibration curve covers

the reference values in serum sample coming from both healthy and unhealthy individuals ( $\leq 100$  fM - hyperthyroidism and  $>10$  pM - hypothyroidism).<sup>181</sup>

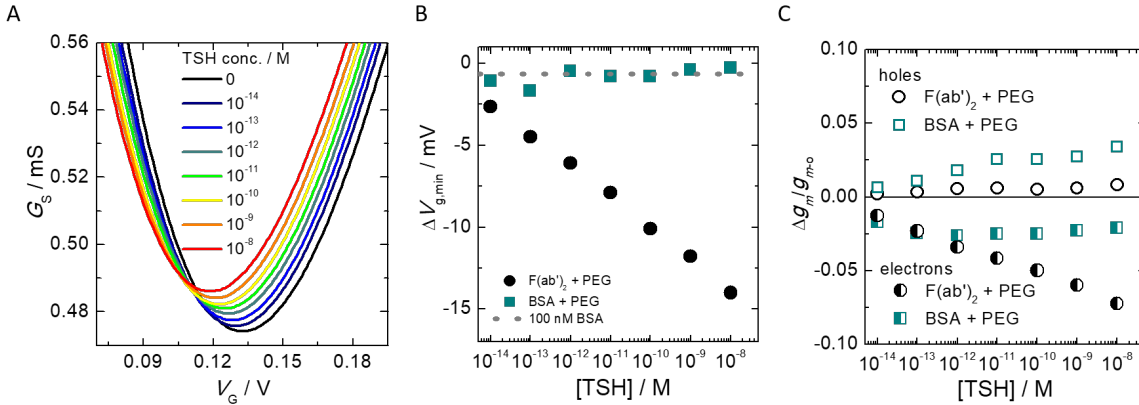


**Figure 3.4** – TSH detection in buffer: **A** Transfer curve of graphene after " $F(ab')_2 + PEG$ " immobilization (dashed line) and after the addition of increasing concentration of TSH (solid lines). **B**  $V_{g,min}$  shift after addition of 100 nM BSA (dotted line) and increasing concentrations of TSH for two different surfaces (calibration curves): active " $F(ab')_2 + PEG$ " (circles) and control " $BSA + PEG$ " (squares). **C** The relative changes in electron and hole transconductance ( $g_m$ ) with respect to the transconductance of  $F(ab')_2$  only ( $g_{m-o}$ ) for the same surfaces as in **B**. This experiment was performed by Dr. Nesha M. Andoy. Adapted from.<sup>59</sup> Copyright 2018 by John Wiley & Sons, Inc.

The asymmetric relative transconductance changes in hole and electron transport upon increasing TSH concentrations are shown in the Fig. 3.4 C (circles). A clear decrease in  $\Delta g_m/g_{m-o}$  for electron transport (Fig. 3.4 C, half-filled circles) is seen, while no clear changes were observed for the hole transport (Fig. 3.4 C, open circle). The said changes however do not exceed  $\sim 7\%$  for electron transport even at 10 nM TSH. A TSH concentration dependent increase in the minimum conductance  $\Delta G_m/G_{m-o}$  can be also seen in the Fig. 3.4 A. From isoelectric focusing experiment, the isoelectric point of TSH (where the net charge of the protein is 0) is  $\sim 6.8$ , TSH is negatively charged at the experimental conditions (pH = 8).<sup>189</sup> Again, the apparent n-doping caused by TSH binding to the biosensor as well as asymmetric changes in charge mobilities, cannot be explained by changes in the carrier density due to electrostatic effects. This is in agreement with what was observed after  $F(ab')_2$  immobilization, and can further confirm that electrostatic effects are not the dominating mechanism by which this graphene device senses analyte binding to  $F(ab')_2$ .

### "Off-target" control experiment

The selectivity of the biosensor towards TSH was assessed by measuring the non-specific adsorption of a well-characterized "off-target" protein, here bovine serum albumin (BSA), which is known to bind unspecifically to graphene surface.<sup>190</sup> Even for very high concentration (100 nM), the  $\Delta V_{g,min}$  recorded is  $\sim 4\times$  less than that from far lower TSH concentration (10 fM) (Fig. 3.4 B, dotted line), showing that non-specific adsorption of non-target proteins is much lower than the signal generated by receptor specific binding.

### "Off-receptor" control experiment

In order to make sure that the analytical signals ( $\Delta V_{g,min}$  and  $\Delta g_m/g_{m-o}$  shifts) are truly originating from the antigen-antibody interaction, a control measurement with "off-receptor" TSH-unspecific was performed. Here,  $F(ab')_2$  was substituted with BSA and co-immobilized with PEG on the graphene surface. Transfer curves obtained with increasing TSH concentrations on an inactive "BSA + PEG" surface are presented in the Fig. 3.6 A. No significant  $V_{g,min}$  change for the control "BSA+PEG" surface is observed with increasing TSH concentrations (Fig. 3.5B (squares)) in contrary to the active " $F(ab')_2$ +PEG" signal observed before in Fig. 3.4B (circles) -  $V_{g,min}$  clearly shifts towards more negative potentials. This confirms that  $V_{g,min}$  can be used as an analytical parameter for the determination of TSH, because it is only subject to change when the specific antigen-antibody binding occurs.

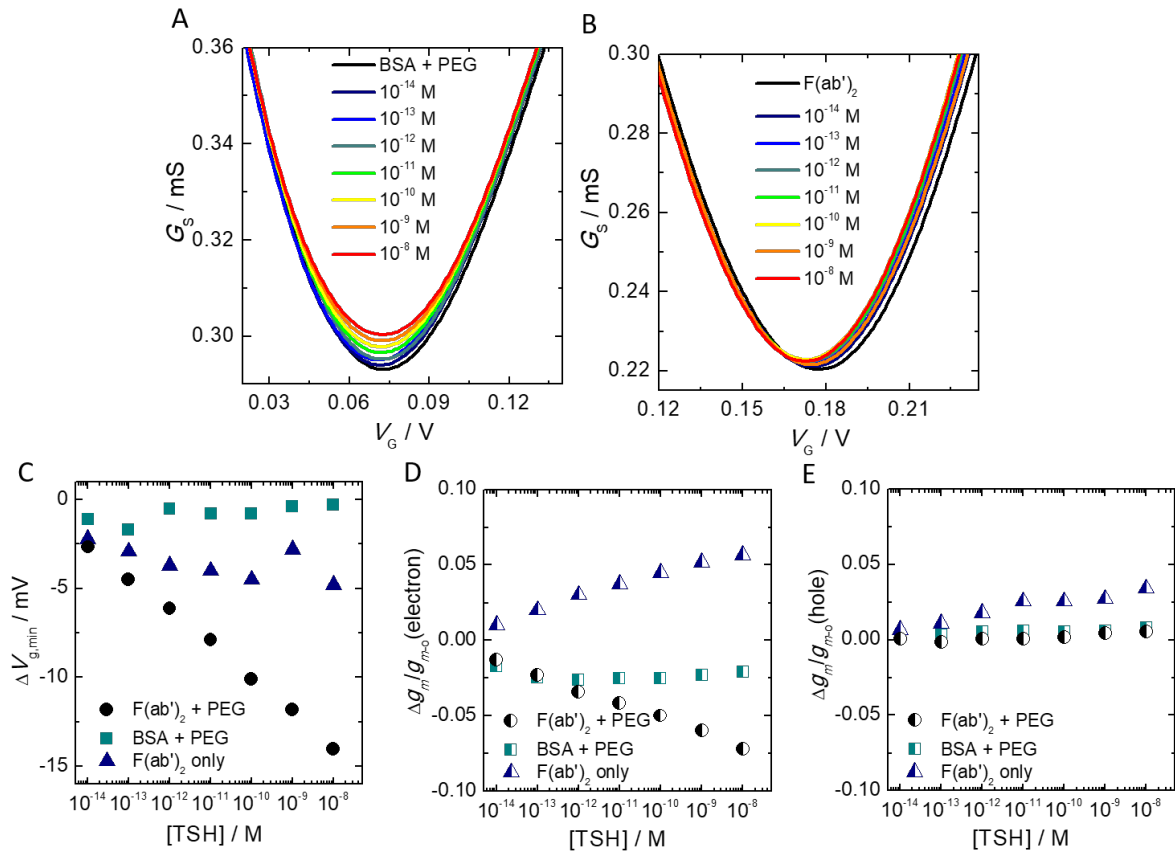


**Figure 3.5** – Transfer curves of GFET devices before and after TSH addition on control surfaces: **A** "BSA + PEG" and **(B)**  $F(ab')_2$  only. TSH concentration dependent changes in  $V_{g,min}$  **C** electron **D** and hole **E** transconductance obtained from the active " $F(ab')_2$  + PEG" (circle) and control: "BSA + PEG" (square) and  $F(ab')_2$  only (triangle) surfaces. Adapted from.<sup>59</sup> Copyright 2018 by John Wiley & Sons, Inc.

Additionally, the non-specific TSH adsorption has an influence on the graphene electron and hole transconductance ( $\Delta g_m/g_{m-o}$ ) as shown in Fig. 3.5C (squares). With increasing TSH concentrations, the electron conductivity of the control surface slightly decreases, similarly to the active surface, but less pronounced (Fig. 3.4 C, circles). When it comes to the hole transport, with increasing TSH concentration, it increases as well, which was not the case for the active surface (Fig. 3.4C), providing another distinction between specific and non-specific interactions. Moreover, TSH concentration-dependent changes in  $\Delta G_{min}/G_{min-o}$  on the inactive surface can be seen, as the minimum conductance increases with increasing TSH concentration, similarly to the active surface (Fig. 3.6, squares). Consequently, the  $\Delta G_{min}/G_{min-o}$  increase cannot be caused by specific antigen-antibody interactions, but rather could be derived from non-specific interactions of TSH with the graphene surface. Therefore, this  $\Delta G_{min}/G_{min-o}$  cannot be used as an indicator of measured TSH concentrations with GFET.

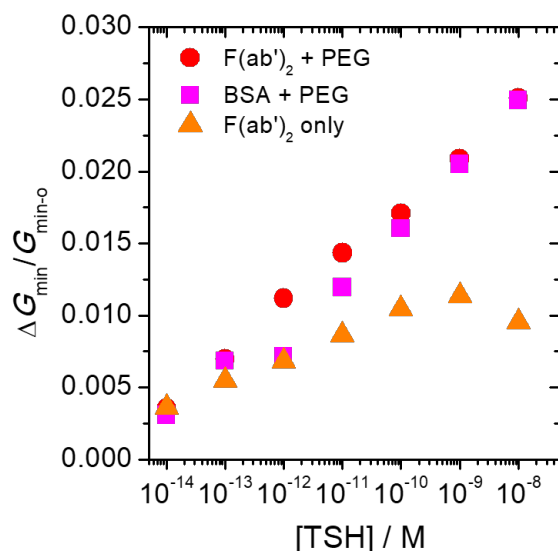


**Figure 3.6** – Relative change in minimum conductance with increasing TSH concentration for different surfaces: active surface "F(ab')<sub>2</sub> + PEG" (circle), inactive surface "BSA + PEG" (square), and F(ab')<sub>2</sub> only (triangle). Adapted from.<sup>59</sup> Copyright 2018 by John Wiley & Sons, Inc.

### The effect of PEG

The basic principle of FET-based (bio)sensors relies on the analyte's charge detection, which enables label-free detection of charged species. As already mentioned, charge screening by high concentrations of ions present in solutions, pose a challenge (Debye screening).<sup>191</sup> The solution proposed earlier<sup>5-7,60</sup> is based on co-immobilization of receptor molecules and the poly(ethylene glycol), which was mechanically described by Haustein et al.,<sup>150</sup> enables the biodetection in physiological solutions. To verify this approach in this work, a control measurements with "F(ab')<sub>2</sub> only" modified graphene and increasing concentrations of TSH were performed (transfer curves - Fig. 3.5 B) and compared with the results obtained with "F(ab')<sub>2</sub> + PEG" modified graphene surface. The changes observed with increasing TSH concentrations are shown in Fig. 3.5 C-E (triangle). The  $\Delta V_{g,min}$

for "F(ab')<sub>2</sub> only" surface decreases similarly to the additionally PEGylated biosensor, but the magnitude of change is only 30% (at 10 nM TSH) of the signal obtained when PEG is present (Fig. 3.4 A). Furthermore, the sensitivity ( $\Delta signal/\Delta concentration$ ) of the "F(ab')<sub>2</sub> only" biosensor ( $\Delta V_{g,min}/\Delta C$ ) is much lower (from 10 fM to 10 nM  $\Delta V_{g,min}$  shifts only -2.6 mV *vs.* -13 mV for "F(ab')<sub>2</sub> + PEG"). Moreover, asymmetric changes in  $\Delta g_m/g_{m-o}$  for electron and hole transport can be observed – electron conductivity increases significantly with increasing TSH concentration (Fig. 3.5 D) while hole conductivity does not change (Fig. 3.5 E). Finally, the minimum conductance  $\Delta G_{min}/G_{min-o}$  increases with increasing TSH concentrations, but less than the PEGylated biosensor (Fig. 3.6, triangle). An approximately 3-fold signal enhancement in the presence of PEG is in agreement with previous reports on gold and carbon nanotube surfaces<sup>7,117</sup> and is further explained by Hausteine et al.<sup>150</sup> Briefly, the mechanism of PEG-induced signal enhancement may be explained within the Donnan potential theory, where the Debye screening starts to occur at the surface layer/electrolyte interface.

Interestingly, in comparison to the similar work of Gutierrez et al.<sup>7</sup> with gold extended-gate FET configuration using the same F(ab')<sub>2</sub> fragments and PEG as signal enhancement strategy, the limit of detection (LoD) obtained with electrolyte-gated graphene FET is much lower (<10 fM *vs.* 500 fM), which may be attributed to a different detection mechanism.

### 3.2.4 Detection mechanism

Several parameters have been analyzed in the previous sections: **1**) shift in charge neutrality point voltage  $V_{g,min}$ , **2**) change in minimum conductance of the transfer curve  $\Delta G_{min}/G_{min-o}$ , and **3**) hole and electron transconductance changes  $\Delta g_m/g_{m-o}$ . Given the results obtained with specific and non-specific detection of TSH on graphene FET, one could deduce the biosensing mechanisms when using electrolyte-gated graphene field-effect transistor based biosensor (see Paragraph 1.2.2). The most straightforward mechanism for FET-based (bio)detection of charged (bio)molecules is the electrostatic gating effect. Briefly, positively (+) charged (bio)molecules binding to the surface of the (bio)sensor induce n-doping (shifting  $V_{g,min}$  to more negative potentials) and vice-versa, negatively (-) charged (bio)molecules adsorption causes p-doping (shifting  $V_{g,min}$  to more positive potentials) without changing the transconductance.<sup>144,190,192-196</sup> In this work, one can make several observations: 1) negatively charged TSH (-) binding to the surface shifts  $V_{g,min}$  to more negative (-) potentials, positively charged (+) F(ab')<sub>2</sub> immobilization shifts the  $V_{g,min}$  to more positive (+) potentials. Furthermore, non-specific adsorption experiments of a well-characterized BSA<sup>190,197</sup> (IEP = 4.8, therefore negatively (-) charged in pH 8, and positively (+) charged in pH 4) and TSH binding to the bare GFET surface were performed (Fig. 3.7). The transfer curves for BSA (Fig. 3.7 A) and TSH (Fig. 3.7 C) (both positively charged in pH 8) shift to the more negative potentials, whereas in pH 4, where both of the proteins are positively charged, the transfer curves shift to more positive potentials (BSA - Fig. 3.6 B, TSH - Fig. 3.6 D). All of these observations do not agree with the electrostatic gating effect as the detection mechanism, therefore it is excluded from further consideration.

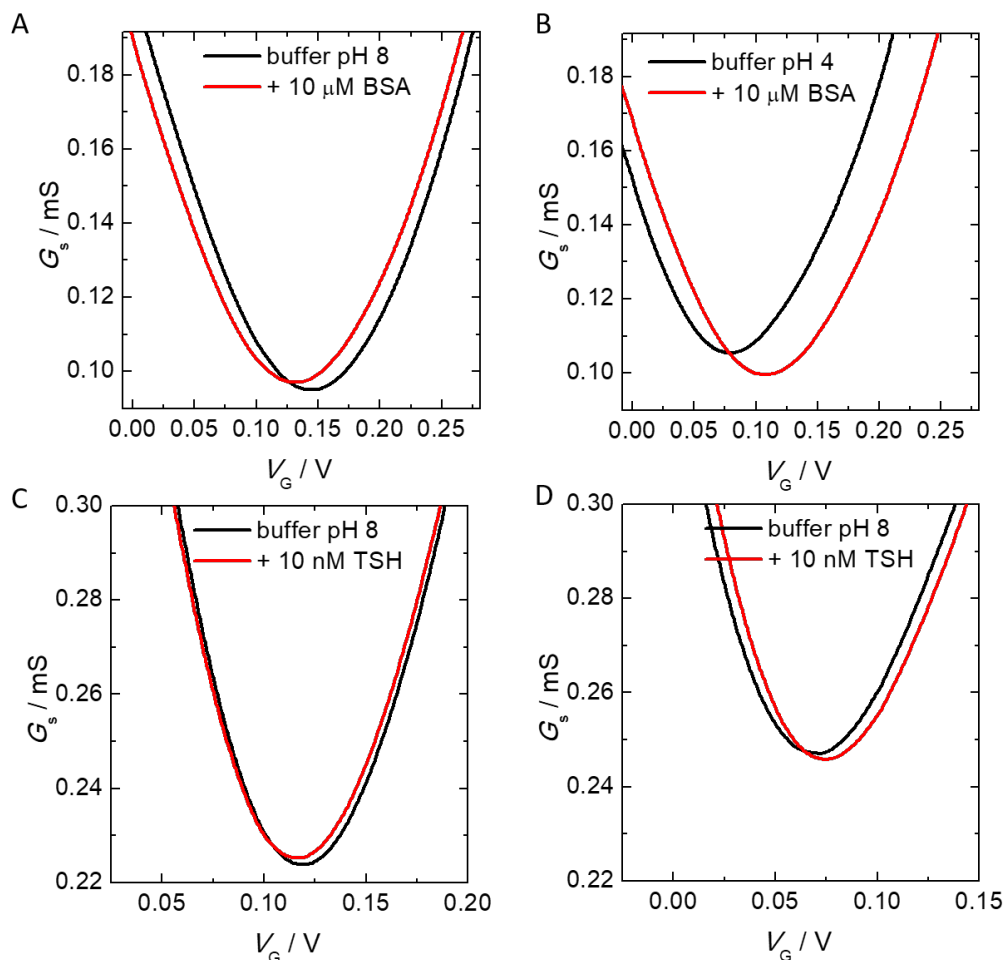


**Figure 3.7** – GFET electronic response towards non-specific detection of BSA and TSH at pH 8 (A & C) and pH 4 (B & D). Adapted from.<sup>59</sup> This experiment was performed by Daniel Vetter. Copyright 2018 by John Wiley & Sons, Inc.

Direct charge transfer could be the reason for the shifts in  $V_{g,min}$ , as previously shown with detection of DNA and protein using a GFET.<sup>197–202</sup> On the other hand, the asymmetric changes in both hole and electron conductivity  $\Delta G_{min}/G_{min-o}$  could not be explained by that effect alone.<sup>70,172,198</sup> The Schottky barrier effect (adsorption of the species on metal contacts) cannot cause these characteristic asymmetric changes and the metal contacts were well-passivated by placing the PDMS slab in a way that only graphene was inside the microfluidic channel with tolerances of at least 500 microns, resulting in very low leakage currents (Fig. 3.8). Therefore, one cannot expect any significant protein-induced energy barrier modulation at the graphene/gold contact (semiconductor/metal Schottky barrier).<sup>58</sup>

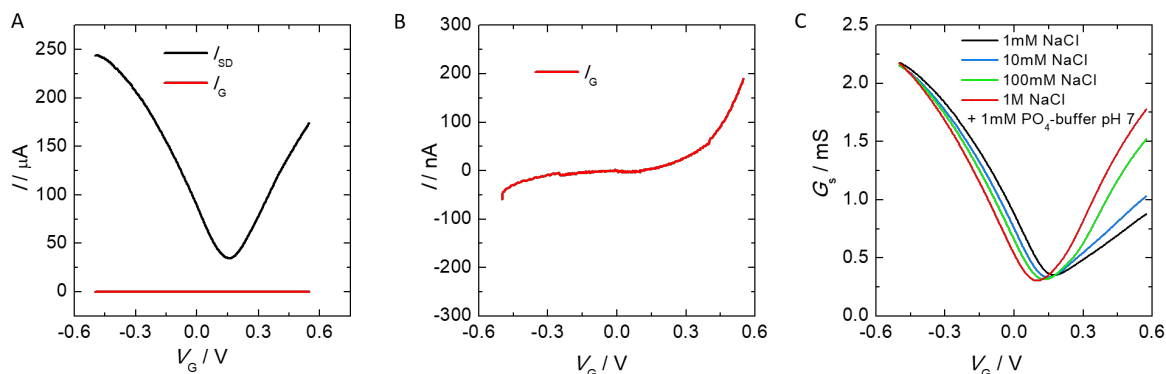


**Figure 3.8** – **A** Drain current ( $I_{SD}$ ) vs. gate current ( $I_G$ ). **B**  $I_G$  as shown in **A** rescaled to show that, compared to  $I_{SD}$ , the gate current is at least 3-orders of magnitude lower **C** Conductance of graphene as a function of gate voltage measured in different salt concentrations. Adapted from.<sup>59</sup> Copyright 2018 by John Wiley & Sons, Inc.

The conductivity of graphene  $\sigma$  for electron and holes is given by the equation:<sup>69</sup>

$$\sigma = \mu \times C_g \times (V_g - V_{g,min}) \quad (3.1)$$

where  $\mu$  is charge carrier mobility,  $C_g$  - gate capacitance,  $V_g$  - gate voltage and  $V_{g,min}$  - minimum gate voltage.

From this equation it is evident that the charge carrier mobility  $\mu$  and the gate capacitance  $C_g$  can change the conductivity of graphene  $\sigma$  and thus the transconductance (slope of the transfer curve). Upon protein adsorption one can see the transconductance decrease, which can be caused by a capacitance decrease,<sup>203</sup> since  $C_g$  is proportional to the permittivity of the interface. Generally, proteins and polymers have a lesser permittivity than the electrolyte solution.<sup>6,58,204</sup> Capacitance modulation cause the symmetric slope changes in transfer curves<sup>6,58</sup> and cannot explain the asymmetric changes in hole and electron conductivity upon protein adsorption. Therefore, with the GFET biosensor presented in this work, the observed changes in conductivity  $\sigma$  are not caused by the capacitance change  $C_g$ , but rather by changes in charge carrier mobility  $\mu$ .

The mobility of holes and electrons in graphene can be a subject of change due to scattering at charged impurities.<sup>70,125,205,206</sup> It has been shown that with the increase of ionic strength of the electrolyte solution, asymmetric changes in carrier mobilities and a  $V_{g,min}$  shift to more negative potentials occur.<sup>125,206</sup> This phenomenon was explained by Debye screening - the electrolyte ions can screen the effect of charged impurities (see Section 1.2.2). Several transfer curves were recorded in different ionic strengths (from 1 mM to 1 M) and shown in the Fig. 3.8 C. The GFET exhibits asymmetric increase in charge carrier mobility and a  $V_{g,min}$  shift to more negative potentials, which implies that the charge carriers are scattered on the charged impurities present on the surface of graphene. Similarly, upon addition of PEG, a negative shift in  $V_{g,min}$  and a significant asymmetric increase in both hole ( $\sim 10\%$ ) and electron ( $\sim 25\%$ ) mobility occur (Fig. ?? B-D). After  $F(ab')_2$  immobilization and upon TSH binding, a similar asymmetric  $\mu$  change was observed. The electron transport decreased more compared to the hole transport upon adsorption of those proteins, despite being oppositely charged under the experimental conditions. However, their respective net charges determined the direction of the  $V_{g,min}$  shift.

**Table 3.1** – *Detection mechanisms proposed for different Graphene-based FET devices. Adapted from.<sup>59</sup> Copyright 2018 by John Wiley & Sons, Inc.*

Target analyte	Biorecognition Molecule	Proposed detection mechanism	Type of graphene
ssDNA	ssDNA	electrostatic gating	mechanical exfoliation <sup>192</sup> CVD grown <sup>196</sup>
ssDNA	ssDNA	charge doping	CVD grown <sup>198</sup> CVD grown <sup>202</sup>
protein	antibody	electrostatic gating	rGO <sup>193</sup> mechanical exfoliation <sup>194</sup>
protein	antibody & GPCR	charge doping	rGO <sup>197</sup> CVD grown <sup>201</sup>
protein	antibody	charged-impurity scattering	rGO <sup>209</sup> rGO <sup>208</sup>
protein	aptamer	electrostatic gating	mechanical exfoliation <sup>144</sup> CVD grown <sup>195</sup>
protein	aptamer	charge doping	CVD grown <sup>199</sup> CVD grown <sup>200</sup>
protein	aptamer	charged-impurity scattering	rGO <sup>208</sup>

Due to complexity of changes of the GFET electronic properties, it can be concluded that more than one factor contribute to the characteristic transfer curve changes upon analyte binding. Examples of devices using different biosensing mechanisms are listed in the Tab. 3.1. It seems that for the same analyte (e.g. protein), different biosensing mechanisms were proposed. This can be further explained by the differences in the device design and manufacturing, highlighting the importance of standardization of those processes.<sup>207</sup> For the GFET used in this work, the characteristic  $V_{g,min}$  shifts and asymmetric  $\mu$  changes suggest that the major biosensing mechanism is most probably based on modulation of charge scattering by charged impurities, similar to Kim et al. and Mansour et al.<sup>208,209</sup> However, it is not excluded that other biosensing mechanisms can take part in the TSH detection with GFET and further work is needed.<sup>210</sup> Overall, it is clear that the presented TSH specific GFET-based biosensor can be used for quantitative determination of TSH in physiological solutions, which in future could be used for Point-of-Care applications.

### 3.3 Conclusions

Ionic screening of analyte charge has so far limited the use of FET-based biosensors in physiological conditions. An electrolyte-gated graphene field-effect transistor-based biosensor has been constructed by co-immobilizing poly(ethylene glycol) and TSH-specific F(ab')<sub>2</sub> antibody fragments. The biosensor exhibited very high sensitivity of TSH determination ranging from fM to nM concentrations even in high ionic strength buffer. The limit of detection (LoD) was estimated to be  $\sim 10$  fM. This is a significant improvement of analytical parameters over previously published work by Gutierrez et al.<sup>7</sup> using a gold extended-gate FET configuration and similar surface modification. However, more focus has to be devoted to the improvement of parameters like precision of immunosensing and device-to-device variability, which can be addressed by establishing a more robust and reproducible device (mass) fabrication process. Characteristic electronic response of graphene (charge neutrality point voltage shift  $V_g$ , change in minimum conductance  $\Delta G/G_o$  and the changes in hole and electron transconductances  $\Delta g_m/g_{m-o}$ ) towards analyte detection have been carefully examined. Using this approach, one can deduce that the most probable biosensing mechanism for the presented TSH biosensing assay is charge carrier scattering on surface impurities of graphene. Furthermore, the presented GFET-based biosensor addresses the needs of Point-of-Care setting i.e. simplicity and robustness (lack of sample pre-treatment, dilution or washing steps) as well as time to result (<20 min).



# 4 | Observation of direct electron transfer from glucose dehydrogenase to single-sheet graphene

The study described in this chapter will be submitted as "*Observation of direct electron transfer from glucose dehydrogenase to single sheet graphene electrode*" to *Electrochimica Acta* with Marcin S. Filipiak as first author.

## 4.1 Introduction

Diabetes is a group of metabolic disorders characterized by increased blood sugar or glucose levels, which, if left untreated, can cause severe long-term complications. Therefore, measuring glucose levels is important to ensure proper disease management for those diagnosed with diabetes. Glucose biosensors have been under development for more than 60 years since the first report by Clark and Lyons.<sup>1</sup> In this so-called "first-generation" glucose biosensor, the enzyme glucose oxidase (GOx) was employed, which with the help of oxygen as an electron acceptor, was able to oxidize glucose. The glucose concentration was measured indirectly either by measuring the decrease in local oxygen concentration or increase in hydrogen peroxide concentration, a by-product of the enzymatic reaction. The main principle, *i.e.* dependence on and correlation with oxygen concentration, was at the same time a drawback, as the oxygen concentrations in a sample may vary leading to false results. To overcome this issue, oxygen was substituted with an artificial electron acceptor, a mediator, that can be sensed at the electrode ("second generation"). An example of a redox mediator for enzymatic determination of glucose is ferrocene, first demonstrated in 1984.<sup>211</sup> With a smart choice of mediator and the immobilization matrix for the enzyme, researchers were able to lower the effect of interferences present in complex samples (e.g. blood). The trend that has emerged over the last 30 years is to eliminate the mediator and "wire" the enzymes' active center to the electrode to transfer the electrons directly ("third generation"). This phenomenon, called "direct electron transfer" (DET) became a "Mount Everest" for (bio)electrochemists because it would enable studies of direct enzyme-substrate interactions, not limited by the use of additional mediator, and reduce the complexity of the system. DET could be highly advantageous for Continuous Glucose Monitoring (CGM), since so far CGM is based on oxygen as means of cofactor regeneration due to high requirements imposed on implantable devices (*e.g.* non-toxicity excludes the use of mediators). The oxygen molar concentration in venous blood does not exceed 0.2 mM<sup>211</sup> and varies significantly with different conditions. Although there has

been much research on DET in glucose biosensors, most researchers have used oxidases that are oxygen sensitive. Unfortunately, it is difficult to distinguish the proposed DET from the oxygen-mediated pathway, rendering some of the DET claims rather contentious in the light of recent critical reports.<sup>212,213</sup> To circumvent this issue, a possible solution would be to use an oxygen insensitive enzyme such as glucose dehydrogenase, which has been lately shown to facilitate DET.<sup>214</sup> A recent review discusses direct electron transfer of FAD-dependent dehydrogenase complexes, with a special interest in glucose dehydrogenase (GDH).<sup>215</sup> The applications of glucose dehydrogenase have been very limited so far partly due to the enzyme's substrate specificity issues.<sup>216</sup> However, progress in enzyme engineering has led to highly specific GDH that, according to the manufacturer's specification sheet for the GDH used here,<sup>31</sup> has sufficiently high specificity against other sugars such as maltose, galactose and xylose.

Monolayer graphene has been shown to be suitable and advantageous for use in electrochemistry due to fast electron transfer kinetics.<sup>217,218</sup> Quite recently, Kwak et al. proved that it is possible to construct a flexible graphene-based enzymatic glucose sensor on PET foil.<sup>216</sup> On top of that, graphene offers the ability to easily pattern electrodes in different shapes, including 3D structures and flexible substrates, that may be advantageous in designing new biosensor configurations, e.g. for CGM devices.

So far, the term "graphene" in the context of electrochemical glucose biosensors claiming DET has been used to describe different materials including *e.g.* reduced graphene oxide,<sup>219</sup> graphene oxide,<sup>220</sup> nanosheets,<sup>221</sup> nitrogen doped graphene,<sup>222</sup> quantum dots,<sup>223</sup> mesocellular graphene foam<sup>224</sup> or simply flakes<sup>225</sup> with a single exception of graphene grown by chemical vapor deposition (CVD) and transferred onto a glassy carbon electrode.<sup>226</sup> For a comprehensive overview of research on DET with graphene and related materials, see Tab. 4.1. Previous works have claimed that graphene may facilitate DET by: 1) "plugging in" a carbon nanomaterial to access the active site, 2) partially unfolding the protein (GOx) enabling the direct electron transfer to the electrode or simply 3) having a high surface area with excellent conductivity.<sup>227</sup>

In this work, we used CVD grown single-layer graphene directly as the working electrode (WE). The advantage of this material over frequently used (reduced) graphene oxide is its high quality, resulting in higher conductivity, more control over surface modification via non-covalent pyrene chemistry, and reduced probability of competing reactions at defect sites. To study interactions between a single-sheet graphene and oxygen insensitive glucose dehydrogenase, GDH was attached to graphene via short pyrene-based linker molecules. Even though the use of glucose dehydrogenase in combination with graphene was described before,<sup>228</sup> this report was limited to the second generation glucose biosensor (through mediated electron transfer). To the best of our knowledge, direct electron transfer from GDH to graphene has not been observed yet. Due to the small linker size (<1 nm), DET from the enzyme to the graphene electrode may be feasible.

## 4.2 Results and discussion

A microfluidic PDMS channel with PTFE tubing was used to provide the solutions to the electrochemical setup. A CVD-grown single layer graphene was used as a working electrode, Ag/AgCl as reference electrode and a planar on-chip gold electrode was used as a counter electrode (Fig. 4.1 A).

In Fig. 4.1 B, a schematic representation of redox reactions associated with electrochemical glucose biosensing for two different cases investigated in this work are presented. Glucose oxidation catalyzed by glucose dehydrogenase involves two major redox steps: 1) glucose oxidation coupled with reduction of flavin adenine dinucleotide (FAD) to its hydroquinone form – FADH<sub>2</sub><sup>25</sup> and 2) active site regeneration by the final electron acceptor. In this work, the regeneration was performed: 1) directly on the electrode (direct electron transfer, DET) or 2) with a redox mediator (mediated electron transfer, MET) – in here nitrosoaniline (NA).

When direct electron transfer is considered, the enzyme's cofactor is regenerated directly by transferring an electron to the electrode when a suitable potential is applied (Fig. 4.1 A). In the case of the nitrosoaniline derivative (specifically *N,N*-bis(hydroxyethyl)-3-methoxy-4-nitrosoaniline), the mediator must be first pre-activated by the enzymatic oxidation of glucose in order to be sensed electrochemically (in other words - the first glucose oxidation cycle, activates the mediator, which then can be used for further "cycling"). In presence of glucose a nitrosoaniline derivative (Fig. 4.1 A - 1.) is reduced to hydroxylamine in contact with the reduced form of the enzyme's cofactor (2.). It hydrolyses homogenously to chinodiimine (3.), which then can undergo reduction with another simultaneous oxidation of FADH<sub>2</sub> to FAD present in the enzyme. The product of chinodiimine reduction – phenyldiamine (4.) can be electrooxidized on the electrode giving a glucose dependent amperometric signal.

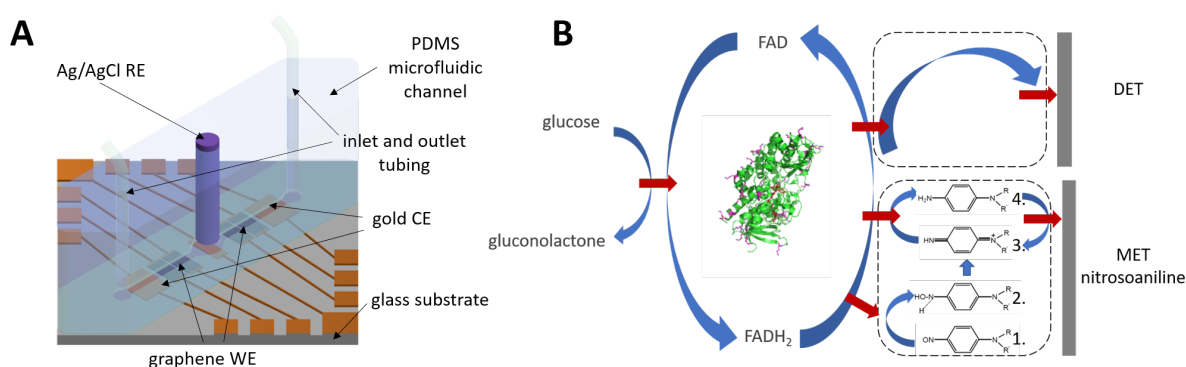


**Figure 4.1** – **A** Microfluidic 3-electrode electrochemistry setup on glass substrate with single sheet graphene as WE, gold planar electrodes as CE and bulk Ag/AgCl as RE. A PDMS microfluidic channel was placed on top. **B** Reaction scheme of different glucose biosensing pathways using glucose dehydrogenase described in this work. Path 1 is a direct electron transfer (DET); Path 2 is mediated electron transfer (MET) with nitrosoaniline used as a mediator.

To construct a glucose specific biosensor, the graphene WE was modified with appropriate glucose selective enzyme – in this work - flavin adenine dinucleotide, FAD-dependent glucose dehydrogenase. First, the bare graphene was functionalized non-covalently with a well-known pyrene derivative by means of  $\pi$ - $\pi$  stacking<sup>36</sup> which formed a monolayer on the graphene surface (Fig. 4.2 A-B)). Here, 1-pyrenebutyric acid *N*-hydroxysuccinimide ester (PBA-NHS) was chosen as a linker molecule (Fig. 4.2 B). The activated linker was later used to couple the  $\text{NH}_2$  residues from surface lysines of glucose dehydrogenase (Fig. 4.2 C). This resulted in a non-oriented covalent immobilization of the enzyme on the linker-modified electrode. Raman spectroscopy is a valuable technique to characterize a variety of parameters (doping, defects, strain, number of layers) of single layer graphene.<sup>73,74</sup> Raman characterization of untreated (Fig. 4.2 D, red), pyrenebutyric acid (PBA)-functionalized (Fig. 4.2 E, blue) and GDH-PBA-functionalized (Fig. 4.2 F, green) graphene films on glass substrates was performed. This spectroscopic technique was used to probe the quality of the graphene film and confirm the molecular functionalization in conjunction with the presented electrochemical measurements. The untreated graphene Raman spectrum (Fig. 4.2 D) depicts the prominent G mode peak of graphene at  $1589\text{ cm}^{-1}$ . The low D-peak ( $\approx 1350\text{ cm}^{-1}$ ) intensity of the graphene film serves as a quality indication of the film. After the PBA functionalization of graphene, the appearance of Raman peaks associated (Fig. 4.2 E, blue spectrum) with a self-assembled layer of PBA on graphene<sup>37</sup> was observed. Following the GDH functionalization of PBA-treated graphene films, an increase in the peak intensity of Raman peaks around  $\approx 1520\text{ cm}^{-1}$  was observed (Fig. 4.2 F). The latter peak of a lower intensity is also present in the PBA-treated sample.

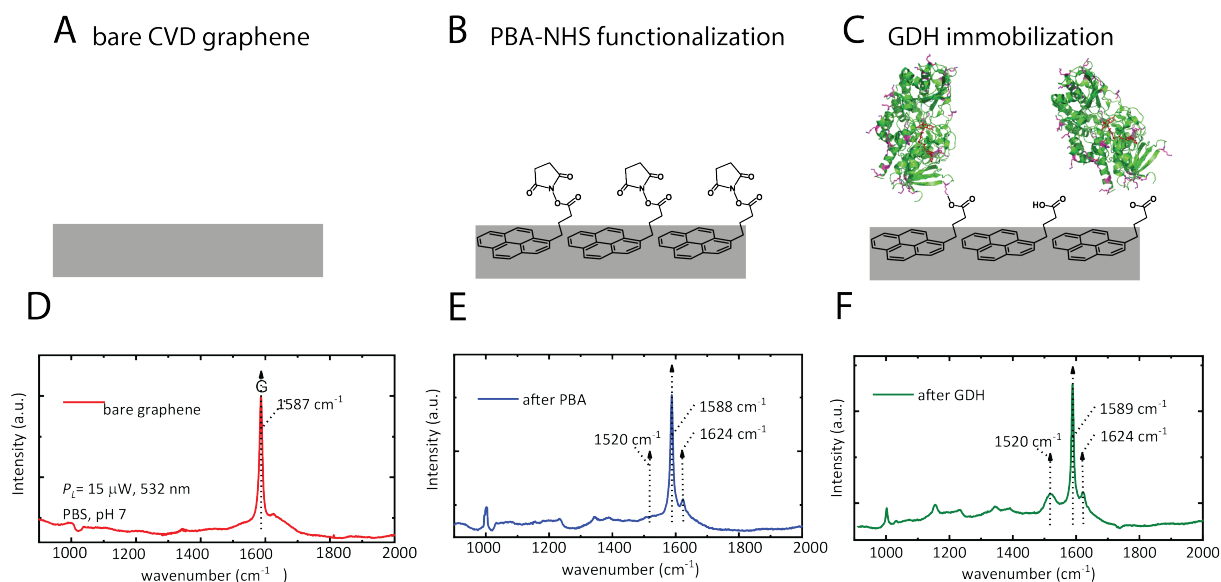


**Figure 4.2** – Surface functionalization and enzyme immobilization scheme - **A** bare graphene electrode, **B** 1 mM 1-pyrenebutyric acid *N*-hydroxysuccinimide ester – PBA-NHS monolayer **C** 1 mg/mL glucose dehydrogenase (GDH). Raman spectra of bare (**D**, red), PBA-NHS functionalized (**E**, blue) and GDH functionalized (**F**, green) graphene film. Raman measurements were performed by Kishan Thodkar (BioMed X GmbH).

An increasing peak intensity ( $\approx 1520 \text{ cm}^{-1}$ ) with increasing GDH concentration is shown in Fig. 4.3 A. Furthermore, a consistent up-shift of one wavenumber in G peak position in each step of functionalization with the PBA and GDH functionalization was observed. This shift in the G peak position can be correlated with the change in the charge carrier density of the graphene film ( $0.5 \text{ cm}^{-1} \approx 2.4 \times 10^{11} \text{ cm}^{-2}$ ).<sup>229</sup> After the functionalization, a charge carrier density change of  $\approx 5 \times 10^{11} \text{ cm}^{-2}$  could be estimated. Since the direction of the peak shift is towards higher wavenumber, our functionalization process has a hole doping effect on the graphene film (see Fig. 4.3 B for further Raman characterization).

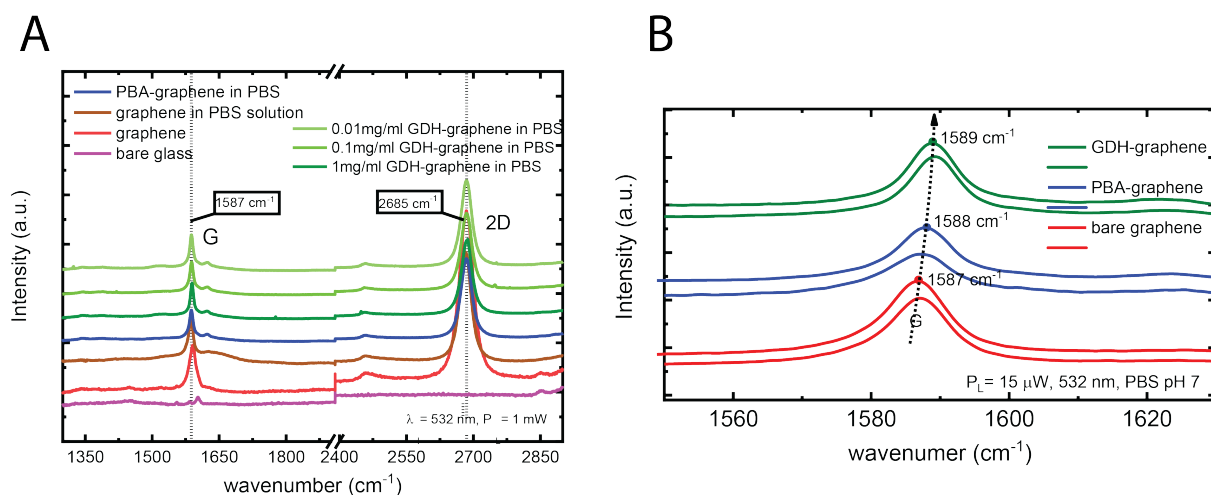


**Figure 4.3** – **A** Raman characterization of bare glass (magenta), graphene in air (red), graphene in PBS solution (brown), PBA-NHS functionalized (blue), GDH functionalized (different concentration, green). **B** Raman spectra of G peak of bare graphene (red), PBA-NHS functionalized (blue), GDH functionalized (green). Note the blue-shift of the peak position after each step of functionalization. Raman measurements were performed by Kishan Thodkar (BioMed X GmbH).

### 4.2.1 Direct electron transfer

While performing cyclic voltammetry measurements with graphene working electrode and without any redox mediator, a pronounced glucose dependent signal as seen from Fig. 4.4 A was observed. To make sure that this oxidation current increase was caused by the enzymatic reaction of glucose oxidation, a control experiment was performed, where the graphene surface without the enzyme was exposed to different glucose concentrations and cyclic voltammograms were recorded (see Fig. 4.4 B). The apparent oxidation current decreases slightly with increasing glucose concentration, which may be due to the oxidation of adsorbed species (contaminants) on the graphene surface. The calibration curves for bare and GDH modified graphene electrode are plotted in Fig. 4.4 C. Since there is no current increase without the enzyme, a conclusion can be made that the glucose dependent current increase observed with the enzyme-coated graphene must be due to the enzymatic activity, even though no redox mediator is present in solution. This behavior may be explained by direct electron transfer (DET) from the active center to the electrode.

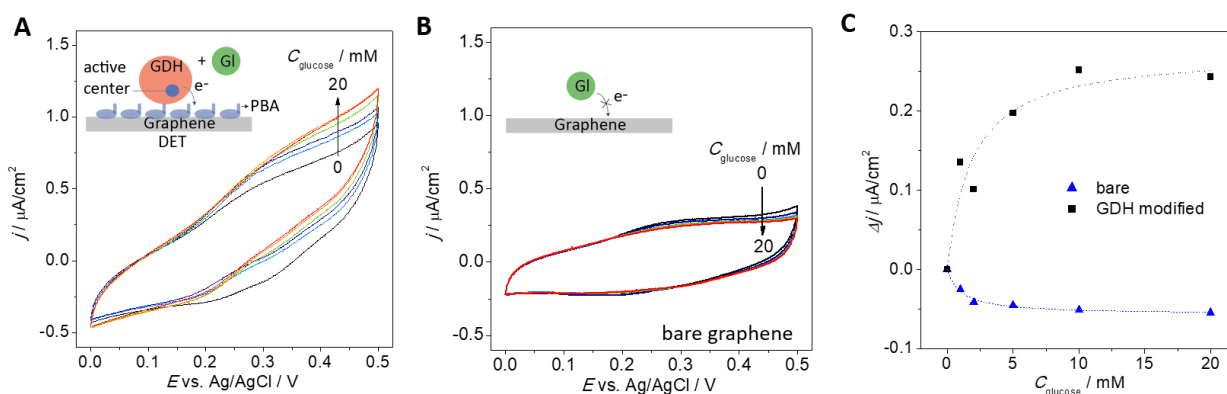


**Figure 4.4** – Direct electron transfer from the cofactor of GDH on graphene/PBA-NHS/GDH electrode. **A** Typical cyclic voltammetry curves of non-mediated enzymatic glucose oxidation (10 mV/s, PBS pH 7). Inset: schematic representation of DET on graphene coated with PBA-NHS and GDH. **B** Typical cyclic voltammetry curves of bare graphene electrode in presence of different concentrations of glucose (10 mV/s, PBS pH 7). Inset: schematic representation the bare graphene in contact with glucose solution. No DET occurred in this case. **C** Calibration curves of glucose biosensing using direct electron transfer on graphene/PBA-NHS/GDH electrode. A glucose concentration current increase is clearly seen for GDH modified electrode, while for bare graphene electrode an insignificant current decrease is seen.

To further investigate the DET pathway and to make sure that the pyrene linkers do not contribute to the glucose oxidation, GDH-modified with pyrene-coated graphene was compared. These experiments were performed in a PDMS well electrochemical cell format to simplify the setup by removing active fluidics (see Chapter 6). Cyclic voltammograms were recorded using PBA-NHS modified graphene electrode without (Fig. 4.5 A) and with immobilized GDH (Fig. 4.5 B).

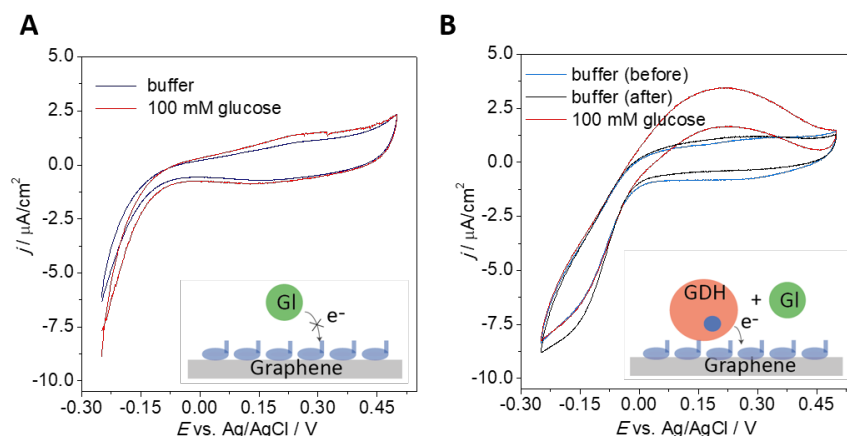


**Figure 4.5** – **A** Control experiment with graphene/PBA-NHS electrode showing no current increase in presence of 100 mM glucose. **B** Enzymatic electrooxidation of glucose on graphene/PBA-NHS/GDH modified electrode.

For the case of PBA-NHS functionalized graphene (Fig. 4.5 A), no current increase was recorded upon addition of 100 mM glucose. For the case of GDH modified graphene electrode (Fig. 4.5 B), an obvious oxidation current increase was seen when 100 mM glucose was added. Furthermore, the voltammograms before and after glucose addition match each other meaning that there is no glucose adsorption on the surface of GDH modified graphene electrode. This control experiment confirms that the enzyme GDH is responsible for glucose oxidation and not the pyrene linker molecules.

Next, chronoamperometric measurements were performed in a well setup (Fig. 4.6 A). During a glucose measurement in blood, electrochemical interferences may occur and lead to incorrect glucose values. Therefore, the influence of interferences must be carefully considered when developing a glucose sensor. One of the most severe sources of interference in electrochemical blood glucose measurement is ascorbic acid (AA)<sup>230</sup> with 0.08 mM upper limit of reference values in plasma.<sup>231</sup> Without AA, a clear glucose dependent signal was observed. With AA, there was significant ascorbic acid oxidation current. To distinguish the current changes due to the glucose oxidation from the current coming from the ascorbic acid oxidation, the background must be subtracted first. The following empirical function was used to subtract the background:  $y = a - b \times \ln(x + c) + d \times x$ , where  $y$  is the current and  $x$  is the time of the experiment. The chronoamperograms can be seen on Fig. 4.6 A (before) and B (after subtraction). After subtracting the background signal (AA oxidation current), it can be clearly seen (Fig. 4.6 B) that the currents due to glucose addition are much smaller with AA than without. The calibration curves are plotted in Fig. 4.6 C.

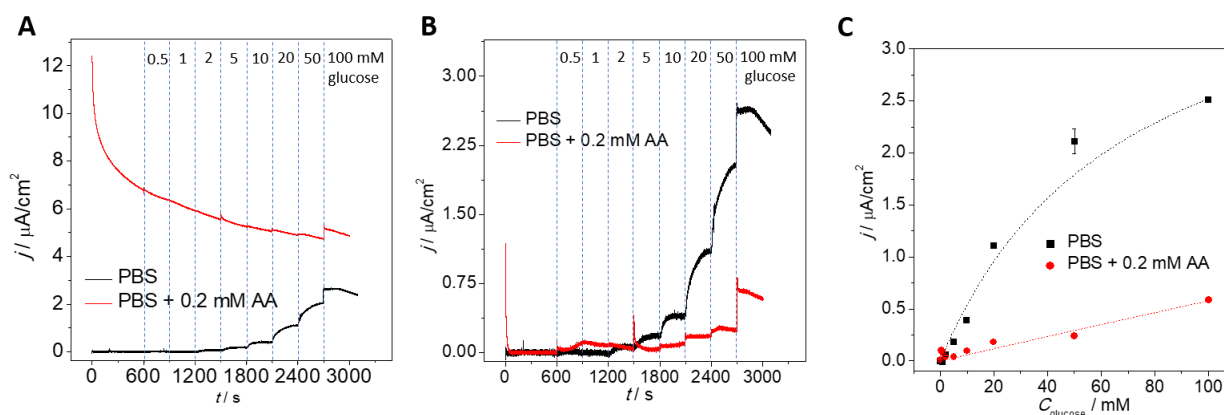


**Figure 4.6** – **A** A chronoamperometric response of the enzyme-coated graphene to different glucose concentrations in PBS in absence (**black**) and in presence (**red**) of 0.2 mM ascorbic acid (without mediator). **B** The chronoamperogram from A with the background current subtracted. **C** Calibration curves in absence (**black squares**) and in presence (**red circles**) of 0.2 mM ascorbic acid after background subtraction.

The expected Michaelis-Menten behavior is observed with estimated  $K_M = 68$  mM from fitting the data with the following equation (black line in Fig. 4.6 C):  $\Delta j = (\Delta j_{max} \times C_{glucose}) / (K_M + C_{glucose})$ , where  $\Delta j$  is the absolute current increase,  $\Delta j_{max}$  the maximal absolute current increase,  $C_{glucose}$  the glucose concentration. The estimated  $K_M$  exactly matches the value provided by the producer of the enzyme ( $K_M = 68$  mM, BBI solutions), confirming that the enzyme activity is fully preserved on the graphene surface.

### 4.2.2 Mediated electron transfer using ferrocenemethanol as a redox mediator

To test if the immobilization protocol preserved the activity of the enzyme, the conventional ferrocenemethanol mediator was explored for glucose biosensing using cyclic voltammetry. We performed several cyclic voltammetry experiments with increasing glucose concentration using FAD-GDH modified graphene electrode. The voltammogram has a shape typical of reversible one-electron redox reactions. The peak-to-peak separation is  $\Delta E_p = 121$  mV and the formal redox potential is  $E^\circ = 0.232$  V vs. Ag/AgCl (3M KCl). For a redox process involving one electron, the theoretical value of the peak-to-peak separation should be 59 mV, which indicates that the resistance of the microfluidic electrochemical cell is relatively high. As one can see in the Fig. 4.7 A, there is a ferrocenemethanol oxidation peak increase with increasing glucose concentrations, while the reduction peak of ferrocenemethanol is barely affected by the increasing concentration of glucose in the solution. As one can see in the Fig. 4.7 B, a significant oxidation current increase was observed for buffer containing ascorbic acid and ferrocene. In comparison with the buffer without AA, the reduction peak of ferrocenemethanol was suppressed, and the oxidation peak current is 3 times higher (w/o vs. w/ AA). On top of that, the curves' peak currents and potentials are not as predictable as the ones for the curves recorded without AA. To make a calibration curve, the absolute current density increase ( $\Delta j$ ) was considered at 0.45 V (in diffusion-controlled regime of the electrooxidation reaction), which is defined here as follows:  $\Delta j = j_{\text{glucose}} - j_{\text{blank}}$ , where  $j_{\text{glucose}}$  – oxidation current density for the concentration of glucose,  $j_{\text{blank}}$  – oxidation current density of ferrocenemethanol in buffer without any glucose. The calibration curve is plotted in Fig. 4.7 C.

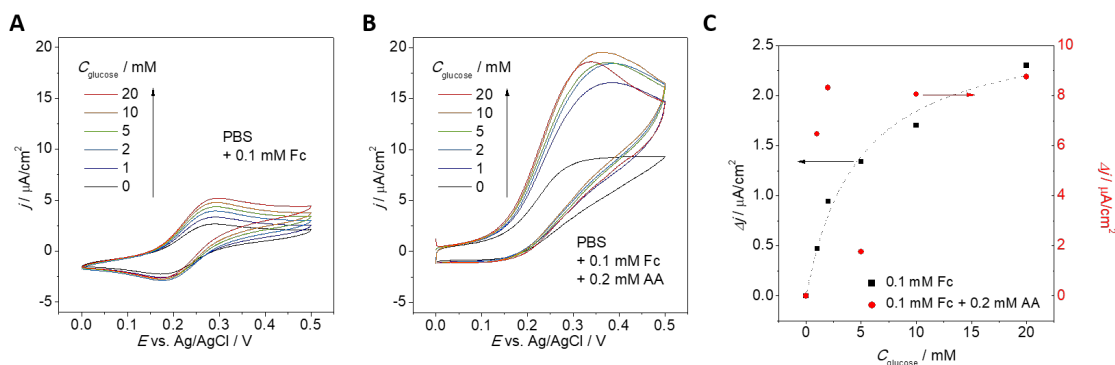


**Figure 4.7** – Ferrocenemethanol as a conventional redox mediator in glucose biosensors. **A** Typical cyclic voltammetry curves of FcMeOH mediated glucose oxidation, an increase in glucose concentration increases the FcMeOH electrooxidation signal (scan rate: 10 mV/s, solution: 0.1 mM FcMeOH in PBS pH 7) **B** Typical cyclic voltammetry curves of FcMeOH mediated glucose oxidation in presence of 0.2 mM ascorbic acid. **C** Calibration curves of glucose biosensing with FcMeOH with (red circles) and without (black squares) 0.2 mM ascorbic acid in solution. This set of measurements was performed by Daniel Vetter (BioMed X GmbH).

The calibration curve for the case without AA presents a typical Michaelis-Menten behavior, while for the case with AA the calibration curve is not predictable in a straight-

forward manner. Additionally, the difference between the first concentration tested and the “blank” is much higher indicating some additional chemical reactions in the system.

Using ferrocenemethanol as an electron mediator confirmed that the enzyme was successfully immobilized and retained its activity on the surface. Upon exposure to a model interferent – ascorbic acid, the performance of the biosensor to distinguish different concentration of glucose dropped significantly. The recorded voltammograms with ascorbic acid showed that there is some interaction between ferrocene derivative and ascorbic acid itself leading to unpredictable and high oxidation currents and lack of a reduction peak. The catalytic behavior of ferrocene derivatives towards ascorbic acid oxidation is well-known<sup>232</sup> and shown in the Fig. 4.8.

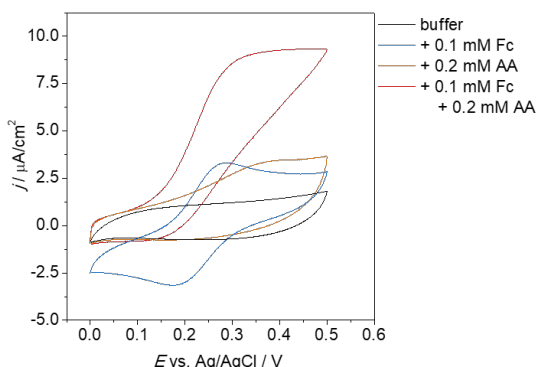


**Figure 4.8** – Cyclic voltammograms of a G/PBS-NHS/GDH in different solutions: PBS pH 7 only (black), PBS pH 7 with addition of mediator 0.1 mM FcMeOH, PBS pH 7 with addition of 0.2 mM ascorbic acid (orange), PBS pH 7 with addition of 0.2 mM ascorbic acid and 0.1 mM FcMeOH.

Finally, using the Randles-Sevcik equation (see 1.11) and taking the voltammogram recorded with bare graphene electrode (Fig. 4.9) one can calculate the electroactive surface area to be  $A = 2.003 \text{ mm}^2$ , which is about 18% less than the estimated geometric surface area. The difference may come from defects and impurities present on the surface of graphene as well as the PDMS "self-passivation". The same electrode was also used to confirm that the glucose itself is not electrooxidized on the surface of graphene.

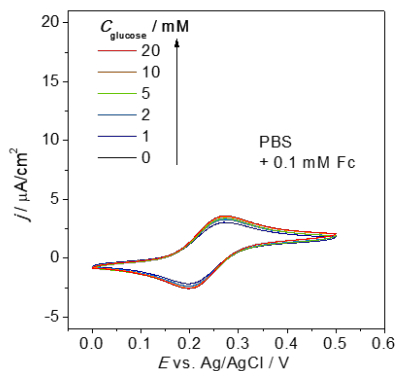


**Figure 4.9** – Cyclic voltammogram of bare graphene electrode in different glucose solutions in PBS pH 7 with addition of 0.1 mM ferrocenemethanol.

### 4.2.3 Mediated electron transfer using nitrosoaniline as a redox mediator

To overcome the electrochemical interference limitations in glucose biosensing, a nitrosoaniline derivative (NA) was employed as a mediator, which is not affected by electrochemical interferents. Several cyclic voltammograms in pure PBS and in PBS with 10 mM nitrosoaniline (Fig. 4.10 A) were recorded. Both CV measurements overlap confirming that without the substrate (glucose) there is no redox signal increase. Afterwards, the influence of ascorbic acid on nitrosoaniline oxidation (Fig. 4.10 B) was examined. With AA only in solution, an ascorbic acid peak at  $\sim 0.25$  V vs. Ag/AgCl can be seen. When NA is added, one can observe that the oxidation of ascorbic acid and nitrosoaniline add up with no catalytic effects. Also, the ascorbic acid oxidation peak disappears in favor of the overall shape determined by nitrosoaniline oxidation cyclic voltammogram.

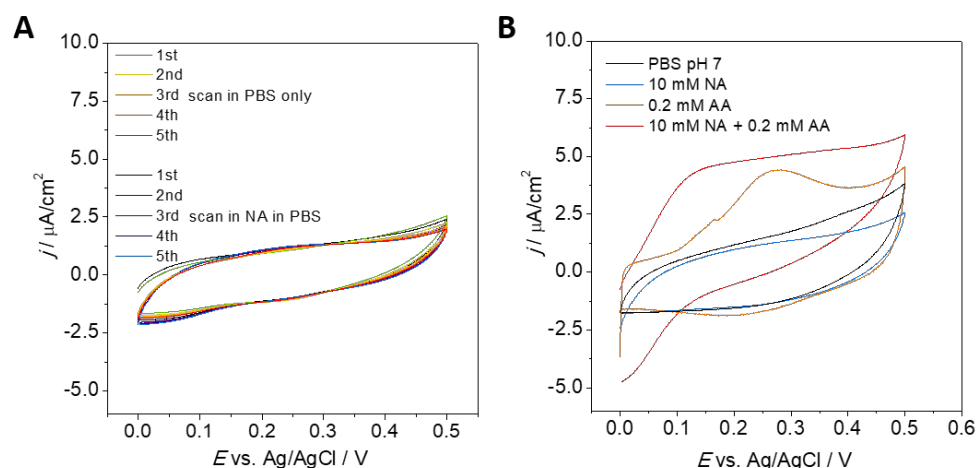


**Figure 4.10** – Nitrosoaniline electrochemistry on graphene. **A** Consecutive (1-5) cyclic voltammograms of graphene/PBA-NHS-GDH electrode in PBS pH 7 and in 10 mM NA (10 mV/s) **B** Cyclic voltammograms of graphene/PBA-NHS-GDH in pure PBS pH 7 (black), 10 mM NA (blue), 0.2 mM AA (orange) and 10 mM NA + 0.2 mM AA (red) in PBS pH 7.

Next, several cyclic voltammetry experiments with increasing glucose concentration using graphene/PBA-NHS-GDH electrode in presence of nitrosoaniline (Fig. 4.11 A) were performed. There are no clearly developed oxidation peaks, yet an overall oxidation current increase with increasing glucose concentrations is seen. For the case with AA (Fig. 4.11 B), one can see a very similar trend of current increase offset by  $\sim 3 \mu\text{A}/\text{cm}^2$ . The calibration curve of glucose concentration vs. absolute current increase (readout at  $E = 0.45 \text{ V}$ ) was plotted in Fig. 4.11 C and the results obtained for the case with and without AA match each other.

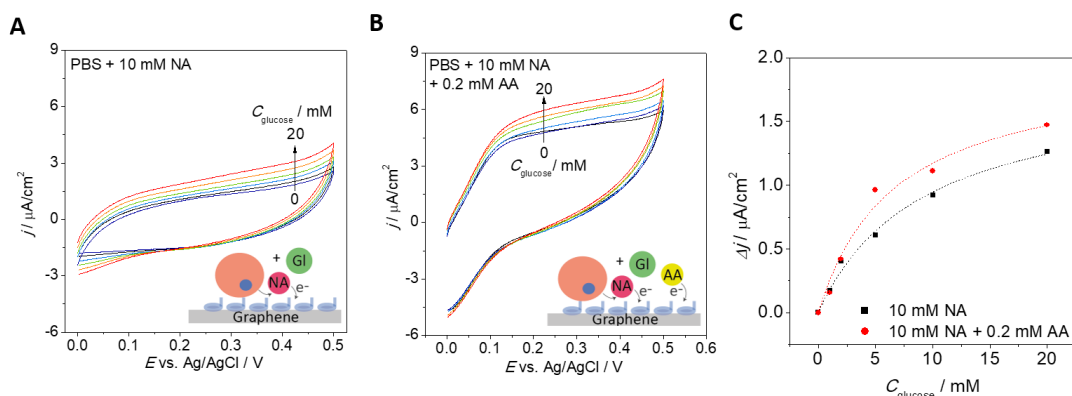


**Figure 4.11** – Nitrosoaniline as a redox mediator in glucose biosensors. **A** Typical cyclic voltammetry curves of NA mediated glucose oxidation ( $10 \text{ mV}/\text{s}$ ,  $10 \text{ mM}$  NA in PBS pH 7) **B** Typical cyclic voltammetry curves of NA mediated glucose oxidation in presence of  $0.2 \text{ mM}$  ascorbic acid.  $10 \text{ mV}/\text{s}$ ,  $10 \text{ mM}$  NA in PBS pH 7 **C** Calibration curves of glucose biosensing with NA with and without  $0.2 \text{ mM}$  ascorbic acid in solution.

#### 4.2.4 Discussion

Here, an enzymatic electrode consisting of a single-layer graphene functionalized with glucose dehydrogenase was used for glucose determination. We evaluated different pathways of glucose enzymatic oxidation on graphene electrodes: 1) based on direct electron transfer (DET) and 2) based on mediated electron transfer (MET) using the relatively unexplored nitrosoaniline (NA) derivative (*N,N*-bis(hydroxyethyl)-3-methoxy-4-nitrosoaniline). Compared to conventional mediators such as ferrocenemethanol, which was explored in the Section 4.2.2 (Fig. 4.7, 4.8 and 4.9), nitrosoaniline is much less affected by cross-reactivity with interferents. On the other hand, ferrocenemethanol is readily available to act as an electron mediator and produces more electrochemical signal, whereas nitrosoaniline must be pre-activated first, which is done enzymatically and thus limited by enzyme turnover. The limiting step of the NA reaction mechanism seems to be the enzymatic activation of nitrosoaniline to chinodiimine - the electrooxidation reaction rate is higher than the enzymatic activation, which is confirmed by the lack of oxidation peaks of phenyldiimine. As a result, there are no "background" redox peaks as in the case of ferrocenemethanol, which means that any recorded current increase will be associated with glucose oxidation.

Regarding the DET pathway, a recent editorial in *Biosensors and Bioelectronics* discussed the inability of native glucose oxidase, a similar simple flavoprotein, to undergo direct electron transfer.<sup>213</sup> The most explored, yet unconvincing evidence for it is based on direct electrochemistry of FAD/FADH<sub>2</sub> pair about -450 mV *vs.* Ag/AgCl. These characteristic peaks were also observed by Vogt<sup>233</sup> with redox titrations showing that the formal potential for free FAD at pH 7.4 is -0.417 V *vs.* Ag/AgCl and -0.302 V *vs.* Ag/AgCl for the bound (expected when considering DET). In a recent critical article<sup>212</sup> the authors argue that most studies claiming direct electron transfer on nanostructured electrodes were not carried out carefully and conscientiously. Appropriate control measurements were not always performed, and the only evidence provided by many researchers was the presence of peaks around -450 mV. However, their source was not necessarily the glucose oxidase itself. With a series of simple experiments with attaching free flavin or catalase, Bartlett and Al-Lolage mimic the "Holy Grail" FAD/FADH<sub>2</sub> peaks and conclude that the mentioned redox peaks come from the contaminants of glucose oxidase. If non-deoxygenated buffers were used and voltammograms recorded in the range where one could expect FAD/FADH<sub>2</sub> peaks,<sup>213</sup> it cannot be excluded that the glucose detection mechanism in a vast majority of the articles claiming DET on graphene may be based on O<sub>2</sub> depletion, rather than on DET (for the comprehensive list of articles where this may be the case, see Tab. 4.1). This would classify these reported devices as "first generation" rather than "third generation" glucose biosensors. Therefore, it was postulated,<sup>213</sup> that there is a need to develop new enzymes, in particular dehydrogenases, since they are oxygen independent. Unfortunately, so far, the use of glucose dehydrogenases has been limited mainly due to specificity issues, yet this has been overcome with recent advances in FAD-GDH protein engineering.<sup>25</sup> The GDH enzyme used here is highly specific for glucose, as mentioned in the introduction.

The direct electron transfer at a distance above 1.7 nm is unmeasurably small.<sup>265</sup> In a native glucose oxidase, the active center - FAD/FADH<sub>2</sub> is buried deeper than 1.7 nm, therefore a DET is very unlikely to be measured. Interestingly, in a recent publication,<sup>266</sup> researchers demonstrated that DET is possible with FAD-dependent glucose dehydroge-

Table 4.1 – Articles claiming direct electron transfer on graphene modified electrodes.

Electrode type	Detection technique	Mediator	Limit of detection	Dynamic range	Sample	Ref
1 GCE/polyvinylpyrrolidone-protected graphene/polyethylenimine-functionalized ionic liquid/ GOD	CV: -0.6 - 0.2 V; 50 mV/s; read-out @ -0.49 V	O2	n/a	2-14	0.05 M PBS pH 7.4	231
2 GCE/rGO/CNT-GOD	CV: -0.8 - 0.0 V; 0.1 V/s; Amperometry @ -0.5 V	O2	n/a	1-8	0.1 M PBS pH 7	235
3 GCE/rGO/CNT-GOD/Nafion	Amperometry @ RDE 0.35 V, 1500 rpm	O2	0.0047 (w/ mediator)	0.01 - 6.5 (w/ mediator)	0.1 M PBS pH 7, 1:5 diluted blood serum, 1:100 diluted urine	236
4 GCE/graphene (CVD) /AuNP/GOD/Nafion	CV: -0.5 - 0.9 V; 50 mV/s; amperometry @ RDE 0.8 V, 750 rpm	O2	0.004	0.010 - 0.366	0.1 M PBS pH 7	236
5 GCE/rGO-GOX (one step preparation)	CV: -0.7 - 0.1 V; 50 mV/s;	O2	n/a	0.1 - 27	0.1 mM PBS pH 7, 1:5 diluted human serum	237
6 GCE/CNT/graphene/AuNP/GOD	Amperometry @ -0.45 V	O2	0.0048	0.005 - 2.1	0.1 M PBS pH 7; undiluted human serum	238
7 GCE/electrochemically reduced carboxyl graphene (ERCGr)/GOD	CV: -0.7 - 0.0 V; 100 mV/s	O2	0.02	2 - 18	0.05 M PBS pH 7.4	239
8 GCE/graphene+chitosan/GOD	CV: -0.7 - 0.1 V; 100 mV/s	O2	0.02	0.08 - 12	0.05 M PBS pH 7.4 + 0.1 M KCl	240
9 GCE/AuNP+PANI+graphene-GOD+chitosan	Amperometry @ -0.55 V	O2	0.0006	0.004 - 1.12	0.1 M PBS pH 7.4, standard glucose samples, human serum samples	241
10 GCE/electrochemically reduced graphene oxide (ERGO)/GOD	CV: -0.7 - 0.0 V; 25 mV/s;	O2	n/a	1-8	PBS pH 7.4	242
11 GCE/ERGO/chitosan/ZnO2-GOD/Nafion	Amperometry @ -0.4 V	DET (?)	0.00456	0.2 - 1.6	0.1 M PBS pH 7.4	243
12 GCE/graphene+Cds+GOD+Nafion	CV: -0.7 - 0.2 V; 50 mV/s;	O2	0.7	2 - 16	0.05 M PBS pH 7.4, human plasma sample	244
13 CCE (carbon ceramic electrode)/GQD/GOD	CV: -0.8 - 0.2 V; 100 mV/s;	O2	0.00173	0.005 - 1.27	0.1 M PBS pH 7.4, human plasma sample	245
14 GCE/rGO+AgNP/GOD	CV: -0.8 - 0.0 V; 50 mV/s;	O2	0.16	0.5 - 12.5	0.05 M PBS pH 7, urine samples	246
15 GCE/PLL+ERGO/GOD	CV: -0.6 - 0.2 V; 100 mV/s; amperometry @ -0.42 V	O2	n/a	0.25 - 5	0.1 M PBS pH 7	246
16 Au/graphene/GOD/Nafion	CV: -0.7 - 0.1 V; 100 mV/s; amperometry @ -0.495 V	O2	0.04	14-Feb	0.05 M PBS pH 7.4	247
17 GCE/graphene+GOD+Nafion (homogenous suspension)	CV: -0.8 - 0.8 V; 100 mV/s	O2	0.03	0.5 - 14	0.2 M PBS pH 7.4 + 0.1 KCl	248
18 GCE/graphene/GOD	CV: -0.65 - -0.05 V; 10 mV/s	O2	0.01	0.1 - 10	0.1 M PBS pH 6.9, human blood serum	249
19 GCE/RGO+ZnO2/PLL+GOD	CV: -0.8 - 0.1 V; 50 mV/s; DPV: -0.8 - 0.1 V; 50 mV/s	O2	0.13	0.29 - 14	0.05 M PBS pH 7, urine samples	250
20 GCE/rGO/ZnO/GOD	CV: -0.8 - 0.0 V; 50 mV/s	O2	0.02	0.02 - 6.24	0.05 M PBS pH 7	251
21 GCE/ERGO/chitosan+GOD	CV: -0.8 - 0.2 V; 50 mV/s; amperometry @ -0.45 V stirring (?)	O2	0.0017	0.02 - 3.2	0.01 M PBS 7.3	252
22 GCE/mesocellular graphene foam (MGF)+Nafion+GOD	CV: -0.7 - 0.2 V; 90 mV/s (-0.51 V readout)	O2	0.25	1 - 12	0.05 M PBS pH 7.4	254
23 Au/graphene-SH/Au nanocubes/GOD	Amperometry @ -0.4 V	O2	n/a	0.1 - 0.9	0.05 M PBS pH 6.5 + 0.1 M KCl	253
24 GCE/oxidized graphene-CNT (CVD grown)	CV: -0.75 - 0.15 V; 50 mV/s	O2	0.5	2 - 8	0.033 M PBS pH 7 + 0.1 M KCl	254
25 GCE/rGO/Bi nanoribbons/GOD	LSV: -0.6 - 0.2 V; 50 mV/s (read-out -0.46 V)	O2	0.104	0.5 - 6	0.05 M PBS pH 7	219
26 GCE/APTES/rGO/GOD	CV: -0.6 - 0.4 V; 50 mV/s	O2	n/a	0 - 24	0.01 M PBS pH 7.4	255
27 Au/chemically modified graphene/GOD	CV: -0.8 - 0.0 V; 50 mV/s; amperometry @ -0.3 V	O2	0.376	2 - 20	PBS pH 7.4	256
28 GCE/poly(1-vinyl-3-butylimidazolium bromide)+graphene/GOD	CV: -0.7 - 0.1 V; 200 mV/s	O2	0.267	0.8 - 20	0.1 M PBS pH 6.5	257
29 GCE/graphene oxide nanoribbons/iron(III) meso-tetakis(N-methylpyridyl- num-4-yl) porphyrin/GOD	CV: 0.1 - 0.9 V; 100 mV/s (read-out -0.41 V)	O2	0.2	0.5 - 10	0.1 M PBS pH 7.4, serum samples	258
30 GCE/graphene+AuNP/GOD	Amperometry @ -0.2 V; CV: -0.9 - 0.5 V; 50 mV/s	O2	0.0035	0.1 - 10	0.1 M PBS pH 5.5, human serum	259
31 GCE/graphene nanosheets+carbon nanospheres/GOD	CV: -0.7 - 0.3 V in 100 mV/s	O2	0.1	0.4 - 20	0.1 M PBS pH 7, 1:10 diluted blood sample (PBS pH 7.0)	260
32 GCE/rGO-PAMAM-Ag/GOD/chitosan	Amperometry @ -0.25 V	O2	0.0045	0.032 - 1.89	0.1 M PBS pH 7	261
33 GCE/metal coordination polymers supported on graphene nanosheets/GOD	Amperometry @ -0.3 V	O2	0.000005 (5 nM)	2 ranges: 0.00005 (50 nM) - 0.1, 0.1 M PBS pH 7, 1:100 diluted blood (with 0.1 M PBS pH 7)		221
34 GCE/graphene+CNT+ZnO/GOD	DPV: -0.6 - 0.2 V; 50 mV/s	O2	0.0045	0.01 - 6.5	PBS pH 7	262
35 SPCE/graphene+polyaniline+AuNP-GOD/Nafion	DPV: -0.7 - 0.0 V, pulse amplitude 15 mV, width 20 ms	O2	0.1	0.2 - 11.2	0.1 M PBS pH 7	263
36 GCE/rGO+AuNP/GOD/Nafion	CV: -0.65 - 0.0 V; 50 mV/s	O2	0.01	1 - 8	0.1 M PBS pH 7	264
37 GCE/nitrogen doped graphene+PANI+GOD/Nafion	Amperometry @ -0.33 V	O2	0.002	0.005 - 1.1	0.1 M PBS pH 6.0	222
38 GCE/GO-Pt-AuNP/GOD	CV: -0.65 - 0.0 V; 100 mV/s; amperometry @ -0.43 V + stirring	DET (?)	0.3	0.3 - 20	0.05 M PBS pH 7, cell growing medium (glucose uptake measurements)	220

nase. This phenomenon is explained by the following mechanism: the FAD-GDH can transfer the electrons by means of intramolecular charge transfer from the cofactor - FAD *via* iron-sulfur cluster in the catalytic subunit (3Fe-4s) to hemes in the electron transfer subunit and from these directly to the electrode (the exact mechanism is described elsewhere<sup>267</sup>).

Here, a graphene electrode and pyrenebutyric acid as a monolayer for aminocoupling the enzyme, was used. The average thickness of a saturated monolayer formed by using PBA solution was measured to be 0.7 nm and the orientation of the PBA towards the graphene surface is concentration dependent.<sup>37</sup> Since in our experiments we used only 1 mM PBA (non-saturated monolayer), PBA is most probably "lying flat" on graphene, with the pyrene functional group parallel to the graphene surface, whereas in the saturated monolayer case, the PBA would bind at a higher angle close to 90° with respect to the graphene surface. Therefore, the maximum linker length is well below 0.7 nm, which is within the relevant range for DET to occur.

Control measurements with different surfaces were performed: bare graphene (Fig. 4.4 B) and PBA-NHS modified graphene (Fig. 4.5 A) and no oxidation current increase in response to glucose addition was observed. This provides further evidence for non-mediated or direct electron transfer in the studied monolayer system. With respect to electrochemical interferences in the DET pathway, the glucose oxidation currents are lowered when ascorbic acid is added to the solution. At this point, one can only speculate on the exact nature of the interactions between the electrode surface and the ascorbic acid. However, these interfering contributions may be reduced if AA can be excluded from the vicinity of the electrode surface by appropriate surface modification, for example, by adding polyethylene glycol.

Comparing the glucose dependent oxidation currents for the case of MET and DET (Fig. 4.4 *vs.* Fig. 4.11), one can clearly see that the MET currents are substantially higher (5x). This effect can be easily explained by the orientation of GDH on the surface of the electrode. Here, the enzyme's immobilization is random and generally one can distinguish two different types of orientations: 1) when the active center is directed towards the electrode enabling the DET and 2) all other orientations, where DET is suppressed due to long distance. Statistically, one can assume that this preferred DET-enabling orientation is less probable and some of the enzyme molecules are not directly connected to the electrode, but can remain catalytically active when a redox mediator is provided. Therefore, more enzyme molecules contribute to the MET glucose signals than to DET. To increase the DET currents, oriented enzyme immobilization may be envisioned which would require additional enzyme engineering to introduce specific binding sites.<sup>268</sup>

### 4.3 Conclusions

In summary, high-quality large-area CVD grown single-layer graphene was investigated as a working electrode for the enzymatic detection of glucose. The electrode was modified with a monolayer of FAD-dependent glucose dehydrogenase and different paths (direct vs. mediated) of electron transfer were studied. A glucose-dependent increase of oxidation current was measured even in the absence of redox mediators, indicating that direct electron transfer may occur in this monolayer system owing to the short linkers used. To corroborate these results, additional control measurements were performed with bare and with linker modified graphene and no significant glucose dependent signals were recorded. To the best of my knowledge, this is the first time that a direct electron transfer from an oxygen insensitive glucose dehydrogenase to a monolayer graphene electrode surface has been reported. Previous works employed glucose oxidase instead, which is highly sensitive to oxygen, raising concerns about the robustness of DET observations to date as oxygen dependency or impurities may be misinterpreted as DET signals. To reduce the interfering signals, a novel redox mediator was used – a nitrosoaniline derivative (*N,N*-bis(hydroxyethyl)-3-methoxy-4-nitrosoaniline). It is only activated in presence of glucose and interference effects can be easily subtracted. This is the first time a nitrosoaniline derivative was employed as a mediator on a GDH-coated single layer graphene electrode. While the measured DET currents are smaller than those in the mediated cases, the probability of DET may be further increased by site-specific enzyme immobilization. Also, the surface may be passivated by polymers such as polyethylene glycol to exclude ascorbic acid and other electrochemical interferents from the vicinity of the electrode. Overall, the presented monolayer-based DET device may have certain advantages, for example, in continuous glucose monitoring (CGM), where the use of diffusional mediators is prohibited due to toxicity or limited long-term stability. On the other hand, the use of nitrosoaniline is justified in "regular", i.e. single-use, glucose test strips, because it helps to easily eliminate the effects of electrochemical interferences.

## 5 | Conclusions and outlook

*"One never notices what has been done;  
„Człowiek nigdy nie ogląda się na to, co zrobione,*

*one can only see what remains to be done".  
ale na to patrzy, co ma przed sobą do zrobienia".*

— Maria Skłodowska-Curie

This work presented multimodal detection (electrochemical and electronic) of biomolecules with biosensors based on different carbon nanomaterials (carbon nanotubes and graphene). Semiconducting carbon nanotube networks are shown to make good transistors and interestingly, can be ink-jet printed as shown recently by Rother et al.<sup>159</sup> Graphene, on the other hand is still troublesome for mass-manufacturing, yet it seems that it is more susceptible to electrical characteristics change, which can be both advantageous (lower limit-of-detection, higher sensitivity of the biosensor), as well as problematic (more cumbersome analysis of adsorption of species). An attempt of elucidating the biosensing mechanism of GFET was made. For the presented assay, the TSH detection mechanism most likely relies on charge carrier scattering on surface impurities of graphene. For other analytes, it may be different though, therefore careful analysis of the GFET behaviour is needed. The device-to-device variation is lower in case of CNT FET than for GFETs, so more work has to be dedicated to develop reproducible manufacturing processes of GFETs. Both transistor setups presented in Chapter 2 and Chapter 3, significantly reduce the problem of Debye screening in high ionic strength (physiological) buffers through the addition of a PEG layer. It is not excluded though, that there are different polymers to substitute poly(ethylene glycol).

The next steps for the assays presented here will be measurements in more complex media like e.g. blood (Andoy et al. worked with serum<sup>59</sup>). Despite different PEG immobilization methods, the "PEG effect" *i.e.* signal enhancement, with respect to the mono SAM (PBA), was about  $\sim 3$ -fold. More laboratory work as well as theoretical modelling has to be dedicated to understand the mechanisms of PEG-induced signal enhancement.

In this work, either GFP-specific nanobodies or TSH-specific F(ab')<sub>2</sub> was used as model receptors, but in future, one cannot exclude the use of different receptors, including whole antibodies (most probably different PEG lengths and linker-to-PEG ratios would be needed), aptamers or even molecularly imprinted polymers. Additionally, oriented immobilization of receptors on the surface to bring the binding sites closer to the surface of the transducer could be advantageous for generating overall higher analytical signals.

Furthermore, here, pyrene derivatives were used as linkers for both receptor immobilization and PEG functionalization. Other, non-pyrene linkers based on  $\pi$ - $\pi$  stacking could be used to enhance the density of the monolayers on the surface of graphene or carbon nanotubes.

Interestingly, a comparison of different processes of graphene FET manufacturing could be made. Reduced graphene oxide platelets network, non-PMMA based transfer of CVD graphene (e.g. with paraffin shown to be result in less residues on the surface of graphene) could be compared. Moreover, a "flip-over" transfer of CVD graphene can be assessed, where as CVD grown graphene on copper foil is flipped over and attached to the substrate surface (e.g. with a polymer) and then the copper layer is etched away leaving a clean, non-polymer polluted graphene surface.

Interestingly, it was demonstrated that the exactly same graphene electrode/transistor setup can be employed in electrochemical biosensing (as a working electrode) and in electronic (as an electrolyte-gated field-effect transistor's channel). Future studies will focus on detection of the same analyte with those two different techniques with the hope that the analytical parameters (dynamic range, lower limit of detection, sensitivity) of the multimodal approach will be enhanced.

It was also recently shown that semiconducting carbon nanotubes can be advantageous for facilitating direct electron transfer from glucose dehydrogenase.<sup>269</sup> A setup used in Chapter 2 can be beneficial for making a DET-based electrochemical biosensor due to high surface area and the three dimensional structure of the nanotube network.

Additionally, one could envision the use of graphene and/or carbon nanotube FET based transducer for creating a platform (in e.g. 96 well plate format) and immobilize the target of interest at the surface of carbon nanomaterial based FETs in order to screen synthetic libraries of nanobodies to select the nanobodies with the highest binding affinities.

As an interesting alternative, multiparameter analysis of a single liquid sample could be also taken into consideration. By mass production of multielectrode/multichannel chips and controlled surface modification (either by means of selective (electro)chemistry, spotting of the biologicals/chemicals or simply by introducing a physical barrier between devices on one chip), one could construct a biosensor platform that is able to monitor more than one quasi-specific analyte (parameter) at a time to make the biosensors output specific. This would help to diagnose complex diseases like e.g. sepsis, where different biomarkers are involved, but there is so far no single specific biomarker to diagnose it.

Obviously, if glucose sensing with glucose dehydrogenase was possible, other enzymes for crucial metabolites could be employed (e.g. lactate).

Finally, from the materials science point-of-view, it would be interesting to test a device (working electrode, EGFET channel) comprising of both carbon nanotubes and graphene combined as means for higher surface area, which could benefit both readout methods.

## 6 | Materials and methods

### 6.1 Single-walled carbon nanotube network field-effect transistor for immunodetection in physiological conditions

Methods described here refer to the study described in the Chapter 2.

#### 6.1.1 Preparation of SWCNT dispersions.

SWCNT purification was carried out by Marcel Rother (Uni Heidelberg).

Plasma torch SWCNTs (RN-220, 0.9 - 1.9 nm of diameter, 0.3 – 4  $\mu\text{m}$  of length, SWCNT content 60 - 70%, 70% semiconducting SWCNTs, produced by NanoIntegris, Inc.) are added to 2 mg/mL toluene solution of PF12 (poly(9,9-di-n-dodecyl-fluorenyl-2,7-diyl)) to achieve 1.5 mg/mL RN-220 content and bath sonicated for 90 minutes. Next, the dispersion is centrifuged for 45 mins at 60 000 g to remove undispersed material. The supernatant is collected and centrifuged again at 268 000 g for 60 minutes to remove SWCNTs bundles. The supernatant is transferred to a fresh centrifuge tube and centrifuged at 268 000 g for 16 h to remove excess polymer. After the solvent is removed, the formed pellet was washed with THF and stored dry until redispersed in pure toluene again just before the alignment step.

#### 6.1.2 FET fabrication

FET fabrication was performed by Marcel Rother (Uni Heidelberg).

Interdigitated bottom electrodes (channel width 2 mm, channel length 20  $\mu\text{m}$ ) are patterned by means of photolithography using double layer photoresist (MicroChem LOR5B and Microposit S1813) and evaporated with an electron-beam evaporator (Ti/Au thickness 2+30 nm). After that, 1 mL of the redispersed SWCNTs is placed on top of the electrodes and an AC voltage is applied (80 V, 0.1 Hz). Substrates are then washed with THF to remove residual polymer. Atomic force microscopy (tapping mode, Bruker Dimension Icon) is used to determine the average SWNT density: 5-6  $\mu\text{m}^{-1}$ . Gold contacts are passivated in another photolithography step using SU-8 2005 (diluted 1:1 with cyclopentanone resulting in a thickness of approx. 1  $\mu\text{m}$ ) to reduce leakage current.

### 6.1.3 Liquid handling

The liquid cell is made from a polydimethylsiloxane (PDMS, Dow Chemicals) slab, cast from a CNC milled Teflon mold with defined microfluidic channels. Inlet and outlet PTFE tubing is introduced as well as a Ag/AgCl reference electrode (DRIFEF-2, World Precision Instruments). The liquid cell is aligned on the chip and pressed down with a cover. Liquids are introduced into the channel using a Harvard PhD Ultra syringe pump in withdrawal mode (25  $\mu$ L/min, if not stated otherwise).

### 6.1.4 Expression of receptor and analyte molecules

Expression of receptor and analyte molecules was performed by Christopher Bachran (BioMed X GmbH).

VHH GFP enhancer (a camelid heavy chain VHH fragment specific to green fluorescent protein and additionally enhancing its fluorescence),<sup>156</sup> enhanced GFP (eGFP) and tobacco etch virus protease (TEV) are expressed recombinantly in *E. coli*. VHH GFP enhancer gene in plasmid pHEN (kindly provided by H. Ploegh, Whitehead Institute, MIT, USA) is transformed into *E. coli* strain WK6 for expression. eGFP is cloned into plasmid pET19b (Novagen) using NcoI and EcoRI sites. TEV (maltose binding protein fusion to TEV containing a S219V point mutation, MBP-TEV S219V, kindly provided by D. Waugh via Addgene, plasmid reference RK793) and eGFP plasmids are transformed into *E. coli* strain Rosetta (DE3) pLysS (Novagen). For all three proteins, protein expression is induced by 1 mM Isopropyl- $\beta$ -D-thiogalactoside at an OD 600 nm of 0.8-1 for 3 h at 37 °C in a shaker. Cultures are centrifuged (4000  $\times$  g, 15 min, 4 °C), resuspended in phosphate-buffered saline (PBS) and sonicated (2  $\times$  1 min at 100 % intensity and 0.5 second duty cycle on a Sonopuls HD2070 (Bandelin) equipped with a MS 73 microtip). Samples are centrifuged (4000  $\times$  g, 15 min, 4 °C), supernatants applied to Ni-NTA Agarose-loaded columns (Macherey & Nagel), washed by 20 and 50 mM imidazole in PBS before elution in 250 mM imidazole in PBS. Eluted samples are concentrated in Amicon centrifugal filter devices with 3 kDa and 10 kDa cut-off for VHH GFP enh and eGFP / TEV, respectively (Millipore). Concentrates are dialyzed over night against PBS before concentrations were determined by A 280 nm measurements.

### 6.1.5 Surface functionalization

An ethanol solution of 1 mM 1-pyrenebutyric acid (PBA, Sigma-Aldrich) and 0.25 mM mPEG-pyrene (molecular weight = 10 kDa, Creative PEGWorks) to achieve heterogeneous SAM (“mixed SAM”) or just 1 mM PBA to get homogeneous SAM (“mono SAM”), is continuously introduced into the microfluidic channel for 1 h. After that, the channel is briefly washed with ethanol and deionized water and then kept in 100 mM Tris buffer pH 7.4 (Carl Roth). Then, after a brief flush with deionized water, 100 mM N-hydroxysuccinimide (NHS) and 1-ethyl-3-(3-dimethylaminopropyl) carbodiimide (EDC, both Sigma-Aldrich) aqueous solution is pumped into the channel for 20 minutes to activate the surface. After that, either a 10  $\mu$ M GFP-specific nanobody VHH or 10  $\mu$ M bovine serum albumin (BSA, Carl Roth), in 0.2 M phosphate buffer (pH 7) is introduced for 1 h for specific and non-specific adsorption experiments, respectively. Finally, in case

of optimized SWCNT FET based GFP sensing assay, the surface is blocked with BSA (Carl Roth).

### 6.1.6 Measurement setup

A microfluidic PDMS channel with PTFE tubing is used to provide the solutions to the transducer. A bulk Ag/AgCl reference electrode is inserted in the middle of the microfluidic channel to control the gate potential. Typical current-voltage curves can be seen in Fig. 2.1 C. A constant bias voltage  $V_{SD} = 100$  mV is applied between the source and drain gold electrodes and the gate voltage  $V_{Ag/AgCl}$  is swept from -750 mV to 750 mV. The measurements are repeated three times, if not stated otherwise. All FET measurements are recorded using a dual-channel source meter (Keithley 2636 B) in Tris buffers at ambient temperature of  $21 \pm 2^\circ\text{C}$ . All measurements are performed after 30 minutes initial stabilization time.

### 6.1.7 QCM study

A quartz crystal microbalance system (Q-Sense E4, Biolin Scientific AB, Stockholm, Sweden) is used to test the immobilization protocol for VHH nanobodies and to measure the binding of the green fluorescent protein (GFP). Prior to immobilization, the gold-coated QCM chips are first cleaned in UV/ozone for 10 min and hot base piranha (= 5:1:1 mixture of ammonia :  $\text{H}_2\text{O}_2$  : water) at  $75^\circ\text{C}$  for 5 min, rinsed with deionized water, dried with nitrogen and cleaned in UV/ozone again for 10 min. After cleaning, the chips are immersed in a 1 mM 6-mercaptopentanoic acid solution in a 3:1 ethanol : water mixture at  $37^\circ\text{C}$  overnight to assemble a monolayer with functional COOH groups. After rinsing with ethanol and water and drying with nitrogen, the QCM chambers are assembled and the chips primed with buffer (10 mM, pH 7.4) to reach a stable baseline, continuously monitored by QCM. The surface is then activated with 100 mM EDC and 100 mM NHS in  $\text{H}_2\text{O}$  for 20 min, followed by a short rinsing in buffer (1 min) and incubation in anti-GFP VHH antibody solution in buffer for 30 min. Then, the surface is rinsed with buffer again to remove unbound VHH, and is subsequently incubated in 100 nM GFP solution.

## 6.2 TSH immunosensing with single-sheet graphene field-effect transistor

Methods described here refer to the study described in the Chapter 3.

### 6.2.1 Materials

CVD-grown graphene (Trivial Transfer Graphene; lateral size  $5\text{ cm} \times 5\text{ cm}$ ) is purchased from ACS Material (Pasadena, CA). The  $\text{F(ab}')_2$  fragment of an anti-TSH antibody and the recombinant TSH antigen are kindly provided by Roche Diagnostics GmbH (Penzberg, Germany). PDMS (SYLGARD-184) for flow chamber fabrication was from Dow Corning (Midland, MI). Polyethylene glycol (mPEG-SH,  $M_w = 10$  kDa) is from Nanocs, Inc. (Boston, MA) and the linker PEG (SH-PEG-COOH,  $M_w = 460$  Da)

from Celares GmbH (Berlin, Germany). PBA, PyMal, and horse serum are from Sigma-Aldrich (Steinheim, Germany). 1-Ethyl-3-(3-dimethylaminopropyl)carbodiimide (EDC), *N*-hydroxysuccinimide (NHS) and all the other chemicals are from Carl Roth (Karlsruhe, Germany) unless otherwise stated.

### 6.2.2 Fabrication of substrate and gold contacts

Glass slides (25 × 25 mm) are first sonicated with acetone, isopropanol, and deionized water for 15 min. After drying in N<sub>2</sub> they were then oxygen plasma cleaned for 5 min. After that, titanium (10 nm) and gold (100 nm) are thermally evaporated using a shadow mask to achieve desired pattern (Fig. ??). The resulting glass substrate is then kept dry at room temperature until use. Immediately prior to graphene transfer, the glass substrate is first cleaned by sonication in deionized water for 10 min then N<sub>2</sub> dried. Afterward, base piranha (1:1:5 of NH<sub>4</sub>OH:H<sub>2</sub>O<sub>2</sub>:H<sub>2</sub>O volume ratio) cleaning is done for 20 min at 80 °C. After thorough rinsing with deionized water and drying with N<sub>2</sub>, the glass substrate is then treated further with O<sub>2</sub> plasma for 5 min then kept in water, ready for graphene transfer.

### 6.2.3 Graphene transfer and flow chamber assembly

The PMMA-coated single-layer graphene sheet is transferred following instructions from ACS Material. The graphene is manually cut and transferred between the empty space of two gold electrodes (~3 × 3 mm). The excess water is air dried for at least 30 min, making sure graphene dries on top of the gold contacts. The air-dried slides are then baked on the hot plate at 120 °C for 20 min. To remove the PMMA layer, the glass slides are washed with acetone for 24 h using a Soxhlet extractor. With this method, the samples are always flushed with a freshly condensed acetone making the cleaning more effective. After acetone cleaning, they are baked on the hot plate at 120 °C for 20 min to remove residual organic solvents. Each chip containing two graphene devices is then used or stored at room temperature until further use (Fig. ?? C). The flow chamber is then assembled by placing the PDMS chamber and sealing with the printed circuit board (PCB) for connection with the source and drain contacts. Polytetrafluoroethylene (PTFE) tubing is used to flow solution in and out of the chamber using a syringe pump (Harvard Apparatus, Holliston, MA), ensuring a rapid exchange of liquids within the active channel.

### 6.2.4 Surface functionalization and TSH detection

After the flow cell is assembled the bare graphene surface is washed with dry ethanol for 10 min. The surface is then modified with pyrene-based compounds to anchor both the F(ab')<sub>2</sub> receptor and PEG to the surface of graphene. First, 1 mM PBA + 0.1 mM PyMal in dry ethanol is flowed into the chamber and incubated for 60 min to functionalize the graphene surface with 10:1 PBA:PyMal. After incubation, the unbound pyrene is washed with dry ethanol for 10 min at 100 L/min. The solution within the chamber is then exchanged to aqueous for PEG immobilization by flushing with water then PBS (150 mM NaCl + 50 mM phosphate buffer pH 7), for 1 min each. 200 M solution of thiolated-mPEG (SH-mPEG, M<sub>w</sub> = 10 kDa) in PBS is then added to immobilize PEG polymer on

maleimide-functionalized pyrene. The PEG solution is incubated for 2 h before washing with PBS. The PBA is then activated with 100 mM EDC + 100 mM NHS for 20 min before 0.3 mg/mL F(ab')<sub>2</sub> is added to the chamber. F(ab')<sub>2</sub> solution is then incubated overnight at 4 °C then washed with PBS to remove non-immobilized F(ab')<sub>2</sub>.

### 6.2.5 Measurement setup

FET characterization is performed before and after addition of increasing concentration of TSH both in 50 mM phosphate buffer pH 8 + 150 mM NaCl. Electrical measurements are performed using a dual-channel source meter (Keithley 2636B) at a constant source-drain voltage  $V_{sd} = 100$  mV the gate potential  $V_g$  is swept typically from -0.5 to 0.5 V. An Ag/AgCl reference electrode (WPI, Dri-REF, customized length) is placed near the sensor surface (through the PDMS chamber) to control the gate potential.

## 6.3 Observation of direct electron transfer from glucose dehydrogenase to graphene

Methods described here refer to the study described in the Chapter 4.

### 6.3.1 Single-sheet graphene electrodes

Glass substrates (25 x 25 x 1.1 mm, Borofloat 33) are bought from Schott, Germany and thoroughly sonicated for 15 minutes in acetone, isopropanol (Carl Roth, Germany) and deionized water, subsequently. After drying with N<sub>2</sub> stream, they are put into O<sub>2</sub> plasma cleaner for 10 minutes. Next, a metal shadow mask was used to evaporate a pattern of 10 nm titanium and 100 nm gold. After hydrophilizing the surface with another 5-minute plasma treatment, Trivial Transfer Graphene pieces from ACS Material, LLC (USA) are "fished" from the surface of water onto the glass substrates. The graphene with PMMA on top is left to air dry and then baked on a hot plate for 20 minutes in 80 °C. To remove the PMMA, the samples are put into Soxhlet apparatus overnight, which enabled cycled rinsing with freshly distilled acetone. Next, the samples are rinsed with isopropanol and baked for 20 minutes in 80 °C to evaporate leftover solvents.

### 6.3.2 Liquid handling

The liquid cell is made from polydimethylsiloxane (PDMS, Dow Chemicals) slab, casted out of Teflon mold with defined microfluidic channels. Inlet and outlet PTFE tubing and Ag/AgCl reference electrode (DRIREF-2, World Precision Instruments) are inserted into PDMS slab. The liquid cell is aligned on the chip in a way the contact electrodes for graphene are outside the fluidic channel and pressed with a cover. The liquids are introduced into the channel using a Harvard PhD Ultra syringe pump.

### 6.3.3 Surface functionalization

An ethanol solution of 1 mM 1-pyrenebutyric succinimide acid (PBA-NHS, Sigma-Aldrich) is introduced into the microfluidic channel for 1 h. After that, the microfluidic channel

is briefly washed with ethanol, deionized water and PBS buffer (150 mM NaCl + 50 mM Na<sub>2</sub>HPO<sub>4</sub>, pH 7.4, Carl Roth). After that, 1 mg/mL of FAD-dependent GDH (BBI Solutions, UK) in PBS (pH 7.4) is introduced for 1 h.

### 6.3.4 Measurement setup

A microfluidic PDMS channel with PTFE tubing is used to provide the solutions to the electrochemical setup. A CVD-grown single layer graphene is used as a working electrode, Ag/AgCl as reference electrode and a planar on-chip gold electrode is used as a counter electrode. In well setup experiments, a PDMS slab with a through hole is placed on the glass chip forming an open well, where bulk RE and a Pt wire are placed. The geometric surface area of exposed graphene is estimated to be 2.44 mm<sup>2</sup> and the currents are recalculated to current density using this value. The electrochemically active surface area is estimated to be  $\sim 2.00$  mm<sup>2</sup> (see Subsection 4.2.2 4.9). Cyclic voltammetry experiments were typically performed from 0.0 to 0.5 V with 10 mV/s scan rate. For chronoamperometry measurements, 0.3 V is applied continuously and currents for the background (600 s) and upon glucose stock solution recorded (for 300 seconds each). All the measurements are recorded using an Ivium-n-Stat multichannel potentiostat (Ivium Technologies) in PBS pH 7.4 at ambient temperature of  $21 \pm 2$  °C.

# List of Figures

1.1	Scheme of a biosensor. . . . .	3
1.2	Schematic representation of the main components and mode of action of a immunosensor. . . . .	4
1.3	Schematic representation of different antibody formats . . . . .	5
1.4	Michaelis-Menten kinetics . . . . .	8
1.5	Chemical formulas of pyrene and its derivatives used in this work. . . . .	9
1.6	Carboxyl-to-amine crosslinking using the carbodiimide EDC and NHS and maleimide-thiol crosslinking. . . . .	10
1.7	Homogeneous and heterogeneous reduction of ferrocenium ion . . . . .	11
1.8	Cyclic voltammetry basics . . . . .	13
1.9	Chronoamperometry: waveform of potential step and chronoamperometric response . . . . .	14
1.10	MOSFET scheme and transfer curves. . . . .	16
1.11	Schematic representations of EDL structures . . . . .	18
1.12	Debye length with relation to the surface potential . . . . .	21
1.13	Illustration of Debye screening limitation in FET-based (bio)sensors. . . . .	22
1.14	Comparison of a classical FET with electrolyte-gated FET . . . . .	23
1.15	Mechanisms of biosensing with carbon nanotube/graphene electrolyte gated transistors . . . . .	25
1.16	Typical Raman spectra of graphene and carbon nanotubes . . . . .	27
1.17	Literature trends for different carbon nanomaterials . . . . .	29
1.18	Bravais lattice of graphene. . . . .	30
1.19	Graphene electronic structure. . . . .	31
1.20	Atomic structure of carbon nanotubes. . . . .	33
1.21	Comparison between transfer curves of GFET and CNTFET devices . . . . .	36
2.1	CNT-FET measurement setup, typical transfer curves and surface characterization . . . . .	40
2.2	Surface functionalization. Transfer curves of bare and PBA+PEG coated CNT-FET . . . . .	41
2.3	Immobilization of VHH on PBA only and PBA+PEG coated SWCNTs. . . . .	42
2.4	Immobilization of VHH on 6-mercaptophexanoic acid functionalized gold-coated QCM chips. . . . .	43
2.5	MixSAM vs. monoSAM - GFP immunosensing with VHH on differently functionalized CNT-FET . . . . .	45
2.6	Non-specific adsorption experiments in 100 mM buffer with pH 7.4 . . . . .	46

2.7	Optimized SWCNT FET-based assay for GFP detection. . . . .	47
2.8	Long-term stability measurements. . . . .	48
3.1	Graphene FET measurement setup, a real photo of the chip, Raman spectra and a graph showing reproducibility of CNP of GFETs . . . . .	55
3.2	Surface modification of graphene based FET for TSH immunodetection . . . . .	56
3.3	Electrical characterization of surface modification of graphene based FET for TSH immunodetection . . . . .	57
3.4	TSH detection in buffer with GFET . . . . .	58
3.5	Transfer curves of GFET devices before and after TSH addition on control surfaces . . . . .	59
3.6	Relative change in minimum conductance with increasing TSH concentration for different surfaces . . . . .	60
3.7	GFET electronic response towards non-specific detection of BSA and TSH at pH 8 and pH 4. . . . .	62
3.8	Drain current <i>vs.</i> gate current (leakage) of a typical GFET device . . . . .	63
4.1	Setup scheme and electrochemical reactions taking place in the studied system. . . . .	69
4.2	Surface functionalization and enzyme immobilization scheme with Raman spectroscopy characterization . . . . .	70
4.3	Raman characterization of GDH modification of graphene. . . . .	71
4.4	Direct electron transfer from GDH to graphene . . . . .	72
4.5	DET control experiment of PBA-NHS modified graphene electrode . . . . .	73
4.6	Chronoamperometry of GDH on graphene electrode (DET) . . . . .	74
4.7	Ferrocenemethanol as a conventional redox mediator in glucose biosensors. . . . .	75
4.8	Catalytic behavior of ferrocenemethanol towards ascorbic acid oxidation. . . . .	76
4.9	Cyclic voltammogram of bare graphene electrode with different glucose concentration with ferrocenemethanol added. . . . .	76
4.10	Nitrosoaniline electrochemistry on graphene. . . . .	77
4.11	Nitrosoaniline as a redox mediator in glucose biosensors. . . . .	78

# Bibliography

- [1] Clark, L. C.; Lyons, C. *Annals of the New York Academy of Sciences* **1962**, *102*, 29–45.
- [2] Yalow, R. S.; Berson, S. A. *Journal of Clinical Investigation* **1960**, *39*, 1157–1175.
- [3] Iijima, S. *Nature* **1991**, *354*, 56–58.
- [4] Novoselov, K. S. *Science* **2004**, *306*, 666–669.
- [5] Gao, N.; Zhou, W.; Jiang, X.; Hong, G.; Fu, T. M.; Lieber, C. M. *Nano Letters* **2015**, *15*, 2143–2148.
- [6] Gao, N.; Gao, T.; Yang, X.; Dai, X.; Zhou, W.; Zhang, A.; Lieber, C. M. *Proceedings of the National Academy of Sciences* **2016**, *113*, 14633–14638.
- [7] Gutiérrez-Sanz, Ó.; Andoy, N. M.; Filipiak, M. S.; Hausteim, N.; Tarasov, A. *ACS Sensors* **2017**, *2*, 1278–1286.
- [8] Charles, P. T.; Stubbs, V. R.; Soto, C. M.; Martin, B. D.; White, B. J.; Taitt, C. R. *Sensors* **2009**, *9*, 645–655.
- [9] Liu, J.; Bibari, O.; Mailley, P.; Dijon, J.; Rouvière, E.; Sauter-Starace, F.; Caillat, P.; Vinet, F.; Marchand, G. *New Journal of Chemistry* **2009**, *33*, 1017–1024.
- [10] Monošík, R.; Stredánský, M.; Šturdík, E. *Acta Chimica Slovaca* **2012**, *5*, 109–120.
- [11] Lin, J.; Ju, H. *Biosensors and Bioelectronics* **2005**, *20*, 1461–1470.
- [12] Wang, W.; Singh, S.; Zeng, D. L.; King, K.; Nema, S. *Journal of Pharmaceutical Sciences* **2007**, *96*, 1–26.
- [13] Holliger, P.; Hudson, P. J. *Nature Biotechnology* **2005**, *23*, 1126–1136.
- [14] Kubala, M. H.; Kovtun, O.; Alexandrov, K.; Collins, B. M. *Protein Science* **2010**, *19*, 2389–2401.
- [15] Muyldermans, S. *Annual Review of Biochemistry* **2013**, *82*, 775–797.
- [16] De Meyer, T.; Muyldermans, S.; Depicker, A. *Trends in Biotechnology* **2014**, *32*, 263–270.

- [17] Mi, L.; Wang, P.; Yan, J.; Qian, J.; Lu, J.; Yu, J.; Wang, Y.; Liu, H.; Zhu, M.; Wan, Y.; Liu, S. *Analytica Chimica Acta* **2016**, *902*, 107–114.
- [18] Li, H.; Mu, Y.; Yan, J.; Cui, D.; Ou, W.; Wan, Y.; Liu, S. *Analytical Chemistry* **2015**, *87*, 2007–2015.
- [19] Zhou, Q.; Li, G.; Zhang, Y.; Zhu, M.; Wan, Y.; Shen, Y. *Analytical Chemistry* **2016**, *88*, 9830–9836.
- [20] Wang, H.; Li, G.; Zhang, Y.; Zhu, M.; Ma, H.; Du, B.; Wei, Q.; Wan, Y. *Analytical Chemistry* **2015**, *87*, 11209–11214.
- [21] *Enzyme Kinetics*; Wiley-VCH Verlag GmbH & Co. KGaA: Weinheim, Germany, 2008; pp 7–58.
- [22] Filipiak, M. S.; Vetter, D.; Thodkar, K.; Gutiérrez-Sanz, O.; Jönsson-Niedziółka, M.; Tarasov, A. *Electrochimica Acta (to be submitted)* **2018**,
- [23] Celebanska, A.; Jedraszko, J.; Lesniewski, A.; Jubete, E.; Opallo, M. *Electroanalysis* **2018**, *30*, 2731–2737.
- [24] Tabata, M.; Koushima, F.; Totani, M. *Analytica Chimica Acta* **1994**, *298*, 113–119.
- [25] Ferri, S.; Kojima, K.; Sode, K. *Journal of Diabetes Science and Technology* **2011**, *5*, 1068–1076.
- [26] Bardea, A.; Katz, E.; Bückmann, A. F.; Willner, I. *Journal of the American Chemical Society* **1997**, *119*, 9114–9119.
- [27] Stryer, *Biochemistry*; W. H. Freeman, 2002.
- [28] Bairoch, A. ENZYME - enzyme nomenclature database. <https://enzyme.expasy.org>.
- [29] 1978, U. o. E. A. R. *European Journal of Biochemistry* **1979**, *97*, 319–320.
- [30] Johnson, K. A.; Goody, R. S. *Biochemistry* **2011**, *50*, 8264–8269.
- [31] BBI Solutions, FAD-GDH - reduced xylose interference. [https://www.bbisolutions.com/pub/media/wysiwyg/technical\\_{\\_}support/enzymes/FAD-GDH-{-}-reduced-xylose-interference-Product-Information-Sheet.pdf](https://www.bbisolutions.com/pub/media/wysiwyg/technical_{_}support/enzymes/FAD-GDH-{-}-reduced-xylose-interference-Product-Information-Sheet.pdf).
- [32] Toyobo USA Inc., Lactate oxidase information website. <http://www.toyobousa.com/enzyme-LCO-301.html>.
- [33] Pundir, C. S.; Narwal, V.; Batra, B. *Biosensors and Bioelectronics* **2016**, *86*, 777–790.
- [34] Gomes, A. R.; Rocha-Santos, T. A. *Reference Module in Chemistry, Molecular Sciences and Chemical Engineering*, 3rd ed.; Elsevier, 2018; pp 1–7.

- [35] Sassolas, A.; Blum, L. J.; Leca-Bouvier, B. D. *Biotechnology Advances* **2012**, *30*, 489–511.
- [36] Snyder, R. G. *Journal of Molecular Spectroscopy* **1961**, *7*, 116–144.
- [37] Hinnemo, M.; Zhao, J.; Ahlberg, P.; Hägglund, C.; Djurberg, V.; Scheicher, R. H.; Zhang, S. L.; Zhang, Z. B. *Langmuir* **2017**, *33*, 3588–3593.
- [38] Nakajima, N.; Ikada, Y. *Bioconjugate Chemistry* **1995**, *6*, 123–130.
- [39] Hermanson, G. T. In *Bioconjugate Techniques*, third edit ed.; Hermanson, G. T., Ed.; Elsevier: Boston, 2013; pp 259–273.
- [40] ThermoFisher Scientific, Carbodiimide crosslinker chemistry. <https://www.thermofisher.com/pl/en/home/life-science/protein-biology/protein-biology-learning-center/protein-biology-resource-library/pierce-protein-methods/carbodiimide-crosslinker-chemistry.html>.
- [41] Elgrishi, N.; Rountree, K. J.; McCarthy, B. D.; Rountree, E. S.; Eisenhart, T. T.; Dempsey, J. L. *Journal of Chemical Education* **2018**, *95*, 197–206.
- [42] Compton, R. G.; Laborda, E.; Ward, K. R. *Understanding Voltammetry*; World Scientific, 2014.
- [43] Bard, A. J.; Inzelt, G.; Scholz, F. *Electrochemical Dictionary*; Springer-Verlag: Berlin, 2008.
- [44] Scholz, F. In *Electroanalytical Methods: Guide to Experiments and Applications*; Scholz, F., Bond, A., Compton, R., Fiedler, D., Inzelt, G., Kahlert, H., Komorsky-Lovrić, Š., Lohse, H., Lovrić, M., Marken, F., Neudeck, A., Retter, U., Scholz, F., Stojek, Z., Eds.; Springer Berlin Heidelberg: Berlin, Heidelberg, 2010; Vol. 1; pp 1–359.
- [45] Cottrell, F. G. *Zeitschrift für Physikalische Chemie* **1903**, *42U*, 385–431.
- [46] Syu, Y.-C.; Hsu, W.-E.; Lin, C.-T. *ECS Journal of Solid State Science and Technology* **2018**, *7*, Q3196–Q3207.
- [47] Helmholtz, H. *Annalen der Physik und Chemie* **1853**, *165*, 211–233.
- [48] Burt, R.; Birkett, G.; Zhao, X. S. *Physical Chemistry Chemical Physics* **2014**, *16*, 6519–6538.
- [49] Butt, H.-J. *Physics and Chemistry of Interfaces*; Wiley-VCH Verlag GmbH & Co. KGaA: Weinheim, FRG, 2003; pp 42–56.
- [50] Robins, M.; Fillery-Travis, A. *Journal of Chemical Technology & Biotechnology* **2007**, *54*, 201–202.
- [51] Debye, P. *Transactions of The Electrochemical Society* **1942**, *82*, 265.

- [52] Maehashi, K.; Katsura, T.; Kerman, K.; Takamura, Y.; Matsumoto, K.; Tamiya, E. *Analytical Chemistry* **2007**, *79*, 782–787.
- [53] Pacios, M.; Martin-Fernandez, I.; Borrisé, X.; Del Valle, M.; Bartrolí, J.; Lora-Tamayo, E.; Godignon, P.; Pérez-Murano, F.; Esplandiu, M. J. *Nanoscale* **2012**, *4*, 5917–5923.
- [54] Kim, J. P.; Lee, B. Y.; Hong, S.; Sim, S. J. *Analytical Biochemistry* **2008**, *381*, 193–198.
- [55] Kulkarni, G. S.; Zhong, Z. *Nano Letters* **2012**, *12*, 719–723.
- [56] Ohshima, H. *Science and Technology of Advanced Materials* **2009**, *10*, 063001.
- [57] Melzer, K.; Brändlein, M.; Popescu, B.; Popescu, D.; Lugli, P.; Scarpa, G. *Faraday Discuss.* **2014**, *174*, 399–411.
- [58] Heller, I.; Janssens, A. M.; Männik, J.; Minot, E. D.; Lemay, S. G.; Dekker, C. *Nano Letters* **2008**, *8*, 591–595.
- [59] Andoy, N. M.; Filipiak, M. S.; Vetter, D.; Gutiérrez-Sanz, Ó.; Tarasov, A. *Advanced Materials Technologies* **2018**, *1800186*, 1–12.
- [60] Filipiak, M. S.; Rother, M.; Andoy, N. M.; Knudsen, A. C.; Grimm, S.; Bachran, C.; Swee, L. K.; Zaumseil, J.; Tarasov, A. *Sensors and Actuators, B: Chemical* **2018**, *255*, 1507–1516.
- [61] Rosenblatt, S.; Yaish, Y.; Park, J.; Gore, J.; Sazonova, V.; McEuen, P. L. *Nano Letters* **2002**, *2*, 869–872.
- [62] Allen, B. L.; Kichambare, P. D.; Star, A. *Advanced Materials* **2007**, *19*, 1439–1451.
- [63] Boussaad, S.; Tao, N. J.; Zhang, R.; Hopson, T.; Nagahara, L. A. *Chemical Communications* **2003**, 1502.
- [64] Artyukhin, A. B.; Stadermann, M.; Friddle, R. W.; Stroeve, P.; Bakajin, O.; Noy, A. *Nano Letters* **2006**, *6*, 2080–2085.
- [65] Gui, E. L.; Li, L.-J.; Zhang, K.; Xu, Y.; Dong, X.; Ho, X.; Lee, P. S.; Kasim, J.; Shen, Z. X.; Rogers, J. A.; Mhaisalkar, *Journal of the American Chemical Society* **2007**, *129*, 14427–14432.
- [66] Hecht, D. S.; Ramirez, R. J. a.; Briman, M.; Artukovic, E.; Chichak, K. S.; Stoddart, J. F.; Grüner, G. *Nano Letters* **2006**, *6*, 2031–2036.
- [67] Maroto, A.; Balasubramanian, K.; Burghard, M.; Kern, K. *ChemPhysChem* **2007**, *8*, 220–223.
- [68] Chen, R. J.; Choi, H. C.; Bangsaruntip, S.; Yenilmez, E.; Tang, X.; Wang, Q.; Chang, Y. L.; Dai, H. *Journal of the American Chemical Society* **2004**, *126*, 1563–1568.

- [69] Chen, F.; Qing, Q.; Xia, J.; Tao, N. *Chemistry - An Asian Journal* **2010**, *5*, 2144–2153.
- [70] Chen, J.-H.; Jang, C.; Adam, S.; Fuhrer, M. S.; Williams, E. D.; Ishigami, M. *Nature Physics* **2008**, *4*, 377–381.
- [71] Heller, I.; Kong, J.; Williams, K. A.; Dekker, C.; Lemay, S. G. *Journal of the American Chemical Society* **2006**, *128*, 7353–7359.
- [72] Dresselhaus, M.; Dresselhaus, G.; Saito, R.; Jorio, A. *Physics Reports* **2005**, *409*, 47–99.
- [73] Malard, L.; Pimenta, M.; Dresselhaus, G.; Dresselhaus, M. *Physics Reports* **2009**, *473*, 51–87.
- [74] Ferrari, A. C.; Basko, D. M. *Nature Nanotechnology* **2013**, *8*, 235–246.
- [75] Jorio, A.; Kauppinen, E.; Hassanien, A. *Carbon-Nanotube Metrology*; 2007; Vol. 100; pp 63–100.
- [76] King, W. H. *Analytical Chemistry* **1964**, *36*, 1735–1739.
- [77] Sauerbrey, G. *Zeitschrift für Physik* **1959**, *155*, 206–222.
- [78] Rodahl, M.; Höök, F.; Fredriksson, C.; Keller, C. A.; Krozer, A.; Brzezinski, P.; Voinova, M.; Kasemo, B. *Faraday Discussions* **1997**, *107*, 229–246.
- [79] Voinova, M.; Jonson, M.; Kasemo, B. *Biosensors and Bioelectronics* **2002**, *17*, 835–841.
- [80] Nomura, T.; Okuhara, M. *Analytica Chimica Acta* **1982**, *142*, 281–284.
- [81] Buttry, D. A.; Ward, M. D. *Chemical Reviews* **1992**, *92*, 1355–1379.
- [82] Castro Neto, A. H.; Guinea, F.; Peres, N. M. R.; Novoselov, K. S.; Geim, A. K. *Reviews of Modern Physics* **2009**, *81*, 109–162.
- [83] Syedmoradi, L.; Daneshpour, M.; Alvandipour, M.; Gomez, F. A.; Hajghassem, H.; Omidfar, K. *Biosensors and Bioelectronics* **2017**, *87*, 373–387.
- [84] Geim, A. K.; Novoselov, K. S. *Nature Materials* **2007**, *6*, 183–191.
- [85] Yang, G.; Huang, Z.; Gao, C.-F.; Zhang, B. *AIP Advances* **2016**, *6*, 055115.
- [86] Avouris, P. *Nano Letters* **2010**, *10*, 4285–4294.
- [87] Bolotin, K.; Sikes, K.; Jiang, Z.; Klima, M.; Fudenberg, G.; Hone, J.; Kim, P.; Stormer, H. *Solid State Communications* **2008**, *146*, 351–355.
- [88] Tour, J. M. *Chemistry of Materials* **2014**, *26*, 163–171.
- [89] Levy, R. A. *Microelectronic Materials and Processes*; Springer Science & Business Media, 1989; Vol. 164; p 1000.

- [90] Sallai, G. *Acta Polytechnica Hungarica* **2012**, *9*, 171–181.
- [91] Emtsev, K. V.; Bostwick, A.; Horn, K.; Jobst, J.; Kellogg, G. L.; Ley, L.; McChesney, J. L.; Ohta, T.; Reshanov, S. A.; Röhrl, J.; Rotenberg, E.; Schmid, A. K.; Waldmann, D.; Weber, H. B.; Seyller, T. *Nature Materials* **2009**, *8*, 203–207.
- [92] Reina, A.; Jia, X.; Ho, J.; Nezich, D.; Son, H.; Bulovic, V.; Dresselhaus, M. S.; Kong, J. *Nano Letters* **2009**, *9*, 30–35.
- [93] Li, X.; Cai, W.; An, J.; Kim, S.; Nah, J.; Yang, D.; Piner, R.; Velamakanni, A.; Jung, I.; Tutuc, E.; Banerjee, S. K.; Colombo, L.; Ruoff, R. S. *Science* **2009**, *324*, 1312–1314.
- [94] Zhang, Y.; Zhang, L.; Zhou, C. *Accounts of Chemical Research* **2013**, *46*, 2329–2339.
- [95] Li, X.; Zhu, Y.; Cai, W.; Borysiak, M.; Han, B.; Chen, D.; Piner, R. D.; Colombo, L.; Ruoff, R. S. *Nano Letters* **2009**, *9*, 4359–4363.
- [96] Thune, E.; Strunk, C. *Introducing Molecular Electronics*; Springer Berlin Heidelberg, 2015; Vol. 680; pp 351–380.
- [97] Odom, T. W.; Huang, J.-L.; Kim, P.; Lieber, C. M. *The Journal of Physical Chemistry B* **2000**, *104*, 2794–2809.
- [98] Avouris, P.; Chen, Z.; Perebeinos, V. *Nature Nanotechnology* **2007**, *2*, 605–615.
- [99] Grobert, N. *Materials Today* **2007**, *10*, 28–35.
- [100] Guo, T.; Nikolaev, P.; Thess, A.; Colbert, D.; Smalley, R. *Chemical Physics Letters* **1995**, *243*, 49–54.
- [101] Eatemadi, A.; Daraee, H.; Karimkhanloo, H.; Kouhi, M.; Zarghami, N.; Akbarzadeh, A.; Abasi, M.; Hanifehpour, Y.; Joo, S. *Nanoscale Research Letters* **2014**, *9*, 393.
- [102] NanoIntegris Technologies, I. Small Diameter SWNTs (HiPco™) - NanoIntegris. <http://nanointegris.com/our-products/small-diameter-swnts-hipco/>.
- [103] Silvy, R. P.; Tan, Y.; Wallis, P. CoMoCAT® Single-wall Carbon Nanotubes. <https://www.sigmaaldrich.com/technical-documents/articles/materials-science/nanomaterials/comocat-carbon-nanotubes.html>.
- [104] Wang, H.; Bao, Z. *Nano Today* **2015**, *10*, 737–758.
- [105] Brohmann, M.; Rother, M.; Schießl, S. P.; Preis, E.; Allard, S.; Scherf, U.; Zaumseil, J. *Journal of Physical Chemistry C* **2018**, *122*, 19886–19896.
- [106] Qiu, S.; Wu, K.; Gao, B.; Li, L.; Jin, H.; Li, Q. *Advanced Materials* **2019**, *31*, 1800750.
- [107] Xiang, L.; Zhang, H.; Dong, G.; Zhong, D.; Han, J.; Liang, X.; Zhang, Z.; Peng, L.-M.; Hu, Y. *Nature Electronics* **2018**, *1*, 237–245.

- [108] Melzer, K.; Bhatt, V. D.; Jaworska, E.; Mittermeier, R.; Maksymiuk, K.; Michalska, A.; Lugli, P. *Biosensors and Bioelectronics* **2016**, *84*, 7–14.
- [109] Zhang, A.; Lieber, C. M. *Chemical Reviews* **2016**, *116*, 215–257.
- [110] Javey, A.; Qi, P.; Wang, Q.; Dai, H. *Proceedings of the National Academy of Sciences* **2004**, *101*, 13408–13410.
- [111] Yu, J.; Liu, G.; Sumant, A. V.; Goyal, V.; Balandin, A. A. *Nano Letters* **2012**, *12*, 1603–1608.
- [112] Dürkop, T.; Getty, S. A.; Cobas, E.; Fuhrer, M. S. *Nano Letters* **2004**, *4*, 35–39.
- [113] Mayorov, A. S.; Gorbachev, R. V.; Morozov, S. V.; Britnell, L.; Jalil, R.; Ponomarenko, L. A.; Blake, P.; Novoselov, K. S.; Watanabe, K.; Taniguchi, T.; Geim, A. K. *Nano Letters* **2011**, *11*, 2396–2399.
- [114] Chae, S. H.; Lee, Y. H. *Nano Convergence* **2014**, *1*, 15.
- [115] Rother, M.; Schießl, S. P.; Zakharko, Y.; Gannott, F.; Zaumseil, J. *ACS Applied Materials and Interfaces* **2016**, *8*, 5571–5579.
- [116] Schießl, S. P.; Fröhlich, N.; Held, M.; Gannott, F.; Schweiger, M.; Forster, M.; Scherf, U.; Zaumseil, J. *ACS Applied Materials and Interfaces* **2015**, *7*, 682–689.
- [117] Filipiak, M. S.; Rother, M.; Andoy, N. M.; Knudsen, A. C.; Grimm, S. B.; Bachran, C.; Swee, L. K.; Zaumseil, J.; Tarasov, A. *Proceedings* **2017**, *1*, 491.
- [118] Knopfmacher, O.; Tarasov, A.; Fu, W.; Wipf, M.; Niesen, B.; Calame, M.; Schönenberger, C. *Nano Letters* **2010**, *10*, 2268–2274.
- [119] Noor, M. O.; Krull, U. J. *Analytica Chimica Acta* **2014**, *825*, 1–25.
- [120] Rajan, N. K.; Duan, X.; Reed, M. A. *Wiley Interdisciplinary Reviews: Nanomedicine and Nanobiotechnology* **2013**, *5*, 629–645.
- [121] Chen, B.; Zhang, P.; Ding, L.; Han, J.; Qiu, S.; Li, Q.; Zhang, Z.; Peng, L. M. *Nano Letters* **2016**, *16*, 5120–5128.
- [122] Held, M.; Schießl, S. P.; Miebler, D.; Gannott, F.; Zaumseil, J. *Applied Physics Letters* **2015**, *107*, 83301.
- [123] Heller, I.; Mannik, J.; Lemay, S. G.; Dekker, C. *Nano Letters* **2009**, *9*, 377–382.
- [124] Zaumseil, J. *Semiconductor Science and Technology* **2015**, *30*, 74001.
- [125] Chen, F.; Qing, Q.; Xia, J.; Li, J.; Tao, N. *Journal of the American Chemical Society* **2009**, *131*, 9908–9909.
- [126] Fu, W.; Nef, C.; Knopfmacher, O.; Tarasov, A.; Weiss, M.; Calame, M.; Schönenberger, C. *Nano Letters* **2011**, *11*, 3597–3600.

- [127] Tarasov, A.; Tsai, M. Y.; Flynn, E. M.; Joiner, C. A.; Taylor, R. C.; Vogel, E. M. *2D Materials* **2015**, *2*, 044008.
- [128] Manoli, K.; Magliulo, M.; Mulla, M. Y.; Singh, M.; Sabbatini, L.; Palazzo, G.; Torsi, L. *Angewandte Chemie - International Edition* **2015**, *54*, 12562–12576.
- [129] Torsi, L.; Magliulo, M.; Manoli, K.; Palazzo, G. *Chemical Society Reviews* **2013**, *42*, 8612–8628.
- [130] Ganatra, R.; Zhang, Q. *ACS Nano* **2014**, *8*, 4074–4099.
- [131] Sarkar, D.; Liu, W.; Xie, X.; Anselmo, A. C.; Mitragotri, S.; Banerjee, K. *ACS Nano* **2014**, *8*, 3992–4003.
- [132] Cao, C.; Andrews, J. B.; Franklin, A. D. *Advanced Electronic Materials* **2017**, *3*, 1700057.
- [133] Graf, A.; Zakharko, Y.; Schiefl, S. P.; Backes, C.; Pfohl, M.; Flavel, B. S.; Zaumseil, J. *Carbon* **2016**, *105*, 593–599.
- [134] Fu, D.; Okimoto, H.; Lee, C. W.; Takenobu, T.; Iwasa, Y.; Kataura, H.; Li, L. J. *Advanced Materials* **2010**, *22*, 4867–4871.
- [135] Li, W. S.; Hou, P. X.; Liu, C.; Sun, D. M.; Yuan, J.; Zhao, S. Y.; Yin, L. C.; Cong, H.; Cheng, H. M. *ACS Nano* **2013**, *7*, 6831–6839.
- [136] Roberts, M. E.; Lemieux, M. C.; Bao, Z. *ACS Nano* **2009**, *3*, 3287–3293.
- [137] Novak, J. P.; Snow, E. S.; Houser, E. J.; Park, D.; Stepnowski, J. L.; McGill, R. A. *Applied Physics Letters* **2003**, *83*, 4026–4028.
- [138] Besteman, K.; Lee, J. O.; Wiertz, F. G.; Heering, H. A.; Dekker, C. *Nano Letters* **2003**, *3*, 727–730.
- [139] Gruner, G. *Analytical and Bioanalytical Chemistry* **2005**, *384*, 322–335.
- [140] Zheng, G.; Patolsky, F.; Cui, Y.; Wang, W. U.; Lieber, C. M. *Nature Biotechnology* **2005**, *23*, 1294–1301.
- [141] Stern, E.; Vacic, A.; Rajan, N. K.; Criscione, J. M.; Park, J.; Fahmy, T. M.; Reed, M. A. Label-free biomarker detection from whole blood. 2010 10th IEEE International Conference on Solid-State and Integrated Circuit Technology. 2010; pp 1392–1393.
- [142] Jang, H.-J.; Ahn, J.; Kim, M.-G.; Shin, Y.-B.; Jeun, M.; Cho, W.-J.; Lee, K. H. *Biosensors and Bioelectronics* **2015**, *64*, 318–323.
- [143] Piccinini, E.; Alberti, S.; Longo, G. S.; Berninger, T.; Breu, J.; Dostalek, J.; Azzaroni, O.; Knoll, W. *The Journal of Physical Chemistry C* **2018**, *122*, 10181–10188.
- [144] Ohno, Y.; Maehashi, K.; Matsumoto, K. *Journal of the American Chemical Society* **2010**, *132*, 18012–18013.

- [145] Tang, Y.; Memaugh, R.; Zeng, X. *Analytical Chemistry* **2006**, *78*, 1841–1848.
- [146] Grimm, S.; Schiefl, S. P.; Zakharko, Y.; Rother, M.; Brohmann, M.; Zaumseil, J. *Carbon* **2017**, *118*, 261–267.
- [147] Hu, L.; Hecht, D. S.; Gruner, G. *Nano Letters* **2004**, *4*, 2513–2517.
- [148] Heller, I.; Chatoor, S.; Männik, J.; Zevenbergen, M. A.; Dekker, C.; Lemay, S. G. *Journal of the American Chemical Society* **2010**, *132*, 17149–17156.
- [149] Lee, J.; Hwang, E.; Lee, E.; Seo, S.; Lee, H. *Chemistry - A European Journal* **2012**, *18*, 5155–5159.
- [150] Haustein, N.; Gutiérrez-Sanz, Ó.; Tarasov, A. *ACS Sensors* **2019**, acssensors.8b01515.
- [151] Chaudhury, P. K.; Nagarajan, K.; Dubey, P.; Sarkar, S. *Journal of Inorganic Biochemistry* **2004**, *98*, 1667–1677.
- [152] Abcam, GFP ELISA Kit (ab171581). <https://www.abcam.com/gfp-elisa-kit-ab171581.html>.
- [153] Rigante, S.; Scarbolo, P.; Wipf, M.; Stoop, R. L.; Bedner, K.; Buitrago, E.; Bazigos, A.; Bouvet, D.; Calame, M.; Schönenberger, C.; Ionescu, A. M. *ACS Nano* **2015**, *9*, 4872–4881.
- [154] Bae, T. E.; Jang, H. J.; Yang, J. H.; Cho, W. J. *ACS Applied Materials and Interfaces* **2013**, *5*, 5214–5218.
- [155] Ahn, J. H.; Kim, J. Y.; Seol, M. L.; Baek, D. J.; Guo, Z.; Kim, C. H.; Choi, S. J.; Choi, Y. K. *Applied Physics Letters* **2013**, *102*, 083701.
- [156] Kirchhofer, A.; Helma, J.; Schmidhals, K.; Frauer, C.; Cui, S.; Karcher, A.; Pellis, M.; Muyltermans, S.; Casas-Delucchi, C. S.; Cardoso, M. C.; Leonhardt, H.; Hopfner, K. P.; Rothbauer, U. *Nature Structural and Molecular Biology* **2010**, *17*, 133–139.
- [157] Saerens, D.; Pellis, M.; Loris, R.; Pardon, E.; Dumoulin, M.; Matagne, A.; Wyns, L.; Muyltermans, S.; Conrath, K. *Journal of Molecular Biology* **2005**, *352*, 597–607.
- [158] Rothbauer, U.; Zolghadr, K.; Tillib, S.; Nowak, D.; Schermelleh, L.; Gahl, A.; Backmann, N.; Conrath, K.; Muyltermans, S.; Cardoso, M. C.; Leonhardt, H. *Nature Methods* **2006**, *3*, 887–889.
- [159] Rother, M.; Kruse, A.; Brohmann, M.; Matthiesen, M.; Grieger, S.; Higgins, T. M.; Zaumseil, J. *ACS Applied Nano Materials* **2018**, *1*, 3616–3624.
- [160] Ries, J.; Kaplan, C.; Platonova, E.; Eghlidi, H.; Ewers, H. *Nature Methods* **2012**, *9*, 582–584.
- [161] Martinez, C. R.; Iverson, B. L. *Chemical Science* **2012**, *3*, 2191–2201.

- [162] Fox, M. A.; Whitesell, J. K. *Organische Chemie:: Grundlagen, Mechanismen, bioorganische Anwendungen. [Hauptbd.]: [...]*; Spektrum Akademischer Verlag, 1995; p 930.
- [163] Arakawa, T.; Timasheff, S. N. *Biochemistry* **1985**, *24*, 6756–6762.
- [164] Chen, H.; Choo, T. K.; Huang, J.; Wang, Y.; Liu, Y.; Platt, M.; Palaniappan, A.; Liedberg, B.; Tok, A. I. Y. *Materials and Design* **2016**, *90*, 852–857.
- [165] Lerner, M. B.; Dailey, J.; Goldsmith, B. R.; Brisson, D.; Charlie Johnson, A. T. *Biosensors and Bioelectronics* **2013**, *45*, 163–167.
- [166] Son, M.; Kim, D.; Park, K. S.; Hong, S.; Park, T. H. *Biosensors and Bioelectronics* **2016**, *78*, 87–91.
- [167] Chen, R. J.; Bangsaruntip, S.; Drouvalakis, K. A.; Wong Shi Kam, N.; Shim, M.; Li, Y.; Kim, W.; Utz, P. J.; Dai, H. *Proceedings of the National Academy of Sciences* **2003**, *100*, 4984–4989.
- [168] Kojima, A.; Hyon, C. K.; Kamimura, T.; Maeda, M.; Matsumoto, K. *Japanese Journal of Applied Physics, Part 1: Regular Papers and Short Notes and Review Papers* **2005**, *44*, 1596–1598.
- [169] Star, A.; Gabriel, J. C. P.; Bradley, K.; Grüner, G. *Nano Letters* **2003**, *3*, 459–463.
- [170] Baldo, S.; Buccheri, S.; Ballo, A.; Camarda, M.; La Magna, A.; Castagna, M. E.; Romano, A.; Iannazzo, D.; Di Raimondo, F.; Neri, G.; Scalese, S. *Sensing and Bio-Sensing Research* **2016**, *7*, 168–173.
- [171] Takeda, S.; Sbagyo, A.; Sakoda, Y.; Ishii, A.; Sawamura, M.; Sueoka, K.; Kida, H.; Mukasa, K.; Matsumoto, K. *Biosensors and Bioelectronics* **2005**, *21*, 201–205.
- [172] Schedin, F.; Geim, A. K.; Morozov, S. V.; Hill, E. W.; Blake, P.; Katsnelson, M. I.; Novoselov, K. S. *Nature Materials* **2007**, *6*, 652–655.
- [173] Forsyth, R.; Devadoss, A.; Guy, O. J. *Diagnostics* **2017**, *7*, 45.
- [174] Fu, W.; Jiang, L.; van Geest, E. P.; Lima, L. M.; Schneider, G. F. *Advanced Materials* **2017**, *29*, 1603610.
- [175] Fu, W.; Nef, C.; Tarasov, A.; Wipf, M.; Stoop, R.; Knopfmacher, O.; Weiss, M.; Calame, M.; Schönenberger, C. *Nanoscale* **2013**, *5*, 12104–12110.
- [176] Hess, L. H.; Seifert, M.; Garrido, J. A. *Proceedings of the IEEE* **2013**, *101*, 1780–1792.
- [177] Stine, R.; Mulvaney, S. P.; Robinson, J. T.; Tamanaha, C. R.; Sheehan, P. E. *Analytical chemistry* **2013**, *85*, 509–21.
- [178] Janata, J. *ECS Solid State Letters* **2012**, *1*, M29–M31.

- [179] Chauhan, N.; Maekawa, T.; Kumar, D. N. S. *Journal of Materials Research* **2017**, *32*, 2860–2882.
- [180] Green, N. S.; Norton, M. L. *Analytica Chimica Acta* **2015**, *853*, 127–142.
- [181] Ladenson, P. W.; Singer, P. A.; Ain, K. B.; Bagchi, N.; Bigos, S. T.; Levy, E. G.; Smith, S. A.; Daniels, G. H. *Archives of Internal Medicine* **2000**, *160*, 1573–1575.
- [182] Justino, C. I.; Duarte, A. C.; Rocha-Santos, T. A. *Advances in Clinical Chemistry*, 1st ed.; Elsevier Inc., 2016; Vol. 73; pp 65–108.
- [183] Gubala, V.; Harris, L. F.; Ricco, A. J.; Tan, M. X.; Williams, D. E. *Analytical Chemistry* **2012**, *84*, 487–515.
- [184] Song, Y.; Huang, Y. Y.; Liu, X.; Zhang, X.; Ferrari, M.; Qin, L. *Trends in Biotechnology* **2014**, *32*, 132–139.
- [185] Yager, P.; Domingo, G. J.; Gerdes, J. *Annual Review of Biomedical Engineering* **2008**, *10*, 107–144.
- [186] Lerner, M. B.; Reszczenski, J. M.; Amin, A.; Johnson, R. R.; Goldsmith, J. I.; Johnson, A. T. *Journal of the American Chemical Society* **2012**, *134*, 14318–14321.
- [187] Barradas, R. G.; Fletcher, S.; Porter, J. D. *Canadian Journal of Chemistry* **1976**, *54*, 1400–1404.
- [188] Tran, T. T.; Mulchandani, A. *TrAC - Trends in Analytical Chemistry* **2016**, *79*, 222–232.
- [189] Szkudlinski, M. W.; Fremont, V.; Ronin, C.; Weintraub, B. D. *Physiological Reviews* **2002**, *82*, 473–502.
- [190] Ohno, Y.; Maehashi, K.; Yamashiro, Y.; Matsumoto, K. *Nano Letters* **2009**, *9*, 3318–3322.
- [191] Stern, E.; Wagner, R.; Sigworth, F. J.; Breaker, R.; Fahmy, T. M.; Reed, M. A. *Nano Letters* **2007**, *7*, 3405–3409.
- [192] Lin, J.; Teweldebrhan, D.; Ashraf, K.; Liu, G.; Jing, X.; Yan, Z.; Li, R.; Ozkan, M.; Lake, R. K.; Balandin, A. A.; Ozkan, C. S. *Small* **2010**, *6*, 1150–1155.
- [193] Mao, S.; Lu, G.; Yu, K.; Bo, Z.; Chen, J. *Advanced Materials* **2010**, *22*, 3521–3526.
- [194] Okamoto, S.; Ohno, Y.; Maehashi, K.; Inoue, K.; Matsumoto, K. *Japanese Journal of Applied Physics* **2012**, *51*, 06FD08.
- [195] Saltzgaber, G.; Wojcik, P.; Sharf, T.; Leyden, M. R.; Wardini, J. L.; Heist, C. A.; Adenuga, A. A.; Remcho, V. T.; Minot, E. D. *Nanotechnology* **2013**, *24*, 355502.
- [196] Xu, S.; Zhan, J.; Man, B.; Jiang, S.; Yue, W.; Gao, S.; Guo, C.; Liu, H.; Li, Z.; Wang, J.; Zhou, Y. *Nature Communications* **2017**, *8*, 14902.

- [197] Reiner-Rozman, C.; Larisika, M.; Nowak, C.; Knoll, W. *Biosensors and Bioelectronics* **2015**, *70*, 21–27.
- [198] Dong, X.; Shi, Y.; Huang, W.; Chen, P.; Li, L. J. *Advanced Materials* **2010**, *22*, 1649–1653.
- [199] Farid, S.; Meshik, X.; Choi, M.; Mukherjee, S.; Lan, Y.; Parikh, D.; Poduri, S.; Baterdene, U.; Huang, C. E.; Wang, Y. Y.; Burke, P.; Dutta, M.; Stroschio, M. A. *Biosensors and Bioelectronics* **2015**, *71*, 294–299.
- [200] Hao, Z.; Zhu, Y.; Wang, X.; Rotti, P. G.; Dimarco, C.; Tyler, S. R.; Zhao, X.; Engelhardt, J. F.; Hone, J.; Lin, Q. *ACS Applied Materials and Interfaces* **2017**, *9*, 27504–27511.
- [201] Lerner, M. B.; Matsunaga, F.; Han, G. H.; Hong, S. J.; Xi, J.; Crook, A.; Perez-Aguilar, J. M.; Park, Y. W.; Saven, J. G.; Liu, R.; Johnson, A. T. *Nano Letters* **2014**, *14*, 2709–2714.
- [202] Xu, G.; Abbott, J.; Qin, L.; Yeung, K. Y. M.; Song, Y.; Yoon, H.; Kong, J.; Ham, D. *Nature Communications* **2014**, *5*, 4866.
- [203] Lanche, R.; Pachauri, V.; Munief, W. M.; Müller, A.; Schwartz, M.; Wagner, P.; Thoelen, R.; Ingebrandt, S. *FlatChem* **2018**, *7*, 1–9.
- [204] Arnold, K.; Herrmann, A.; Pratsch, L.; Gawrisch, K. *BBA - Biomembranes* **1985**, *815*, 515–518.
- [205] Adam, S.; Hwang, E. H.; Galitski, V.; Sarma, S. D. *Proceedings of the National Academy of Sciences* **2007**, *104*, 18392–18397.
- [206] Chen, F.; Xia, J.; Tao, N. *Nano Letters* **2009**, *9*, 1621–1625.
- [207] Hasan, N.; Hou, B.; Moore, A. L.; Radadia, A. D. *Advanced Materials Technologies* **2018**, *3*, 1800133.
- [208] Kim, D. J.; Park, H. C.; Sohn, I. Y.; Jung, J. H.; Yoon, O. J.; Park, J. S.; Yoon, M. Y.; Lee, N. E. *Small* **2013**, *9*, 3352–3360.
- [209] Mansour, M.; Mansour, J. B.; Swesy, A. H. E. *Human Resources for Health* **2010**, *8*, 621–626.
- [210] Ping, J.; Xi, J.; Saven, J. G.; Liu, R.; Johnson, A. T. *Biosensors and Bioelectronics* **2017**, *89*, 689–692.
- [211] Cass, A. E.; Davis, G.; Francis, G. D.; Allen, H.; Hill, O.; Aston, W. J.; Higgins, I. J.; Plotkin, E. V.; Scott, L. D.; Turner, A. P. *Analytical Chemistry* **1984**, *56*, 667–671.
- [212] Bartlett, P. N.; Al-Lolage, F. A. *Journal of Electroanalytical Chemistry* **2018**, *819*, 26–37.
- [213] Wilson, G. S. *Biosensors and Bioelectronics* **2016**, *82*, 7–8.

- [214] Shiota, M.; Yamazaki, T.; Yoshimatsu, K.; Kojima, K.; Tsugawa, W.; Ferri, S.; Sode, K. *Bioelectrochemistry* **2016**, *112*, 178–183.
- [215] Yamashita, Y.; Lee, I.; Loew, N.; Sode, K. *Current Opinion in Electrochemistry* **2018**, 1–9.
- [216] Kwak, Y. H.; Choi, D. S.; Kim, Y. N.; Kim, H.; Yoon, D. H.; Ahn, S. S.; Yang, J. W.; Yang, W. S.; Seo, S. *Biosensors and Bioelectronics* **2012**, *37*, 82–87.
- [217] Li, W.; Tan, C.; Lowe, M. A.; Abruña, H. D.; Ralph, D. C. *ACS Nano* **2011**, *5*, 2264–2270.
- [218] Velický, M.; Bradley, D. F.; Cooper, A. J.; Hill, E. W.; Kinloch, I. A.; Mishchenko, A.; Novoselov, K. S.; Patten, H. V.; Toth, P. S.; Valota, A. T.; Worrall, S. D.; Dryfe, R. A. *ACS Nano* **2014**, *8*, 10089–10100.
- [219] Devasenathipathy, R.; Karthik, R.; Chen, S. M.; Ali, M. A.; Mani, V.; Lou, B. S.; Al-Hemaid, F. M. A. *Microchimica Acta* **2015**, *182*, 2165–2172.
- [220] Qi, M.; Zhang, Y.; Cao, C.; Lu, Y.; Liu, G. *RSC Advances* **2016**, *6*, 39180–39187.
- [221] Guo, Y.; Han, Y.; Shuang, S.; Dong, C. *Journal of Materials Chemistry* **2012**, *22*, 13166–13173.
- [222] Yang, Z.; Cao, Y.; Li, J.; Jian, Z.; Zhang, Y.; Hu, X. *Analytica Chimica Acta* **2015**, *871*, 35–42.
- [223] Razmi, H.; Mohammad-Rezaei, R. *Biosensors and Bioelectronics* **2013**, *41*, 498–504.
- [224] Wang, Y.; Ge, L.; Wang, P.; Yan, M.; Yu, J.; Ge, S. *Chemical Communications* **2014**, *50*, 1947–1949.
- [225] Chia, J. S. Y.; Tan, M. T.; Khiew, P. S.; Chin, J. K.; Siong, C. W. *Sensors and Actuators B: Chemical* **2015**, *210*, 558–565.
- [226] Gutes, A.; Carraro, C.; Maboudian, R. *Biosensors and Bioelectronics* **2012**, *33*, 56–59.
- [227] Luong, J. H.; Glennon, J. D.; Gedanken, A.; Vashist, S. K. *Microchimica Acta* **2017**, *184*, 369–388.
- [228] Ravenna, Y.; Xia, L.; Gun, J.; Mikhaylov, A. A.; Medvedev, A. G.; Lev, O.; Alfonta, L. *Analytical Chemistry* **2015**, *87*, 9567–9571.
- [229] Thodkar, K.; El Abbassi, M.; Lüönd, F.; Overney, F.; Schönenberger, C.; Jeanerret, B.; Calame, M. *Physica Status Solidi - Rapid Research Letters* **2016**, *10*, 807–811.
- [230] Ginsberg, B. H. *Journal of Diabetes Science and Technology* **2009**, *3*, 903–913.

- [231] Rutkowski, M.; Grzegorzczak, K. *Polski mercuriusz lekarski : organ Polskiego Towarzystwa Lekarskiego* **1999**, *6*, 57–60.
- [232] Pournaghi-Azar, M. H.; Ojani, R. *Talanta* **1995**, *42*, 1839–1848.
- [233] Vogt, S.; Schneider, M.; Schfer-Eberwein, H.; Nill, G. *Analytical Chemistry* **2014**, *86*, 7530–7535.
- [234] Shan, C.; Yang, H.; Song, J.; Han, D.; Ivaska, A.; Niu, L. *Analytical Chemistry* **2009**, *81*, 2378–2382.
- [235] Chen, J.; Zheng, X.; Miao, F.; Zhang, J.; Cui, X.; Zheng, W. *Journal of Applied Electrochemistry* **2012**, *42*, 875–881.
- [236] Mani, V.; Devadas, B.; Chen, S. M. *Biosensors and Bioelectronics* **2013**, *41*, 309–315.
- [237] Unnikrishnan, B.; Palanisamy, S.; Chen, S. M. *Biosensors and Bioelectronics* **2013**, *39*, 70–75.
- [238] Yu, Y.; Chen, Z.; He, S.; Zhang, B.; Li, X.; Yao, M. *Biosensors and Bioelectronics* **2014**, *52*, 147–152.
- [239] Liang, B.; Fang, L.; Yang, G.; Hu, Y.; Guo, X.; Ye, X. *Biosensors and Bioelectronics* **2013**, *43*, 131–136.
- [240] Kang, X.; Wang, J.; Wu, H.; Aksay, I. A.; Liu, J.; Lin, Y. *Biosensors and Bioelectronics* **2009**, *25*, 901–905.
- [241] Xu, Q.; Gu, S. X.; Jin, L.; Zhou, Y. E.; Yang, Z.; Wang, W.; Hu, X. *Sensors and Actuators, B: Chemical* **2014**, *190*, 562–569.
- [242] Liang, B.; Guo, X.; Fang, L.; Hu, Y.; Yang, G.; Zhu, Q.; Wei, J.; Ye, X. *Electrochemistry Communications* **2015**, *50*, 1–5.
- [243] Cai, C. J.; Xu, M. W.; Bao, S. J.; Lei, C.; Jia, D. Z. *RSC Advances* **2012**, *2*, 8172–8178.
- [244] Wang, H. Y.; Bernarda, A.; Huang, C. Y.; Lee, D. J.; Chang, J. S. *Bioresource Technology* **2011**, *102*, 235–243.
- [245] Palanisamy, S.; Karuppiah, C.; Chen, S. M. *Colloids and Surfaces B: Biointerfaces* **2014**, *114*, 164–169.
- [246] Hua, L.; Wu, X.; Wang, R. *Analyst* **2012**, *137*, 5716–5719.
- [247] Hui, J.; Cui, J.; Xu, G.; Adeloju, S. B.; Wu, Y. *Materials Letters* **2013**, *108*, 88–91.
- [248] Zhang, Y.; Fan, Y.; Wang, S.; Tan, Y.; Shen, X.; Shi, Z. *Chinese Journal of Chemistry* **2012**, *30*, 1163–1167.
- [249] Wu, P.; Shao, Q.; Hu, Y.; Jin, J.; Yin, Y.; Zhang, H.; Cai, C. *Electrochimica Acta* **2010**, *55*, 8606–8614.

- [250] Vilian, A. T.; Chen, S. M.; Ali, M. A.; Al-Hemaid, F. M. *RSC Advances* **2014**, *4*, 30358–30367.
- [251] Palanisamy, S.; Vilian, A. T. E.; Chen, S.-m. *International Journal of Electrochemical Science* **2015**, *7*, 2153–2163.
- [252] Cui, M.; Xu, B.; Hu, C.; Shao, H. B.; Qu, L. *Electrochimica Acta* **2013**, *98*, 48–53.
- [253] Chu, Z.; Liu, Y.; Xu, Y.; Shi, L.; Peng, J.; Jin, W. *Electrochimica Acta* **2015**, *176*, 162–171.
- [254] Terse-Thakoor, T.; Komori, K.; Ramnani, P.; Lee, I.; Mulchandani, A. *Langmuir* **2015**, *31*, 13054–13061.
- [255] Wang, Z.; Zhou, X.; Zhang, J.; Boey, F.; Zhang, H. *Journal of Physical Chemistry C* **2009**, *113*, 14071–14075.
- [256] Yang, W.; Ratinac, K. R.; Ringer, S. R.; Thordarson, P.; Gooding, J. J.; Braet, F. *Angewandte Chemie - International Edition* **2010**, *49*, 2114–2138.
- [257] Zhang, Q.; Wu, S.; Zhang, L.; Lu, J.; Verproot, F.; Liu, Y.; Xing, Z.; Li, J.; Song, X. M. *Biosensors and Bioelectronics* **2011**, *26*, 2632–2637.
- [258] Dalglish, T.; Williams, J. M. G.; Golden, A.-M. J.; Perkins, N.; Barrett, L. F.; Barnard, P. J.; Au Yeung, C.; Murphy, V.; Elward, R.; Tchanturia, K.; Watkins, E. *Journal of Experimental Psychology: General*; Access Online via Elsevier, 2007; Vol. 136; pp 23–42.
- [259] Chen, S.; Bomer, J. G.; Carlen, E. T.; Van Den Berg, A. *Nano Letters* **2011**, *11*, 2334–2341.
- [260] Yin, H.; Zhou, Y.; Meng, X.; Shang, K.; Ai, S. *Biosensors and Bioelectronics* **2011**, *30*, 112–117.
- [261] Luo, Z.; Yuwen, L.; Han, Y.; Tian, J.; Zhu, X.; Weng, L.; Wang, L. *Biosensors and Bioelectronics* **2012**, *36*, 179–185.
- [262] Hwa, K. Y.; Subramani, B. *Biosensors and Bioelectronics* **2014**, *62*, 127–133.
- [263] Kong, F. Y.; Gu, S. X.; Li, W. W.; Chen, T. T.; Xu, Q.; Wang, W. *Biosensors and Bioelectronics* **2014**, *56*, 77–82.
- [264] Amouzadeh Tabrizi, M.; Varkani, J. N. *Sensors and Actuators B: Chemical* **2014**, *202*, 475–482.
- [265] Degani, Y.; Heller, A. *The Journal of Physical Chemistry* **1987**, *91*, 1285–1289.
- [266] Lee, I.; Loew, N.; Tsugawa, W.; Lin, C. E.; Probst, D.; La Belle, J. T.; Sode, K. *Bioelectrochemistry* **2018**, *121*, 1–6.
- [267] Yamashita, Y.; Suzuki, N.; Hirose, N.; Kojima, K.; Tsugawa, W.; Sode, K. *International Journal of Molecular Sciences* **2018**, *19*, 931.

- [268] Rüdiger, O.; Abad, J. M.; Hatchikian, E. C.; Fernandez, V. M.; De Lacey, A. L. *Journal of the American Chemical Society* **2005**, *127*, 16008–16009.
- [269] Muguruma, H.; Iwasa, H.; Hidaka, H.; Hiratsuka, A.; Uzawa, H. *ACS Catalysis* **2017**, *7*, 725–734.

List of abbreviations:

- AC - alternating current
- BSA - bovine serum albumin
- CE - counter (auxiliary) electrode
- CNT - carbon nanotubes
- CVD - chemical vapour deposition
- DNA - deoxyribonucleic acid
- EC - Enzyme Commission
- EDC - 1-ethyl-3-(3-dimethylaminopropyl) carbodiimide hydrochloride
- EGFET - electrolyte-gated field-effect transistor
- ELISA - enzyme-linked immunosorbent assay
- F(ab')<sub>2</sub> - antibody fragment with two antigen-binding sites linked by disulfide bond
- Fab - antibody fragment with one antigen-binding site
- FAD - flavin adenine dinucleotide
- Fc - ferrocene
- FET - field-effect transistor
- GDH - glucose dehydrogenase
- GFET - graphene field-effect transistor
- GFP - green fluorescent protein
- GO - graphene oxide
- GOx - glucose oxidase
- IEP - isoelectric point
- IgG - immunoglobulin, antibody
- IHP - inner Helmholtz plane
- $k_{cat}$  - turnover number
- $k_{off}$  - off-rate constant
- $k_{on}$  - on-rate constant
- $K_a$  - association (binding) constant

- $K_d$  - dissociation constant
- $K_M$  - Michaelis-Menten constant
- LoD - limit of detection
- $M_W$  - molecular weight
- MAL - maleimide group
- MOSFET - metal-oxide-semiconductor field-effect transistor
- mPEG-pyrene - poly(ethylene glycol) modified with pyrene functional group
- NA - nitrosoaniline derivative, specifically *N,N*-bis(hydroxyethyl)-3-methoxy-4-nitrosoaniline
- NHS - *N*-hydroxysuccinimide
- NT - nanotube
- OHP - outer Helmholtz plane
- PBA - 1-pyrenebutyric acid
- PBA-NHS - 1-pyrenebutyric acid *N*-hydroxysuccinimide ester
- PEG - poly(ethylene glycol)
- PMMA - poly(methyl methacrylate)
- PoC - Point-of-Care
- py-MAL - *N*-(1-pyrenyl)maleimide
- QCM - quartz crystal microbalance
- RBM - radial breathing mode
- RE - reference electrode
- rGO - reduced graphene oxide
- STM - scanning tunnelling microscopy
- SWCNT - single-walled carbon nanotubes
- TEM - transmission electron microscopy
- TEV - tobacco etch virus protease
- TSH - thyroid stimulating hormone
- VHH - nanobodies
- WE - working electrode

List of symbols:

- $\lambda_D$  - Debye length
- $\nu_F$  - Fermi velocity
- $\rho_e$  - local electric charge density in C/m<sup>3</sup>
- $\varepsilon$  - dielectric constant (relative permittivity) of the solvent
- $\varepsilon_0$  - permittivity of vacuum
- $\Psi_s$  - potential across the EDL
- D - diffusion coefficient
- E - electrochemical potential
- e - elementary charge of electron ( $1.602 \times 10^{19}$ )
- E - standard electrode potential
- F - Faraday constant ( 96 485 C / mol)
- $g_m$  - transconductance
- I - current
- $I_{SD}$  - source-drain current
- $k_B$  - Boltzmann constant
- $k_{cat}$  - turnover number
- $K_M$  - Michaelis-Menten constant
- L - FET channel length
- $N_A$  - Avogadro constant ( $6.022 \times 10^{23} \text{ mol}^{-1}$ )
- Q - charge density in the channel
- R - universal gas constant (8.314 J / mol K)
- T - temperature in Kelvin
- t - time in seconds
- $V_G$  - gate voltage
- $V_{SD}$  - source-drain voltage
- $V_{th}$  - threshold voltage
- W - FET channel width
- z - charge of the ion



# Personal information

## Publication list

1. **Filipiak, M. S.**; Vetter, D.; Gutiérrez-Sanz, O.; Jönsson-Niedziółka, M.; Tarasov, A. Direct Electron Transfer from Glucose Dehydrogenase to Single Sheet Graphene Electrode. (submitted)
2. Gutiérrez-Sanz, O; Haustein, N.; Schroeter, M.; Oelschlaegel, T.; **Filipiak, M.S.**; Tarasov, A. Transistor-based immunosensing in human serum samples without on-site calibration. (submitted)
3. Andoy, N. M.; **Filipiak, M. S.**; Vetter, D.; Gutiérrez-sanz, Ó. Graphene-Based Electronic Immunosensor with Femtomolar Detection Limit in Whole Serum. *Adv. Mater. Technol.* 2018, 1800186, 1–12.
4. **Filipiak, M. S.**; Rother, M.; Andoy, N. M.; Knudsen, A. C.; Grimm, S.; Bachran, C.; Swee, L. K.; Zaumseil, J.; Tarasov, A. Highly Sensitive, Selective and Label-Free Protein Detection in Physiological Solutions Using Carbon Nanotube Transistors with Nanobody Receptors. *Sensors Actuators B Chem.* 2018, 255 (Part 2), 1507–1516.
5. **Filipiak, M. S.**; Rother, M.; Andoy, N. M.; Knudsen, A. C.; Grimm, S. B.; Bachran, C.; Swee, L. K.; Zaumseil, J.; Tarasov, A. Label-Free Immunodetection in High Ionic Strength Solutions Using Carbon Nanotube Transistors with Nanobody Receptors. *Proceedings* 2017, 1 (10), 491.
6. Gutiérrez-Sanz, Ó.; Andoy, N. M.; **Filipiak, M. S.**; Haustein, N.; Tarasov, A. Direct, Label-Free, and Rapid Transistor-Based Immunodetection in Whole Serum. *ACS Sensors* 2017, 2 (9), 1278–1286.
7. **Filipiak, M. S.**; Zloczewska, A.; Grzeskowiak, P.; Lynch, R.; Jönsson-Niedziółka, M. Tris(Hydroxymethyl)Aminomethane Photooxidation on Titania Based Photoanodes and Its Implication for Photoelectrochemical Biofuel Cells. *J. Power Sources* 2015, 289, 17–21.
8. Celebanska, A.; **Filipiak, M. S.**; Lesniewski, A.; Jubete, E.; Opallo, M. Nanocarbon Electrode Prepared from Oppositely Charged Nanoparticles and Nanotubes for Low-Potential Thiocholine Oxidation. *Electrochim. Acta* 2015, 176, 249–254.

### Patent list

1. International patent application WO/2018/153918 *Polymer coating of electrodes for sensor devices* filed 21.02.2018
2. Polish patent P-405159 *Carbon multilayer electrode and its application* filed 29.08.2013

### Conference appearances:

1. XXXI Eurosensors – 03-06.09.2017 – Paris, France - Label-Free Immunodetection in High Ionic Strength Solutions Using Carbon Nanotube Transistors with Nanobody Receptors (poster)
2. SELECTBio Biodetection and Biosensors 2017 – 10-11.10.2017 – Cambridge, UK - Label-Free Immunodetection in High Ionic Strength Solutions Using Carbon Nanotube Transistors with Nanobody Receptors (poster)
3. 29th World Congress on Biosensors – 12-15.06.2018 – Miami, USA - Highly Sensitive, Selective and Label-Free Protein Detection in Physiological Solutions Using Carbon Nanotube Transistors with Nanobody Receptors (poster)

### Teaching experience

- Supervisor of Amy Leson's Master of Science in Biomedical Engineering thesis *Design and Assessment of a Microfluidic Nanomaterial-based Biosensing Platform* 09.2017 – 04.2018

## PERSONAL DETAILS

---

Surname: Filipiak  
Given names: Marcin Szymon  
Date of birth: January 3<sup>rd</sup>, 1990  
Place of birth: Bydgoszcz, Poland  
Nationality: Polish  
E-Mail: marcinszymonfilipiak@gmail.com

## EDUCATION

---

- |                   |  |
|-------------------|--|
| 02.2016 - 06.2019 | Dr. rer. nat. (PhD) in Physical Chemistry<br>Thesis subject <i>"Carbon based nanomaterials for biosensing applications"</i><br>Institute for Physical Chemistry, Universität Heidelberg<br>(Heidelberg, Germany)   |
| 02.2012 – 01.2014 | Master of Science in Biotechnology Engineering (Microbioanalytics)<br>Thesis subject <i>"Layer-by-layer technique based carbon nanostructured electrode and acetylcholinesterase immobilization for construction of biosensor for organophosphate pesticides determination"</i><br>Faculty of Chemistry, Warsaw University of Technology<br>(Warsaw, Poland) |
| 10.2008 – 02.2012 | Bachelor of Science in Biotechnology Engineering<br>Thesis subject <i>"Modification of amperometric sensors for imipramine detection"</i><br>Faculty of Chemistry, Warsaw University of Technology<br>(Warsaw, Poland)   |
| 10 – 11. 2010     | <i>"Lab-on-a-Chip in medical diagnostics"</i> summer school<br>Faculty of Chemistry, Warsaw University of Technology<br>(Warsaw, Poland)   |
| 09 – 10.2010      | <i>"Sensors and biosensors"</i> specialized course<br>Faculty of Chemistry, Warsaw University of Technology<br>(Warsaw, Poland)  |

## WORK EXPERIENCE

---

- |                   |   |
|-------------------|---|
| 10.2015 - present | Research Associate<br>"Nanomaterial-Based Biosensors" group<br>BioMed X GmbH (Heidelberg, Germany)  |
| 02.2014 – 09.2015 | Technical Specialist / Assistant (from 10.2014)<br>"Charge Transfer Processes in Hydrodynamic Systems" group<br>Institute of Physical Chemistry, Polish Academy of Sciences<br>(Warsaw, Poland) |
| 07 – 08.2012      | Intern<br>"Biogeochemistry and Environmental Analytical Chemistry<br>(BEACh)" group<br>Centre for Research in Earth Sciences, University of Plymouth<br>(Plymouth, UK)                          |
| 05 – 07.2011      | Intern<br>"Hybrid Microbiosystem Engineering" group<br>Nałęcz Institute of Biocybernetics and<br>Biomedical Engineering (Warsaw, Poland)  |

## RESEARCH INTERESTS

---

- electrochemistry
- field-effect transistors
- nanomaterials
- surface modification
- biosensors
- surface characterization (AFM, SEM, Raman)
- microfluidics
- microfabrication

## SKILLS

---

### *Language skills:*

Polish (native), English (C2), German (A2/B1), Russian (A2)

### *Computer skills:*

MS Office, Origin, ChemsSketch, Autodesk AutoCAD, Autodesk Inventor, Adobe Photo-shop, Adobe Illustrator, R Studio, L<sup>A</sup>T<sub>E</sub>X

## ADDITIONAL INFORMATION

---

- Reviewer for *Sensors and Actuators B: Chemical, Biosensors and Bioelectronics*
- Originator, founder, first president and honorary member of Warsaw Society of Biotechnology "Symbioza" (<http://symbioza.edu.pl/en/>)

# Acknowledgements

This work would not have been done without:

- Marcel Rother, Stefan Grimm, Stefan Schießl, Maximilian Brohmann, Martin Held, Jana Zaumseil from Institute for Physical Chemistry, Heidelberg University
- Natalie Haustein, Nesha May Andoy, Oscar Gutierrez-Sanz, Amy Leson, Daniel Vetter, Anton Malovichko, Kishan Thodkar, Alexey Tarasov, Christopher Bachran, Christian Weber, Kim Lee Swee, Arne Knudsen from BioMed X GmbH
- Stefan Nester, Janusz Schinke from Innovation Lab GmbH
- Michael Hein from Roche Diagnostics International Ltd.
- Reiner Schlipfenbacher, Jürgen Spinke, Moritz Marcinowski, Heiko Mussauer from Roche Diagnostics GmbH
- Arnulf Staib, Alexander Licht from Roche Diabetes Care GmbH
- Martin Jönsson-Niedziółka from Institute of Physical Chemistry, Polish Academy of Sciences

The research of the team "Nanomaterial-Based Biosensors" at BioMed X Innovation Center is kindly sponsored by Roche Diagnostics GmbH.



## Personal acknowledgements

I am very lucky to find a lot of amazing people on my path, who help me to develop all the time. I am grateful that these people are not only my co-workers, but friends as well, and that includes (in random order):

- Jana Zaumseil who made possible doing the PhD studies despite working for BioMed X GmbH,
- Alexey Tarasov for introducing me into the field-effect transistor based biosensing,
- Nesha May Andoy and Christopher Bachran for teaching me (again) the biochemistry,
- Maximilian Brohman and Stefan Grimm for helping me and teaching the AFM and Raman spectroscopy,
- Martin Held for his help with ALD and more recently - photolithography,
- Stefan Nester and Janusz Schinke for their help with thermal evaporator, laser cutting and clean room introduction,
- Marcel Rother for introducing me into the world of semiconducting carbon nanotubes,
- Anton Malovichko for helping with the first Team NBB measurement setup,
- Łukasz Kozoń for being my consultant on microfluidics,
- Kamil F. Trzebuniak for dispelling my doubts about statistics,
- Amy Leson for being the best MSc student I had, designing the second generation of Team NBB measurement setup and teaching me Inventor,
- Christian Weber for helping me survive in the German jungle and being my translator,
- Martin Jönsson-Niedziółka for being my electrochemistry advisor,
- Natalie Haustein for being in the same boat and patiently enduring my desk-to-desk neighbourhood, as well as helping me out with R,
- Renata Filipiak, my mom, and Tomasz Filipiak, my brother, for being the best family I could upbringing in and teaching me the importance and value of education,
- Natalia Kołakowska-Filipiak, my lovely wife, for her constant support, patience and love, as well as reminding me that "one works to live, not lives to work"

Eidesstattliche Versicherung gemäß § 8 der Promotionsordnung  
der Naturwissenschaftlich-Mathematischen Gesamtfakultät  
der Universität Heidelberg

1. Bei der eingereichten Dissertation zu dem Thema

*"Carbon based nanomaterials for biosensing applications"*

handelt es sich um meine eigenständig erbrachte Leistung.

2. Ich habe nur die angegebenen Quellen und Hilfsmittel benutzt und mich keiner unzulässigen Hilfe Dritter bedient. Insbesondere habe ich wörtlich oder sinngemäß aus anderen Werken übernommene Inhalte als solche kenntlich gemacht.
3. Die Arbeit oder Teile davon habe ich bislang nicht an einer Hochschule des In- oder Auslands als Bestandteil einer Prüfungs- oder Qualifikationsleistung vorgelegt.
4. Die Richtigkeit der vorstehenden Erklärungen bestätige ich.
5. Die Bedeutung der eidesstattlichen Versicherung und die strafrechtlichen Folgen einer unrichtigen oder unvollständigen eidesstattlichen Versicherung sind mir bekannt.

Ich versichere an Eides statt, dass ich nach bestem Wissen die reine Wahrheit erklärt und nichts verschwiegen habe.

Ort und Datum

Unterschrift